Exploration of Resilient Divertors in Stellarators

by
Kelly Adriana Garcia

A dissertation submitted in partial fulfillment
of the requirements for the degree of
Doctor of Philosophy
Nuclear Engineering & Engineering Physics

at the
University of Wisconsin-Madison
2025

Date of final oral examination: 06/20/2025
Committee Members:
Oliver Schmitz, Professor, Nuclear Engineering & Engineering Physics (Advisor)
Carl Sovinec, Professor Emeritus, Nuclear Engineering & Engineering Physics
Adelle Wright, Assistant Professor, Nuclear Engineering & Engineering Physics
Rogerio Jorge, Assistant Professor, Physics
Aaron Bader, Senior Scientist, Type One Energy Inc.

Abstract

A stable divertor concept is of significant importance for stellarator-based fusion energy. Optimized stellarator configurations will need stable divertors to withstand equilibrium changes which arise as plasma pressure is built up. The main focus of this work is the non-resonant divertor (NRD) as it is an alternative divertor solution to current stellarator divertors used in practice. NRDs separate the confined plasma from surrounding material structures. The intersection pattern of field lines with material surfaces, or divertor targets, is considered to be almost insensitive to plasma equilibrium effects. However, a complex scrape-off layer (SOL), which is created by a chaotic plasma boundary within the NRD geometry, connects the core plasma domain to the plasma facing surfaces (PFCs) through magnetic flux tubes of varying orders of magnitude length scales.

The Compact Toroidal Hybrid (CTH) serves as a test-bed to explore NRD features in a simple circular wall geometry. This is done by scanning across several inductive current levels driven by the central solenoid of the device. Simulations observed a significant change of the chaotic magnetic edge structure along with an effective distance between the confined plasma region and the instrumented divertor wall target. At the same time, the helical intersection pattern of the field lines that strike the wall are contained within an overall narrow helical band. We identify this as a resilient strike line pattern. Within this pattern there are signatures of homoclinic and heteroclinic tangles that connect the interior island chains to the wall. These magnetic field structures are seen in heat flux modeling with the EMC3-EIRENE code to be governed by the long connection length L_C of the field lines. At low inductive currents, the excursion of these field lines from the confined plasma is small and the configuration resembles a limited plasma wall scenario where a closed flux surface is intercepted by the PFC. For high inductive current levels of $\geq 6\,\mathrm{kA}$, the helical strike line pattern splits into two bands and establishes a private magnetic flux region in between them. These bands act as divertor legs for the strike line pattern with distinct parallel particle flow SOL channels. These results demonstrate the NRD strike line pattern resiliency within CTH where the underlying chaotic field lines within the plasma boundary determine if the plasma wall scenario is diverted or limited.

As CTH had a simple vessel geometry, we consider the Helically Symmetric eXperiment (HSX) to investigate the impact plasma shaping on resilient NRD divertor features in an optimized quasihelically symmetric (QHS) device. An expanded vessel wall was considered that would give space for implementation of a physical divertor target structure. The analysis was done for four different magnetic configurations with very different plasma edge behavior. A resilient strike line pattern was identified across all configurations by sampling the field lines' L_C along the wall. This magnetic footprint calculation showed that the field lines along this helical intersection pattern have long L_C. Further investigation into the details of the magnetic footprint's resilient helical band linked the magnetic structures in the edge with the field lines' radial penetration depth into the plasma. This analysis was carried out by introducing a new metric, the minimum radial connection of a field line from the last closed flux surface (LCFS) $\min(\delta_N)$. The relationship, namely the deviation from an empirical scaling law, between the field lines' $\min(\delta_N)$ and L_C suggested if field lines interacting with the wall are associated with structures such as resonant islands, cantori, and turnstiles. This helps determine the relevant magnetic flux channels based on the radial location of these chaotic edge structures and the divertor target footprint.

The next step taken in HSX with this expanded wall was simulation of the basic plasma transport behavior with EMC3-EIRENE. We assessed SOL behavior to see if detachment, which is a desirable SOL regime for divertor performance, could be achieved on the bare wall and especially in the presence of open chaotic structures. By performing a scan of the upstream density n_u, the modeled downstream quantities of temperature and density were connected to the overall power balance behavior as a function of n_u. These quantities together suggest access into energy dissipative detachment. The high-recycling regime, however, was not obtained due to a lack of volumetric particle recombination and the simulated particle flux remained attached to the wall. Similar behavior of no observed high-recycling occurs in other stellarator devices and is, in general, a major research interest for NRD divertor performance. The simulated heat and particle flux on the wall location was also studied and found to be resilient on the wall. This is consistent with the results of field line following modeling. The EMC3-EIRENE work serves as a basis for future work into grid improvements for a deeper analysis into what is needed for a physical resilient divertor structure. For detachment access, this is important not only for identifying a mechanical structure(s) to improve volumetric particle recombination for detachment, but also for understanding other physics parameters necessary for detachment.

Finally, the metrics developed and tested for CTH and HSX were applied to W7-X which is a quasi-isodynamic (QI) stellarator. The magnetic configurations studied in W7-X are high-performance scenarios which were found by changing the rotational transform and shifting the 5/5 island chain inward with respect to the standard island divertor configuration. The current in-vessel island divertor components were removed in order to explore the open field line behavior of these magnetic configurations with the wall as the main PFC. This analysis was also performed to scope out a resilient NRD-like mechanical structure. Despite both configurations not featuring an open chaotic layer like was observed in HSX, the field lines of the chosen magnetic configurations at the wall followed the empirical relationship consistent with the HSX investigation's findings. This was also the case when one of the configuration's plasma wall scenario was a limiter. The field line following analysis in W7-X demonstrates the importance in identifying a high-performance equilibria with NRD magnetic edge features. Moreover, this is relevant for low magnetic shear QI stellarators like W7-X which are susceptible to equilibrium effects that alter the magnetic edge structure and hence the divertor setup.

Acknowledgments

First, I would like to thank my advisor, Prof. Oliver Schmitz, for his support and guidance throughout my dissertation. I would also like to thank my co-advisor, Dr. Aaron Bader, for his mentorship and willingness to answer all my questions (even when there were no answers). I am sincerely grateful to Dr. Heinke Frerichs for the availability and use of the FLARE code without which this thesis could not have been done. I am also thankful for the mentorship and friendship of Dr. Dieter Boeyaert and Dr. Marcos Xavier Navarro-González, particularly, for the many, many (non-)technical discussions. I am especially thankful to the 3DPSI family for welcoming me with open arms and for believing in me, especially when I was in the sea of chaos.

I would also like to thank the many contributions and fruitful technical discussions with (in alphabetical order): Nic. Allen, Prof. Allen Boozer, Prof. David Ennis, Dr. Michael Gerard, Prof. Greg Hartwell, Prof. David Maurer, Prof. Alkesh Punjabi, and Prof. John Schmitt.

Lastly, I would like to thank my friends and family who were my greatest support system during this journey. Your support from many hours of board games, biking, bad movies, and tea consumption brought me encouragement and joy. I am so fortunate to have made many friendships during my time in Madison, especially with Aysia Demby who began with me on day 1 in the 3DPSI group. I am also grateful to Prof. Saikat Chakraborty Thakur who encouraged me to pursue a PhD and continue research in plasma physics and fusion during my undergraduate days. Finally, I would like to thank my wonderful husband, Timothy Jancic, for going on this adventure with me and showing me endless kindness, love, and support over all these years.

Contents

List of Figures

List of Tables

Chapter 1

Motivation

A functional divertor solution is one of the key ingredients for the sustainment of a stable magnetically confined fusion reaction. For reference, the expected heat load on the International Thermonuclear Experimental Reactor (ITER) tokamak divertor is 10 MW/m^2 [1]. Thus, a divertor must be able to withstand high heat and particle flux. For a self-sustaining fusion reaction, this must be done in addition to preventing plasma core contamination from high-Z impurities as well as from helium "ash" generated by the fusion process.

A fusion reaction is the fusing of two light-weight nuclei which create a heavier one along with other products. This reaction can release an immense amount of energy. A candidate fusion reaction for fusion pilot plants is the deuterium ($^2_1$H) tritium ($^3_1$H) reaction, or D-T reaction which releases a total amount of 17.6 MeV:

$$^2_1\mathrm{H} +^3_1 \mathrm{H} \rightarrow \ ^4_2\mathrm{He}(3.5\mathrm{MeV}) + \mathrm{n}(14.1\mathrm{MeV}) \tag{1.1}$$

For a fusion reaction to occur, this requires very high temperatures of $> 10\,\mathrm{keV}$ where the D-T gas is in the plasma state. We also see from this reaction that a divertor must be able to provide a pathway for exhausting helium "ash" created by the fusion reaction away from the plasma. Thus, interaction between the plasma and material surfaces is inevitable, and this occurs in the physical region of a fusion device called the divertor. The divertor is the designated mechanical structure where power and particle exhaust occur.

Fusion ignition is the primary goal of fusion research in order to deliver a carbon-free energy source [2]. A common metric used to assess the output of a fusion reaction is the fusion energy gain factor Q. To achieve a self-sustaining fusion reaction, $Q \gg 1$ which is referred to as ignition. Prior to this "ignited" state, the plasma is "burning" when $Q > 1$ where break-even is defined as $Q = 1$ [3]. The condition for a self-sustaining fusion reaction can be summarized by the "fusion triple product":

$$nT\tau_E > 3 \times 10^{21} \mathrm{m}^{-3}\mathrm{keVs} \tag{1.2}$$

which indicates the minimum threshold for the triple product of number density (n [m^{-3}]), temperature (T [keV]), and confinement time of the plasma (τ_E [s]) and is a reformulation of the Lawson criterion [4]. Achieving a triple product above this threshold requires control of plasma impurities, since impurities can reduce each quantity of this triple product. Common impurities include neutral helium "ash" and sputtered material from the physical vessel wall that surrounds the plasma. Hence, the choice of divertor configuration and design is important for handling impurities along with managing the expected high heat load. Divertor research is an ongoing effort for magnetically confined fusion (MCF) devices of tokamaks and stellarators along with other MCF devices such as mirrors. The research topic of this work focuses on a new type of divertor for stellarators.

For future stellarator-based fusion energy, there are specific challenges regarding divertor design. A stable stellarator divertor concept must be robust with respect to plasma equilibrium changes. This is because promising optimized stellarator configurations undergo significant equilibrium changes as plasma pressure is built up. This is especially true for quasi-helically symmetric (QHS) and quasi-axisymmetric (QAS) devices, which will produce self-generated bootstrap currents at finite plasma pressure [5], [6]. These currents depend on the pressure profile, which in turn depends on the plasma transport, and therefore, it is hard to predict except in idealized cases [7]. Resonant divertors, such as the island divertor studied at W7-AS [8] and W7-X [9] [10]–[12], are very sensitive to the rotational transform profile. This is because small errors in the predicted current

could move the plasma edge islands where heat flux impinges on undesired regions of the wall. If the requirement to fix the rotational transform profile is removed, then there is significantly more configurational flexibility available. A divertor that functions similarly even as the plasma boundary is perturbed is referred to as resilient[1].

Current stellarator divertors include the island divertor concept which has been explored in W7-AS and W7-X [10]–[12] and the helical divertor in LHD [13]. The non-resonant divertor (NRD) is a divertor concept gaining traction as a viable candidate for stellarator fusion reactors. The helical troughs found in stellarator edges [14] are exploited in the NRD concept where a resilient field line intersection pattern on plasma facing components (PFCs) is observed across varying plasma equilibria, such as in HSX [15], [16] and in CTH [17], [18]. This wall intersection pattern is also known as the strike line or point pattern of the field lines and serves as a proxy for heat and particle flux.

This thesis will focus on the viability of the NRD as a resilient stellarator divertor solution. Chapter 2 provides a background on divertors in order to motivate the concept of NRDs. The chapter continues to describe what NRDs are based on previous work and provides an applied description of plasma edge chaos relevant for understanding NRD features. The computational tools which will be used for the analysis are also described in this chapter. In chapter 3, simulation of the Compact Toroidal Hybrid (CTH) [19], [20] with field line following and the 3D plasma edge transport code EMC3-EIRENE [21], [22] will explore the complex scrape-off layer (SOL) where a chaotic plasma boundary emerges while the overall strike line on the vessel wall remains resilient. CTH has a circular vacuum vessel allowing the study of these complex plasma edge features with respect to a simplified PFC geometry. The work shown in chapter 3 adds fundamental features to the understanding of NRDs for the rest of the thesis and is part of an ongoing effort for a future physical design of the NRD.

Next, simulation of the plasma edge in the Helically Symmetric eXperiment (HSX)

[1]There is no objective definition of "resiliency". In this document, we will prescribe a description of a resilient divertor to mean that it is stable across the different plasma configurations, which exhibit different magnetic structures in the plasma edge, studied in this work. More on this will be discussed on resiliency throughout this document.

[23] will be covered in chapters 4 and 5. An extended vessel wall [24], also referred as the "lofted wall" in this thesis, is used rather than the current wall in the experiment in order to analyze the impact of different plasma edge features across the selected equilibria studied. In chapter 4, the strike line on the lofted wall is found to be resilient across the scanned equilibria with varying edge field line behavior. This is further characterized by introducing a new metric we denote as the minimal radial connection $\min(\delta_N)$. This metric differentiates field line behavior from different edge structures within the characteristic resilient strike line of NRDs. Chapter 5 continues the HSX study by employing EMC3-EIRENE where the heat and particle flux deposition will be compared with the results of chapter 4. This chapter includes a basic analysis in the plasma transport behavior as a scoping study for studying detachment in HSX when the lofted wall is the main PFC. This analysis is given in context of the overall power balance and, in particular, power losses manifested through grid misalignment issues. This is important for future work in development of field-aligned stellarator grids used in EMC3-EIRENE to more accurately simulate the plasma transport in the HSX SOL.

The field line following metrics developed and applied throughout this thesis will then be applied to two magnetic configurations in W7-X in chapter 6. The selected high-performance magnetic configurations will be studied without the in-vessel island divertor components currently in W7-X. Since this divertor and its components are specific to the island divertor magnetic structure and geometry, the vacuum vessel is simulated as the main PFC. This is done as an initial survey in W7-X to identify the location, geometry, and structure for an NRD-like divertor solution.

Finally, a summary of the thesis work relating field line behavior and plasma transport for the study of resilient stellarator divertor behavior along with future work is provided in chapter 7.

Chapter 2

Background

This chapter is an overview of the relevant background information for the thesis work. Section 2.1 covers a general background on divertors to help motivate and introduce the NRD concept. A description of the NRD is given in section 2.2 where previous work is summarized. This section additionally provides a description of the relevant physics of chaotic systems which is a focus of this work for understanding the NRD features in the plasma edge. This is particularly important for also analyzing how these magnetic structures influence the open field line interaction with the PFC. Finally, section 2.3 is a brief description of the computational tools utilized for the analysis and results provided in chapters 3, 4, 5, and 6.

2.1 Divertor Background

Power and particle exhaust research has been one of the major challenges in the development of a fusion pilot plant and has been the subject of experimental and theoretical work from very early on in magnetic fusion research [25], [26]. Reference [27] shows that divertor research as a solution for power and particle exhaust began as early as magnetic fusion research itself in the 1950s. According to reference [28], the original purpose of the divertor was to screen impurities from the core plasma by creating a separate region, or in earlier designs, a chamber for plasma-material interaction (PMI). Screening of impuri-

ties is important since they can dilute the main plasma and thus cool down the plasma temperature, which is undesirable for sustaining a fusion reaction. Since then, the requirements of a divertor have expanded beyond merely impurity screening. Reference [25] breaks down four main areas of divertor research:

1. power dissipation
2. neutral particle exhaust
3. reduction of impurity production and screening impurities
4. helium exhaust, i.e. fusion "ash" removal

The divertor concept was initially discussed in context of stellarator application, and consequent divertor research continues in both tokamaks and stellarators.

This continued divertor research has lead to advancements in studying scrape-off layer (SOL) physics and overall reactor performance. The introduction of the divertor on the Axially Symmetric Divertor EXperiment (ASDEX) tokamak [29], for example, led to the discovery of high-confinement mode (H-mode) in 1982 [30]. The significance of this operational regime demonstrated an application of high heating power with improved high energy confinement time, which is beneficial to the fusion triple product mentioned in chapter 1. In contrast, low-confinement mode (L-mode) occurs when the high heating power leads to deterioration of confinement and hence low energy confinement time. Both modes studied at ASDEX were important for increased understanding of energy transport [30].

We next describe axisymmetric (2D) divertors. This description applies to tokamaks and helps establish the groundwork for describing stellarator divertor physics and geometry.

2.1.1 Axisymmetric (2D) Divertor

The name "divertor" arises from diverting the outermost shell of magnetic flux from the core plasma. We will first consider the axisymmetric divertor, which is effectively the

2D representation since it is symmetric around the torus. The magnetic field generated by the plasma current (B_θ^{plasma}) is diverted by introducing a magnetic field created by a divertor coil current (B_θ^{coil}). Here, the poloidal direction is indicated by θ and the toroidal angle by ϕ which can be seen on the right of figure 2.1 along with Z and major radius R. The point at which B_θ^{coil} cancels B_θ^{plasma} is called the X-point. This is a hyperbolic fixed point in the divertor configuration where B_θ^{plasma} exhibits diverging trajectories near the X-point. Hence, the divertor defines the last closed flux surface (LCFS), or separatrix, which separates the SOL and the core plasma made up of nested closed magnetic flux surfaces. This is demonstrated in figure 2.1 with the main plasma in red and with the SOL surrounding the main plasma. The field lines that are outside the LCFS and within the SOL are open and strike the divertor targets, shown blue in figures 2.1 and 2.2. The SOL domain of open field lines is the region which has direct contact with material surfaces. Another region defined by the divertor is the private flux region (PFR) bounded by the divertor "legs" of the X-point and the divertor target in blue. Particles and energy flow from the SOL to the PFR via cross-field transport.

In the unperturbed configuration described above, the flow of particles and energy from the core plasma toward and into the SOL is dictated by cross-field transport, with respect to the magnetic field direction. Within the SOL, parallel transport dominates and particles and energy flow toward the divertor targets along the open field lines. This is illustrated in figures 2.1 and 2.2 by the gray arrows.

Unlike a divertor which magnetically separates the confined region from the SOL, a limiter configuration introduces a material structure in nearly direct contact with the main plasma. A simple schematic is shown on the left of figure 2.1. This direct contact results in the mechanical structure limiting the radius of the main plasma. The gray arrows in the figure demonstrate the flow of particles and energy move from the confined plasma to the SOL via cross-field transport. The placement of this structure can be disadvantageous for plasma purity, however, since material erosion or sputtering of the limiter can introduce impurities directly into the confined plasma [33]. Since one of the

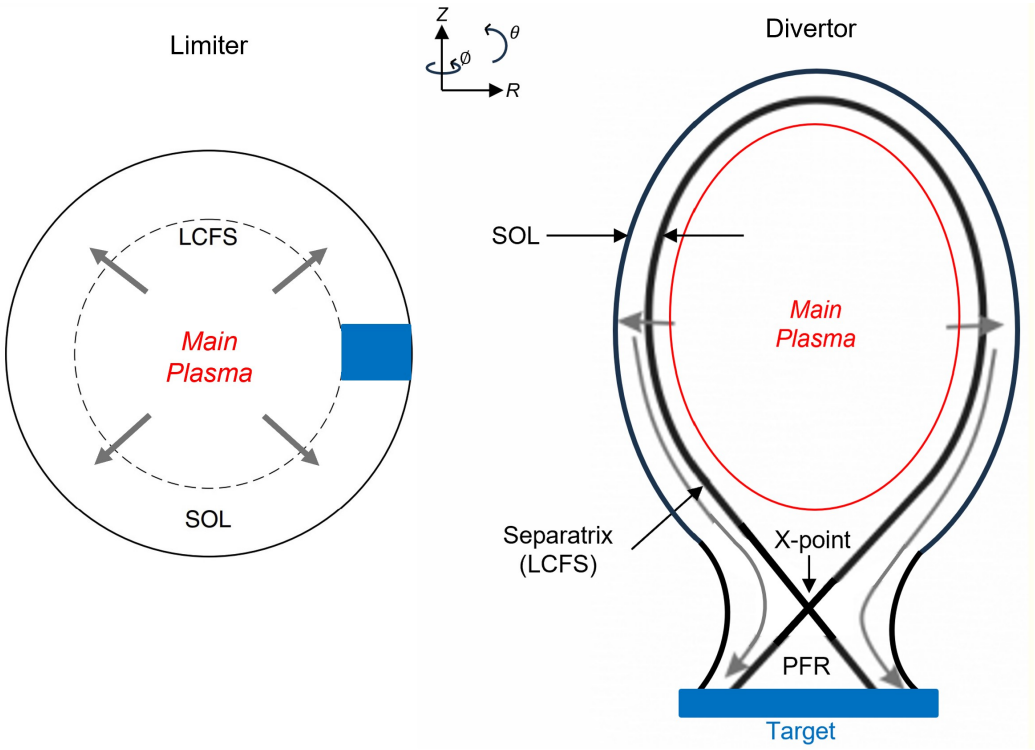

Figure 2.1: Figures adapted from references [31], [32] of a limiter (left) and divertor (right). Both configurations show how the main plasma (red) is separated from the scrap-off layer (SOL). The private flux region (PFR) is an additional region depicted in the single-null divertor example. The targets are blue and the flow of particles and energy are indicated as gray arrows.

main purposes of the divertor is to reduce impurity production and screen impurities, the increased separation between the physical target structure and the plasma helps address this issue. This increased separation is visible in figure 2.1 where the target is in direct contact with the SOL and PFR due to the location of the X-point.

In figure 2.2, a single and double-null divertor configuration are shown, where "null" refers to the X-point. The double-null features 2 X-points and the gray arrows show that energy and particles in the SOL can flow toward both blue targets shown. The single and double-null configurations are examples of 2 axisymmetric divertor configurations which are used in tokamaks. However, we will see in the next section that stellarators can have many more nulls and additional 3D SOL complexity which is discussed next.

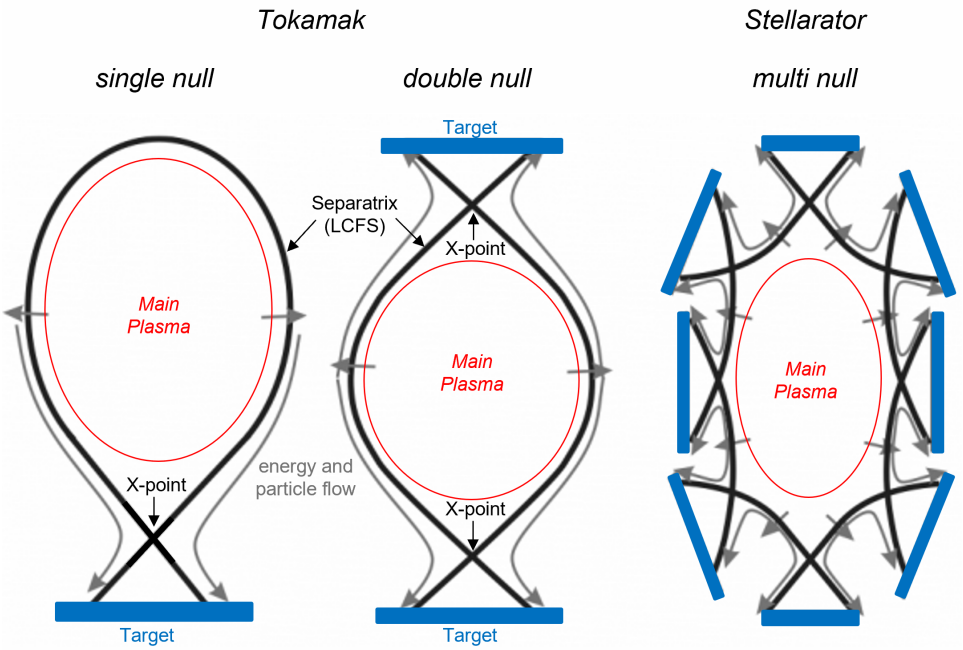

Figure 2.2: Figure adapted from reference [32] illustrating the single-null, double-null, and multi-null divertors from left to right, respectively.

2.1.2 Non-Axisymmetric (3D) Divertor

The description in this section now applies to stellarators whereas the previous case applies to tokamaks. We now consider the non-axisymmetric case, or the 3D divertor description where we cannot leverage toroidal axisymmetry as in the 2D case. For stellarators, the 3D nature of the SOL introduces more plasma edge complexity and, therefore, the required divertor targets must accommodate this. The rightmost plot of figure 2.2 shows the example of a multi-null configuration, which is the case for the island divertor in a stellarator. This is an example of a non-axisymmetric case which contrasts with the other two tokamak divertor configurations illustrated in the figure. In this configuration, the particle and energy flow is now more complex in the presence of 8 X-points, as shown in the figure. The complexity is also increased for this configuration since it is not toroidally axisymmetric like single and double-null divertors. The rest of this section discusses two non-axisymmetric divertors which have been built and experimentally tested in stellarator experiments.

The first type is the resonant divertor. In the resonant divertor configuration, an internal or external magnetic resonant perturbation is applied to a rational magnetic surface. A magnetic surface is rational when its rotational transform $\iota = \iota/2\pi$ satisfies $\iota = m/n$ where the poloidal and toroidal mode numbers m and n, respectively, are integers. In general, the rotational transform is defined as $\iota = d\psi/d\Phi$ where ψ is the poloidal magnetic flux and Φ is the toroidal magnetic flux. It is the ratio of poloidal transits to toroidal transits for a field line. The rightmost sketch in figure 2.3 shows the formation of a magnetic island along with its labeled X and O-point when the sufficiently large perturbed field's Fourier harmonic is resonant with the rational surface (red dashed line).

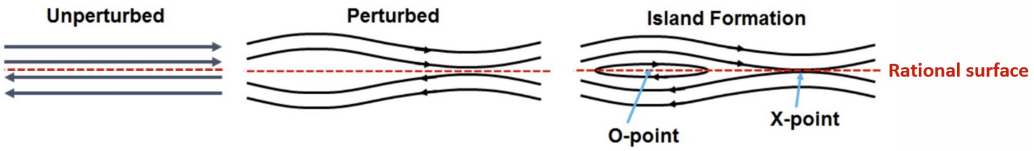

Figure 2.3: Simplified cartoon of magnetic island formation adapted from [34] when an applied magnetic field perturbation is resonant to a rational magnetic surface.

The island divertor at W7-X is an example of a resonant divertor [10]–[12]. The island divertor configuration relies on intrinsically or externally induced magnetic islands in the plasma edge where the divertor target is made to intersect the edge island. The magnetic shear, defined as $s \equiv \frac{r}{\iota}\frac{d\iota}{dr}$, is low and the islands remain large where they can be diverted by the target plates. The X-points of the islands, illustrated in the multi-null configuration of figure 2.2, serve the same purpose as the X-points in the tokamak single and double-null divertors. The islands positioned at the separatrix form a SOL where the field lines of the islands guide the energy and particle flow along the gray arrows depicted towards the targets in figure 2.2. The multi-null in this figure also shows the PFR regions accompanied with each X-point, like in the tokamak divertor. In addition to this figure, the island divertor in W7-X is also shown figure 2.4 from reference [35].

The leftmost plot of figure 2.4 shows that the island divertor is made to intersect the $\iota = \frac{5}{5}$ edge island structure created by the standard magnetic configuration which has

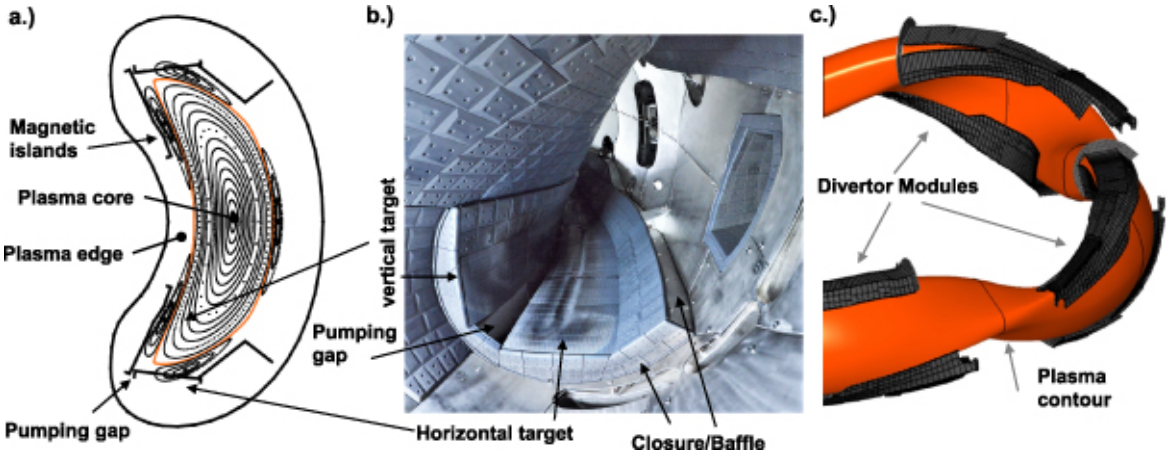

Figure 2.4: Figure from reference [35] illustrating the island divertor in W7-X in the standard magnetic configuration.

$\iota \sim 1$ at the plasma edge[1]. The island divertor can be quite sensitive to ι since changes in island size and the pitch of the field lines can affect the transport behavior [35]. In the rest of figure 2.4, the rightmost plot of the figure that the divertor is separated into different modules shown in black following the plasma contour shown in orange. The center image of figure 2.4 shows the physical vacuum vessel with the horizontal and vertical targets of the divertor along with its baffle.

Another non-axisymmetric divertor type is the helical divertor in the Large Helical Device (LHD) [13]. In the case of the helical divertor in LHD, diversion of the field lines is done internally by the helical coils as seen in figure 2.5 from reference [36]. The leftmost plot of figure 2.5 shows the two helical coils in gray which create a guide field for the plasma to follow. The LCFS is the yellow-green contour surface in this plot of figure 2.5. The middle of figure 2.5 shows a Poincaré plot of the magnetic field lines along the vertically elongated poloidal cross section. The right plot of figure 2.5 depicts the same quantities but for the horizontally elongated cross section in LHD. Labels a-h of figure 2.5 show the divertor tiles in red.

In the helical divertor configuration, the X-point in the plasma edge region greatly resembles the tokamak double-null divertor configuration described in the previous section

[1]In general, the largest islands emerge when the toroidal mode number n of ι is equal to the number of field periods of the stellarator. W7-X is a 5-fold symmetric device.

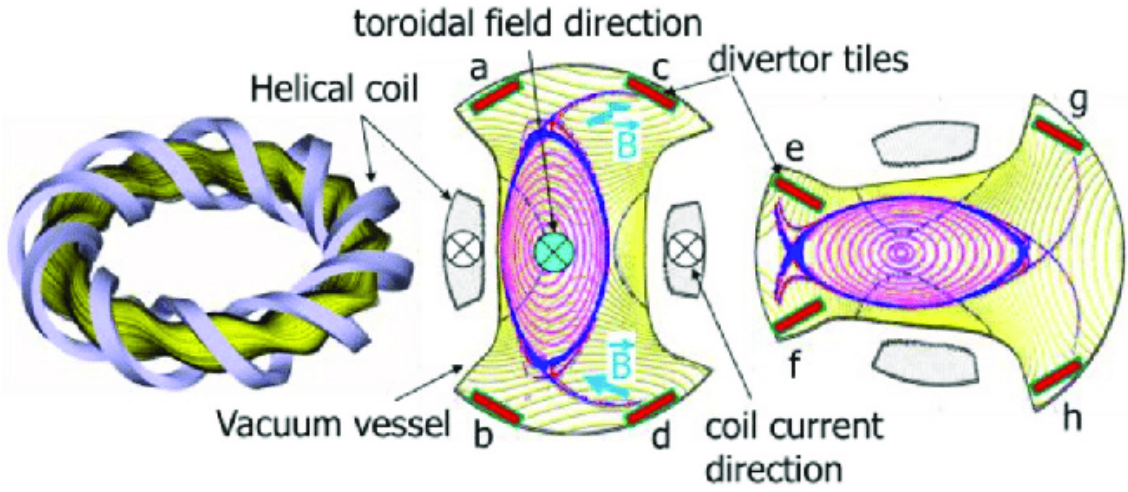

Figure 2.5: Diagram of LHD showing the helical divertor in the LHD standard magnetic configuration. This figure is from reference [36].

and shown in figure 2.2. This divertor, however, is not axisymmetric since the X-points rotate helically and the radial positions can shift. The resulting divertor footprint, or the magnetic field line pattern on the divertor, is therefore non-uniform both toroidally and poloidally. This X-point variation gives rise to a complex SOL. Further, figures 2.5 and 2.6 show that each poloidal cross-section has four divertor tiles and 2 X-points where the field lines are diverted for the SOL. Figure 2.6 plots the different connection lengths[2] L_C of the field lines in LHD. Outside of the LCFS (dashed black curve) in figure 2.6 of LHD, the complex SOL is comprised of remnant island chains (orange $\mathcal{O}(10^5\text{m})$) and the chaotic layer (light green to purple $\mathcal{O}(10^3\text{m}) - \mathcal{O}(10^1\text{m})$). Within the chaotic layer in figure 2.6 the divertor legs appear to be comprised of filamentary lobe-shaped L_C surface layers and extend beyond the X-points toward the divertor plates with $L_C \sim 2\,\text{m}$ [37]. Reference [38] describes the chaotic plasma edge in LHD formed from non-integrable magnetic fields. This will be discussed more in section 2.2. The chaotic layer is typically not exhibited in tokamaks, and if it is, it is significantly smaller in poloidal width compared to stellarators, and is yet another reason why this divertor configuration is different than the double-null tokamak divertor. In high magnetic shear devices like LHD, the plasma does not feature

[2]The connection length is defined as the target to target distance of a field line. In the core, field lines have infinite L_C while outside the LCFS their L_C is finite.

large edge island formation. Instead, a chaotic layer is formed by the overlapping of many different edge resonances [13], [39].

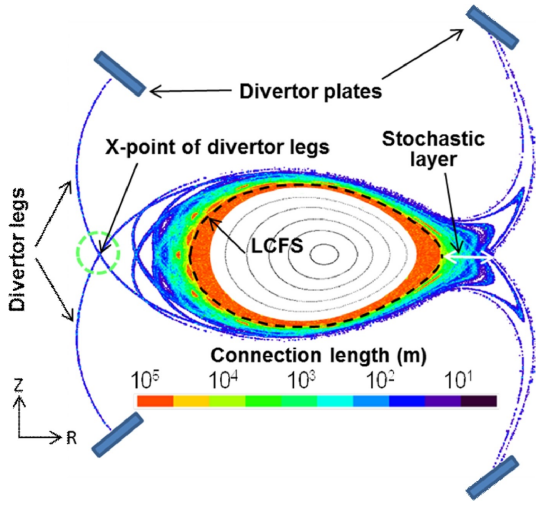

Figure 2.6: Another diagram of LHD showing the helical divertor in the LHD. This figure is from reference [40].

Figures 2.5 and 2.6 show that the helical divertor is further away from main plasma whereas in the island divertor case, the divertor is located close to the main core plasma. In contrast, figure 2.6 shows that the L_C can vary greatly from field line to field line, particularly in the chaotic layer. Hence, perpendicular transport becomes especially important in the SOL for stellarators in contrast to tokamaks.

We have introduced non-axisymmetric 3D divertors in this section and discussed two examples which have been used to date in stellarators. The third stellarator divertor concept the non-resonant divertor. This description is provided in 2.2. Before diving into this last stellarator divertor type, we provide an overview of divertor detachment. As these last sections introduced the differences in geometry and magnetic edge structure between tokamak and stellarator divertors, section 2.1.3 highlights the differences in SOL transport behavior and specifically detachment.

2.1.3 Detachment

A desirable regime of interest in the SOL is divertor detachment. A detached plasma scenario is attractive since it significantly reduces the heat flux seen on the divertor targets in order to avoid melting and erosion of the PFC. Even at low amounts of heat flux, however, plasma temperatures at the PFC can still be high enough that physical sputtering occurs. To avoid physical sputtering, the ion energy at the target must be below the work function of the material. Chemical sputtering can still occur in some materials and source unacceptable levels of impurities. Therefore, in addition to low heat flux, the particle flux needs to also "detach" from (or not be in direct contact with) the divertor target. We consider 2.7 to describe how full detachment is achieved with respect to the downstream divertor quantity trends as a function of the main plasma density (or upstream density).

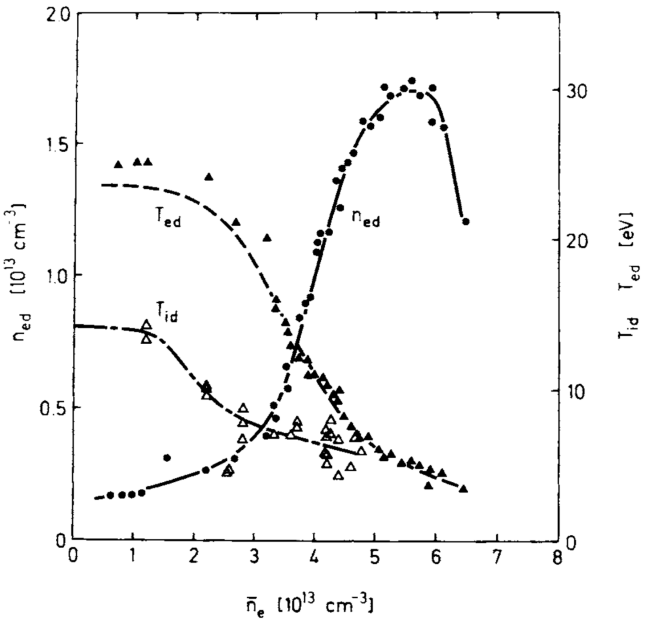

Figure 2.7: Figure from reference [41] demonstrating the density "roll-over" associated with the SOL transition into detachment in ASDEX.

In figure 2.7 Langmuir probe measurements in ASDEX are shown. The figure shows the downstream divertor quantities of electron density (n_{ed} (left y-axis) and target electron and ion temperature ($T_{\{e,i\}d}$) as a function of the line averaged density ($\overline{n}_e$). This assessment

allows to quantify the divertor regime as a function of the plasma core density, which is a main parameter in the fusion triple product mentioned in chapter 1. We see three different divertor regimes: low-recycling (sheath-limited), high-recycling (conduction-limited), and detached [31]. Following the curves plotted, the low-recycling regime is seen when $T_{\{e,i\}d} > 10\,\mathrm{eV}$, n_{ed} tends to increase linearly with $\overline{n}_e$. Next, the high-recycling regime occurs when the n_{ed} increases approximately cubically with $\overline{n}_e$. This regime features low T_{ed} accompanied with high particle flux and hence n_{ed} is larger than in the low-recycling regime. More generally, recycling is the process of neutrals, generated from the recombination of electrons and ions recombining at the PFC, becoming ionized in the plasma and returning to the material surface. The final regime shown in figure 2.7 is detachment where n_{ed} saturates and decreases with $\overline{n}_e$. Following the trend of n_{ed} in this figure, this demonstrates the density "rollover" commonly used to describe the SOL transition to detachment.

The detachment process at the PFC is driven by atomic and molecular processes of the recycling hydrogen plasma species and impurities [42], [43]. These references describe that, without impurities, the recycled neutrals at the target consume energy in the SOL via ionization energy losses and molecular dissociation. This results in a reduced power to the target and hence detachment of the heat flux (also referred to as energy or thermal detachment). However, to detach the particle flux, this is achieved via volumetric recombination of the incoming hydrogen ions to the target. This occurs at divertor electron temperatures of $\sim 1\,\mathrm{eV}$ which requires substantial volumetric power dissipation. Moreover, the downstream density needs to be high enough to facilitate this process. Thus, the high-recycling regime with $n_d \propto n_u^3$ is a necessity. A detailed description which distinguishes between energy, momentum, and particle detachment in tokamaks can be found in reference [44] .

The description above of detachment using figure 2.7 applies to tokamaks. This occurs as a transition from low to high-recycling. Previous work in stellarators observed different detachment behavior linked with the 3D SOL magnetic structure. In stellarators, it was

consistently seen that the ability to reach high-recycling was impeded. Rather, access to full detachment was limited to thermal detachment with marginal particle flux detachment [37], [45]. This lack in high-recycling was explained by momentum losses associated with counter-streaming flows of the 3D flux channels in the SOL. The upstream momentum loss results in particles not effectively streaming towards the divertor and therefore the downstream density condition is not met for high-recycling. This was seen at W7-AS, where the achievement of partial detachment via a high density H-mode (HDH) operational regime, and showed promise of the island divertor concept for future stellarators [10], [46]. However, the detachment occurred at high divertor temperatures ($> 3\,\mathrm{eV}$) resulting in insufficient volumetric particle recombination to avoid continuous particle flux to the divertor. Implementation of additional mechanical structure(s) in the divertor region can facilitate the mentioned physics criteria along with enhance neutral pressure accumulation and hence particle exhaust. The helical and closed helical divertor experiments at LHD have shown that this is possible by placement of baffling structures [47]. In W7-X, the island divertor was designed and installed for W7-X where stable detachment was achieved [35], but still without occurrence of high-recycling linked with limited downstream particle density and a relatively small neutral compression[3] in the divertor.

For stellarators, successful demonstration of detachment is important since this phenomenon is difficult to perform with complex divertor geometries [48]. Mechanical baffling as well as optimization of the edge magnetic structure is necessary to improve the recycling features of stellarator divertors. The difference in observed SOL behavior between tokamaks and stellarators for reaching detachment further emphasizes the importance of studying the plasma edge geometry. Moreover, this an open area of research for non-resonant divertors, which is the third stellarator divertor described next. We provide an overview on past NRD research and the relevant physics as a foundation for the thesis work.

[3]Neutral compression is defined as the ratio of the downstream to upstream neutral pressure [35]. High neutral compression indicates that there is an accumulation of neutrals downstream within the divertor region for stable pumping. Meanwhile, the upstream neutral density must remain small in order to avoid wall sputtering and build-up of a fast upstream neutral source which can inhibit plasma density control. In [35], small neutral compression in island divertor operation was linked to no observation of high-recycling.

2.2 Non-Resonant Divertor Description

2.2.1 Non-Resonant Divertor Background

The non-resonant divertor (NRD) is an alternative divertor solution for stellarators to the island divertor concept explored at W7-X or the closed helical divertor used at LHD [49]–[51]. The name arises from the fact that the NRD is not reliant on having a specific rotational transform value in the edge. This is in contrast to the island divertor discussed in section 2.1.2.

Previous work has shown that in NRDs, the overall magnetic structure on wall surfaces [51] and the deposited heat flux on the wall are resilient to changes in the plasma equilibrium, specifically to changes in the shape of the LCFS [15]. The resilient feature of the NRD concept can be categorized into

(a) features related to the magnetic structure and shape of the plasma boundary and

(b) features of the intersection pattern of escaping field lines on the wall, also known as the strike point or strike line pattern

If these features are maintained under a given plasma equilibrium change, we call the scenario resilient. The amount of allowed variation of the field line-wall interaction region depends on details of the mechanical divertor structure.

Resiliency of these categorical features were seen in previous results if 1) the LCFS was not limited directly by the wall and 2) large islands did not exist in the plasma edge [15]. In this thesis, we will discuss the magnetic structures that exist in the plasma edge in a series of magnetic equilibria in different stellarator devices. Topics such as resiliency and the transition between limited and diverted plasma wall scenarios will be discussed in the process of describing this evolution in chapter 3 for the CTH device. Results with HSX in chapter 4 will be used as a continuation of the results in reference [15] but with an expanded boundary [24] rather than with the current vessel wall. This is to computationally explore a wider plasma edge in HSX as a QHS configuration and to continue to examine how different magnetic structures influence the details of the NRD

characteristic resilient deposition pattern. Chapter 5 then simulates the plasma edge transport in the presence of an open chaotic layer to assess the viability of detachment in HSX with the lofted wall. Finally, an application of the newly implemented methodologies of the previous chapters will be applied to W7-X chapter 6 for a set of high-performing magnetic configurations as a scoping study of an NRD-like divertor structure within W7-X.

By modeling the plasma edge field line behavior in 3 different stellarator experiments, we focus on understanding the coupling of the magnetic structure in the plasma boundary to the overall resilient intersection pattern on different wall elements and the consequent heat deposition features. Specifically, we implement tools and methodologies to better understand the resiliency found in previous results. This is done in tandem with understanding the basic divertor and boundary transport aspects that form these divertor flux patterns. Previous research into these aspects have been performed on a limited number of devices including HSX [15], W7-X [14], and for a very limited configuration set in CTH [17].

2.2.2 Magnetic Field Line Hamiltonian

The description here follows the descriptions in [52]–[54]. We describe the magnetic field Hamiltonian for stellarators and tokamaks. The field lines of a divergence-free field are trajectories of a Hamiltonian system. For consistency with literature of dynamical systems, we denote the Hamiltonian $H = H(q, p, t)$, where q is the canonical position, p the canonical momentum, and t the canonical time. The Hamiltonian which describes field lines for a magnetic field $\vec{B}$ is the poloidal flux $\psi = \psi(\theta, \Phi, \phi)$ where the poloidal angle θ is the canonical position, the toroidal flux Φ is the canonical momentum, and the toroidal angle ϕ is time. The magnetic field $\vec{B} = \nabla \times \vec{A} = B_r\hat{r} + B_\theta\hat{\theta} + B_\phi\hat{\phi}$ can be expressed in the coordinates (θ, Φ, ϕ) as:

$$2\pi\vec{B} = \nabla\Phi \times \nabla\theta + \nabla\phi \times \nabla\psi(\theta, \Phi, \phi) \tag{2.1}$$

Hamilton's equations of a field line trajectory are then:

$$\frac{dq}{dt} = \frac{\partial H}{\partial q} \implies \frac{d\theta}{d\phi} = \frac{\partial \psi(\theta, \Phi, \phi)}{\partial \Phi} \tag{2.2}$$

$$\frac{dp}{dt} = -\frac{\partial H}{\partial p} \implies \frac{d\Phi}{d\phi} = -\frac{\partial \psi(\theta, \Phi, \phi)}{\partial \theta} \tag{2.3}$$

It is observed here that, in the case of axisymmetry (no explicit dependence on ϕ, $\frac{d\psi}{d\phi} = 0$), then ψ is a conserved quantity. As ϕ is our time-like variable, this is similar to a time-independent Hamiltonian which results in energy conservation. Since ψ is conserved, field line trajectories lie on continuous nested constant ψ surfaces which are invariant tori. In a 2D phase space, the topology is a circle. Moreover, since ψ is a constant of motion along a trajectory for a axisymmetric Hamiltonian (1D Hamiltonian), this system is therefore integrable.

Because of the 3D nature of stellarators, however, the dependence on ϕ the Hamiltonian becomes 1.5D [52], [55] and is no longer integrable since this would require 2 constants of motion. The results of Kolmogorov [56], Arnold [57], and Moser [58], also known as the KAM theorem, show that invariant surfaces may still exist. The KAM theorem describes the condition for invariant tori to exist. Consider a perturbed Hamiltonian H which is close to integrability:

$$H(q, p, t) = H_0(p) + \delta H_1(q, p, t) \tag{2.4}$$

where H_0 is unperturbed and integrable and δ is some perturbative parameter. One such condition for invariant tori to persist is if $\delta \ll 1$. Thus, invariant tori can exist even in the presence of perturbations away from axisymmetry. These surfaces, however, increasingly break up as δ increases and H deviates further away from integrability. A detailed treatment regarding deviations away from integrability can be found in [54]. Moreover, the trajectories in this region may be subject to X and O-point periodic motion of island structures, lie on cantori (partially broken tori which are partial barriers to transport), or exhibit chaotic behavior.

Chaos and Stochasticity

Before discussing relevant features in the plasma edge for NRDs, we delineate between chaotic and stochastic systems. This short description is meant as a primer to developing the relevant chaotic structures which emerge in magnetic fields.

In the literature, there are many sources on the topic of chaos, stochasticity, along with their similarities and differences [59]. This supplemental discussion is meant to aid the research to appropriately describe the relevant physics of interest. Put succinctly, a chaotic system is one that is deterministic while a stochastic system is not. After a long period of time, however, both chaotic and stochastic systems can exhibit similar features [59], [60]. A chaotic system, however, is one that is not random and in general has sensitivity to initial conditions. Two trajectories are described as chaotic if they diverge exponentially in a local phase space. A metric to calculate this exponential rate of divergence is called the Lyapunov exponent [61], [62]. The next subsection will discuss chaos with respect to magnetic fields when applicable. This specifically applies to plasma equilibria where chaotic structures in the plasma edge interact with the PFC.

2.2.3 Description of the NRD Chaotic Layer

The subsection is meant to provide an overview of the relevant chaotic magnetic structures specifically for the NRD features shown in the CTH results in chapter 3 and HSX in chapter 4. A short description of tangles, turnstiles, and their characteristic transport features is presented as they appear in the edge about hyperbolic fixed points. This is first discussed generally and then related to previous work in tokamaks and stellarators.

First, we discuss figure 2.8 which illustrates manifolds formed from trajectories in a chaotic dynamical system phase space. Figure 2.8 (i) (a) and (ii) (a) show a single X-point for a unperturbed and perturbed case, respectively. The X-points are defined by two intersecting manifolds, which topologically represent asymptotically approaching trajectories. In a 2D plot like figure 2.8, a manifold is the curve mapped out from the points of a trajectory's periodic orbit. Because these trajectories can be followed forward or backward,

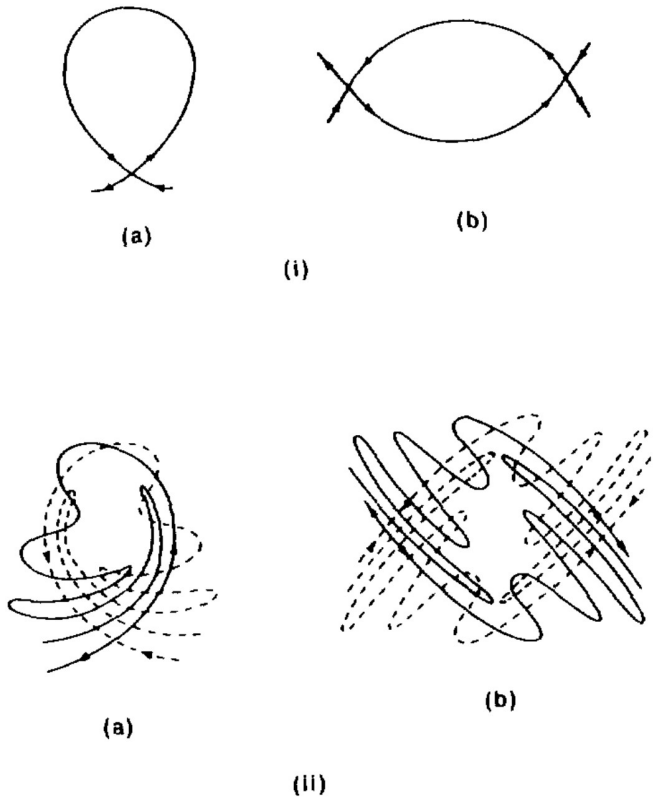

Figure 2.8: Figure reproduced from reference [62] illustrating manifolds formed from trajectories in a chaotic dynamical system phase space. Top row (i) showing an unperturbed single X-point (a) and double X-point (b). Bottom row (ii) showing a homoclinic tangle formed from the manifolds of a perturbed single X-point (b) and heteroclinic tangle formed from the manifolds of a perturbed double X-point. The dashed line is an stable manifold while the solid line is a unstable manifold.

they are generally referred to as unstable and stable manifolds which reference their direction. With respect to the X-point, the stable manifold can be seen as incoming while the unstable manifold is outgoing toward the hyperbolic point. In the perturbed scenario in figure 2.8 (ii) (a), these manifolds can have lobe-shaped, or finger-like, protrusions when projected onto one poloidal plane (a 3D visualization of an (a) unperturbed and (b) perturbed homoclinic manifold is shown in figure 2.9 which displays the 3D variation of an invariant lobes/fingers). The structure created by overlapping stable and unstable manifolds and their lobes of a single X-point is referred to as a homoclinic tangle shown in figure 2.8 (ii) (a). The dashed line is the stable manifold and the solid line is the unstable

manifold.

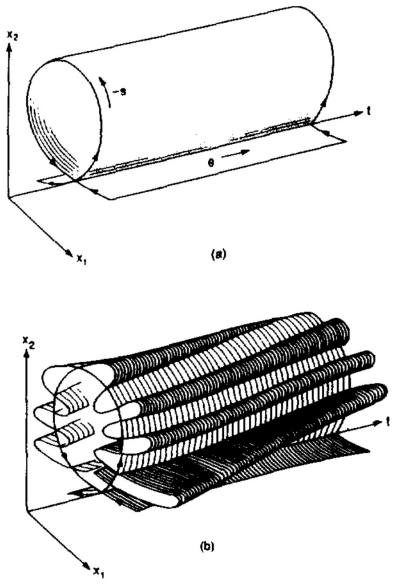

Figure 20. (*a*) An unperturbed homoclinic manifold in $X \times \mathbb{R}$; (*b*) an invariant lobe structure in $X \times \mathbb{R}$ for the perturbed case.

Figure 2.9: Figure from reference [62] illustrating (a) an unperturbed homoclinic manifold and (b) a perturbed homoclinic manifold with 3D variation.

This can be applied to magnetic field line trajectories where in the vicinity of a magnetic island (O-point), there will be an island separatrix that is defined by the set of field lines asymptotically approaching the island X-points. An example of this is shown in figure 2.10 tracing field lines in the DIII-D tokamak where a homoclinic tangle arises from a non-axisymmetric perturbation [63]. In this single null divertor configuration, the X-point can be clearly seen by the outermost open field line trajectories plotted in black in this figure. The homoclinic tangle formed about this X-point is formed by the overlapping of the oscillatory lobes of the forward and backward followed field lines. Topologically, this tangle is formed to preserve invariants in the phase space as the manifolds of the non-axisymmetric perturbation evolve with toroidal angle ϕ [63].

We now turn our attention to the scenario where there are multiple X-points, such as a double null configuration. Figure 2.8 (i) (b) and (ii) (b) shows the manifolds formed from unperturbed and perturbed orbits, respectively, where there are now two X-points. In this scenario, the lobes of a stable manifold of one X-point overlaps with the lobes of

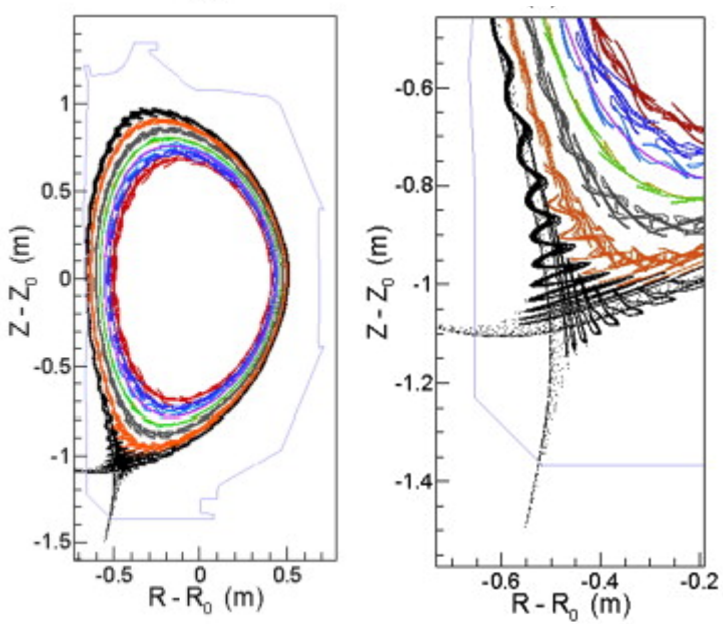

(a) Single null field line trajectories.

(b) Magnification of homoclinic tangle about the X-point in (a).

Figure 2.10: Figure reproduced from reference [63]

an unstable manifold from a different X-point. This results in a heteroclinic tangle. An example from field line trajectories where there are multiple X-points from multiple island chains can be seen figures 2.11 and 2.12 from reference [64]. We first discuss the formation of a heteroclinic tangle formed from a single island with two X-points shown in the right plot of figure 2.11. This plot focuses on the $m, n = 2, 1$ island with X-points $\times_0$ and $\times_1$ where we recall that m and n are the poloidal and toroidal mode numbers, respectively. The overlapping of the stable (W^s) and unstable (W^u) manifolds of each X-point create a heteroclinic tangle, much like what is depicted in figure 2.8 (i) (b) and (ii) (b).

The dynamics can become even more complex when multiple island chains are present in the plasma edge. This is often the case in highly perturbed stellarator edges and even in tokamaks as the next example will show in figure 2.12 from reference [64]. Here, we observe how neighboring island chain tangles interact with one another as a lobe of a stable manifold from one X-point can interact with a lobe of an unstable manifold of a different X-point. This is portrayed in figure 2.12 where a lobe of the green stable manifold $W^s(\times_0)$

of the $m, n = 2, 1$ island chain overlaps with a lobe of the blue unstable manifold $W^u(\times_1)$ of the $m, n = 3, 1$ island chain. Such interactions introduce more complexity of the transport in this region by demonstrating how magnetic flux exchange occurs between neighboring island chains and contribute to radial transport in the edge [64]. Similar complex transport behavior occurs in the plasma edge of LHD where a wider chaotic region is featured in the helical divertor as described in section 2.1. Figure 2.6 showed that the connection length can vary greatly in the edge and this is similarly the case for NRD magnetic configurations with a wide open chaotic layer. This is not the case for island divertors and tokamaks that feature a smaller chaotic layer compared to stellarators.

The island divertor's long connection length can be explained by considering the magnetic shear s. The connection length, in tokamaks, as an approximate measure of X-point to X-point distance is described by $L_C = 2\pi Rq/N$ where R is major radius, N is the null number, $q = 1/\iota$ is the safety factor. For stellarator island divertors, however, the expression can be altered to $L_C = 2\pi R/N\iota_i$ where $\iota_i = r_i s$ and r_i the island width [32]. Here, the quantity ι_i represents how field lines are directed from the plasma core to the targets. Thus, for particularly low-shear stellarators, the connection lengths are much longer ($\mathcal{O}(10^2\mathrm{m})$) than in tokamaks ($\mathcal{O}(10\,\mathrm{m})$) since $L_C \propto s^{-1}$ [32]. Moreover, this is not the case of LHD which was designed to exhibit high shear in its plasma edge [13] and therefore has great variation in its L_C due to the chaotic field line structure.

2.2.4 Effect of Magnetic Structure on Plasma Transport

In reference [63] they demonstrate that the homoclinic tangle influences the heat and particle target deposition, however, with sufficient diffusion, the internal effects of the tangle on the magnetic footprint tend to be washed out. In this thesis, we will also examine the impact of these structures and, while diffusion may obscure the details of the overall heat and particle flux on the PFC, these lobes still influence the overall target deposition. This behavior described is a well-known structural phenomenon from periodically perturbed Hamiltonian systems as described for instance in references [61], [65]–[67]. Previous work

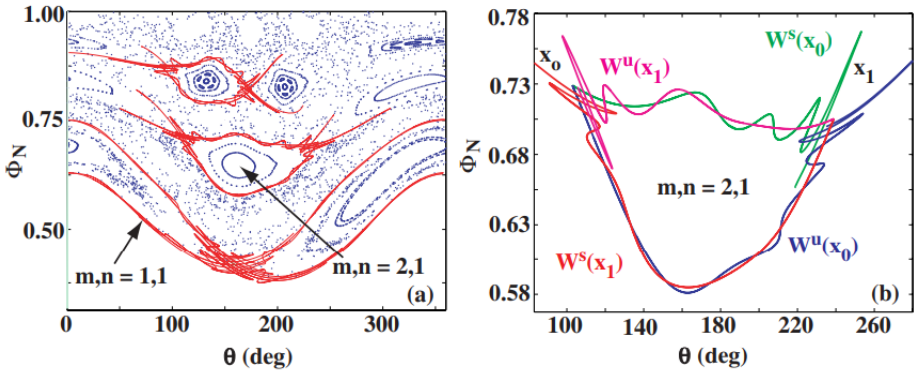

Figure 2.11: Figure from reference [64]. Figure (a) showing a Poincaré map in the radial coordinate Ψ_N on the y-axis and θ along the x-axis where the resonances $m, n = 1, 1$ and $m, n = 2, 1$ are included. The heteroclinic tangle formed here is from the interaction of lobes from the manifolds shown. Figure (b) is the conceptual illustration of overlapping manifolds showing heteroclinic tangles.

in tokamaks has shown the impact of the finger structures formed by the homoclinic and heteroclinic tangles which influence the heat and particle flux striation patterns discussed in [64], [68]–[70].

The link between the open chaotic edge structure and the ι values at the plasma edge has been discussed in references [71]–[73] for the cylindrical tokamak configuration at the TEXTOR-DED experiment. In references [74], [75] it was observed that the finger structures that are formed by the intersecting homoclinic tangles are comprised of shorter connection length magnetic flux tubes. Similar effects for such chaotic systems have also been found in the chaotic boundary structure at Tore-Supra [65], [76].

Because of the symplectic nature [66], [72], [77] of the magnetic field in this chaotic system, these flux bundles represent SOL channels that deposit heat and particles fluxes in their intersection zone with the wall elements. Previous theoretical work has shown that the open field line structure in the chaotic layer of NRDs guiding field lines to the wall are magnetic turnstiles [50], [78]. In this context, a turnstile represents a path for a magnetic field line to transit between regions that are otherwise not connected [61]. These turnstiles create a pathway that brings field lines, and therefore plasma particles, radially outward from the tangles and eventually deposits them on the target. They are the reason

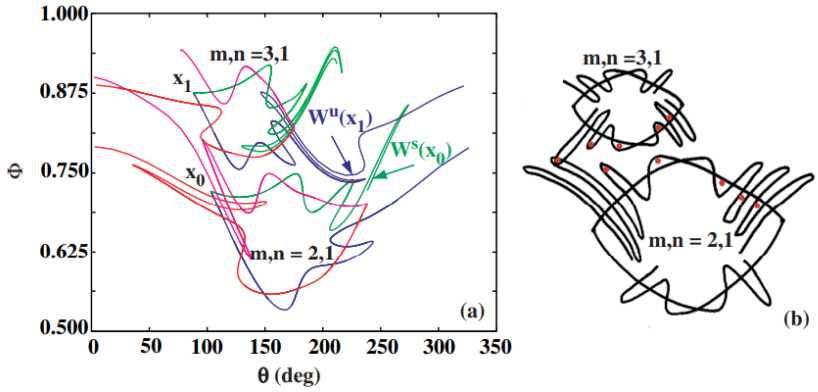

Figure 2.12: Figure from reference [64]. Figure (a) showing the interaction of a heteroclinic tangle formed from the unstable manifold $W^U(\times_1)$ in blue from the X-point $\times_1$ of the $m, n = 3, 1$ resonance with the stable manifold $W^S(\times_0)$ in green from the $m, n = 2, 1$ resonance with X-point $\times_0$. Figure (b) is the conceptual illustration of overlapping manifolds showing heteroclinic tangles.

that the escaping field lines intersect the wall in a confined helical band. The mechanism of the turnstile is discussed in detail in [51], [61], [78]. Recent work related to NRDs and their topology is a subject of ongoing work [79].

We will discuss the relation of the heteroclinic tangles and the SOL flux tubes which connect to the wall via the intersection pattern in chapter 3 for CTH. The tangles and turnstiles define the behavior of: the magnetic field lines in the plasma edge, the resulting strike line pattern on the wall, and therefore, the heat deposition on the PFC elements. As the edge changes, and additional chaotic structures appear, the pattern on the wall can change as well. This is examined in further detail in HSX in chapter 4 where we will introduce a new metric which will provide insight regarding field lines making up the resilient strike line are associated with island-like features or structures such as cantori and turnstiles. This will then be related to the simulated heat and particle flux on the HSX boundary. Relating the magnetic edge structures to the changes in the field line wall behavior is the main focus of this work.

2.3 Plasma Edge Modeling Tools

This section is an overview of the computational tools used for the bulk of the thesis work. To investigate NRD magnetic field edge structures and its performance as a divertor, a plasma equilibria is needed for each scenario. First, a description for generating plasma equilibria is provided. Once this is generated, it can be used to perform field line tracing and can finally be used for divertor performance predictions using a 3D plasma edge transport and neutral particle code. Descriptions of these tools are provided below.

2.3.1 Generating Equilibria for Analysis

To computationally analyze different magnetic equilibria across different devices in this thesis, we have taken two different approaches for computing the magnetic field. For situations where the current and pressure effects within the plasma are small, such as in HSX and W7-X, we use the vacuum field generated from the coils. Because the equilibria of interest for CTH are ohmically driven[4], there is an internal plasma current. We apply a different equilibria generation procedure for this case described here.

A Variational Moments Equilibrium Code (VMEC) simulation [80] establishes a magnetohydrodynamic (MHD) equilibrium solution. The code solves for the ideal MHD force balance $\vec{j} \times \vec{B} = \nabla p$ where p is the plasma pressure and the current $\vec{j}$ is related to the magnetic field $\vec{B}$ by Ampere's law $\mu_0 \vec{j} = \nabla \times \vec{B}$. Assuming nested magnetic flux surfaces and Fourier decomposing the components of the force balance, the code takes in an initial guess of the flux surface geometry and solves the force balance in real space to output the Fourier coefficients $R_{m,n}$, $Z_{m,n}$, $\lambda_{m,n}$ of cylindrical coordinates (R, Z, ϕ)

$$R(\theta, \phi) = \sum_{m,n} R_{m.n} \cos\left(m\theta - n\phi\right) \tag{2.5}$$

$$Z(\theta, \phi) = \sum_{m,n} Z_{m.n} \sin\left(m\theta - n\phi\right) \tag{2.6}$$

[4]This current is driven via Faraday's law where an increasing magnetic field in a solenoid is placed in the center of the CTH torus.

and streaming function λ where ϕ and θ are the toroidal and poloidal angle, respectively [80], [81]. A virtual casing calculation on the VMEC equilibrium is needed to determine the plasma contribution to the field outside the LCFS to prepare for field line tracing. The magnetic potential from the virtual casing calculation is added to the result of a Biot-Savart calculation of the coils themselves, producing a continuous vector potential, $\vec{A}_{Total} = \vec{A}_{Plasma} + \vec{A}_{Coils}$. The magnetic field is derived from the relation $\nabla \times \vec{A}_{Total} = \vec{B}$. This process ensures a divergence-free magnetic field throughout all space. These steps are carried out by the BMW code [82].

We note that for higher performing and optimized stellarators, there is a self-generated, or "bootstrap", current which can be difficult to model. For all the magnetic equilibria in this thesis, the self-generated current is negligible and thus ignored.

2.3.2 FLARE

The magnetic field structure can be analyzed using the Field Line Analysis and Reconstruction Environment (FLARE) code [83]. FLARE requires a geometric boundary representation[5] in addition to a magnetic field model representation[6]. It can be used for field line reconstruction for both axisymmetric equilibrium fields, like tokamaks, and non-axisymmetric configurations, such as stellarators. In tokamaks, the magnetic field can be defined as a superposition of non-perturbed and perturbed field. Stellarators, however, primarily rely on complex external coils for magnetic confinement of the plasma. We note that the magnetic field structure within stellarators can be altered since stellarators also generate some internal current. These changes are minor and will be ignored in this thesis.

FLARE contains tools for its own field line analysis tasks along with tools to construct field aligned grids for plasma boundary codes such as EMC3-EIRENE. Using the same magnetic field description in cylindrical coordinates in section 2.2.2, we describe how the field lines are traced in FLARE. For an initial point $\vec{p} = (r_0, z_0, \phi_0)$, field lines are

[5] These can be walls, divertor targets, and other plasma facing components (PFCs).
[6] Alternatively, the magnetic field can be calculated from a coil file input.

constructed by integrating this system of ordinary differential equations:

$$\frac{dr}{d\phi} = \frac{rB_r}{B_\phi} \tag{2.7}$$

$$\frac{dz}{d\phi} = \frac{rB_z}{B_\phi} \tag{2.8}$$

where we recall that ϕ is the time-like variable such that $\vec{F_p}(\phi) = (r, z)$ and $\vec{F_0}(\phi_0) = (r_0, z_0)$, where $\vec{F_p}(\phi)$ is a field line through $\vec{p}$. Here, ϕ is defined in the counterclockwise direction but can be followed counterclockwise and clockwise[7]. This system of equations is solved in FLARE by a Runge-Kutta method [84] where an adaptive step-size is implemented for error control. The estimated error is compared to a given tolerance parameter ϵ. This is particularly useful for tasks such as generating Poincaré plots and mapping flux surfaces such as what is seen in figures 2.6 and 2.4 (a).

The main area of interest in this thesis is the field line behavior in relation to the stellarator boundary. FLARE requires the input for the geometric boundary to be in so-called Kisslinger format where the cylindrical coordinates (r, z, θ) of the PFC are stored for each finite step of the toroidal angle ϕ for both axisymmetric and non-axisymmetric PFCs. FLARE does not take into account the material properties of the boundary and only keeps tracks of intersections of the field lines with the PFCs. For a field line trajectory from $\vec{p}_1$ to $\vec{p}_2$, FLARE checks if this trajectory intercepts a material surface when the intersection point $\vec{p}_x$ satisfies the linearized equation

$$\vec{p}_x = \vec{p}_1 + t(\vec{p}_2 - \vec{p}_1), \qquad t \in [0, 1] \tag{2.9}$$

This is combined with the polygonal representation of the provided boundary surface. In this example, the polygonal representation of an axisymmetric surface is noted as $\vec{c}_i$ with

[7] Also referred to as forward and backward or increasing and decreasing.

M segments

$$\vec{c}_i = (r_i, z_i) \qquad i = 0, ..., M \tag{2.10}$$

$$(r_x, z_x) = \vec{c}_i + s(\vec{c}_{i+1} - \vec{c}_i), \qquad s \in [0, 1] \tag{2.11}$$

where 2.9 and 2.11 are 2 linear equations for s and t. The component ϕ_x is found via 2.9 and is related to the i_{th} polygon segment through the tuple $\vec{u} = (\phi_x \bmod 2\pi, i + s)$. A similar procedure is followed for non-axisymmetric surfaces, however, it is complicated by the dependence in ϕ. These details are described further in [83].

The workflow for analyzing the field line behavior across various magnetic equilibria within the different stellarators involves identifying PFCs followed by generating various surfaces or points to launch and trace field line trajectories. An example of this is simulating the magnetic footprint along PFCs which has been done in previous work to analyze how field line behavior influences deposition of heat and particles on PFCs [85]–[87]. In addition to the magnetic footprint, another method for approximating the location of heat and particle flux is by simulating field line diffusion to mimic particle transport [15], [63]. For this, field lines are launched inside of the LCFS on a closed magnetic flux surface grid where a displacement Δ is applied to the followed trajectories after each integration step. The displacement takes the form $\Delta = \sqrt{4\mathcal{D}s}$ where s is arc length and $\mathcal{D}$ can be related to the velocity along a field line u and cross-field diffusivity D as $\mathcal{D} = D/u$. This displacement is added in a random direction of the trajectory within the poloidal plane of the trajectory.

The FLARE calculations described can vary in computing time depending on the number of trajectories followed and the level of diffusion (if applicable). Using the high performance computing resource at the Center for High Throughput Computing (CHTC) at the University of Wisconsin-Madison [88] we use up to 4 nodes for a FLARE calculation on a dense mesh. For field line diffusion, these can take up to 6 hours and for magnetic footprints where the majority of field line trajectories are short, this can take up to an hour.

Throughout this thesis, we will use the flexibility in the initial point distribution and the availability of different FLARE output results to define the magnetic stellarator divertor features for NRDs. These results and their application will be discussed in chapters 3, 4, and 6.

2.3.3 EMC3-EIRENE

Field line following gives us insight regarding the behavior of the magnetic structure present in the plasma edge. This can also provide a first estimate of the anticipated location of the heat and particle flux on the PFC. However, for a more robust analysis of the 3D nature of the SOL in these complex plasma edge configurations, we employ a higher fidelity code to simulate SOL transport. This will be addressed using EMC3-EIRENE which is a fully 3D plasma edge fluid Monte-Carlo code (Edge Monte Carlo 3D (EMC3)) coupled to a kinetic neutral transport model (EIRENE) [21], [22]. These are computationally expensive calculations and, therefore, are restricted to a smaller selection of configurations to simulate out of the all of the configurations modeled with FLARE. The results from this edge transport modeling are later compared to the field line tracing results.

EMC3-EIRENE is the standard edge code used in stellarator divertor and SOL research [89]–[92] and is also commonly used in nominally axisymmetric systems that include 3D perturbations, such as tokamaks under the influence of resonant magnetic perturbations [86], [93]–[95]. EMC3 solves for the steady state plasma temperature and density via locally field-aligned fluid equations (Eq. 2.12-2.15) for a given 3D magnetic mesh geometry. EIRENE simulates neutral behavior sourced from plasma striking the provided boundary and PFCs for the simulation. Particles at these physical boundaries are handled via a reversible field line mapping (RFLM) technique [21], [96]. This field line mapping along with flux tube mesh implementation reversibility allows efficiency particularly in modeling complex and anisotropic plasma edge transport. Iterating between the EMC3 fluid solution and the EIRENE neutral interactions provides a self-consistent solution for the SOL where

momentum, energy, and neutral transport are solved separately on an iteration basis. EMC3-EIRENE solves the following fluid equations:

$$\nabla \cdot \left(n_i V_{i\parallel} \vec{b} - D_i \vec{b_\perp} \vec{b_\perp} \cdot \nabla n_i \right) = S_p, \tag{2.12}$$

$$\nabla \cdot \left(m_i n_i V_{i\parallel} V_{i\parallel} \vec{b} - \eta_\parallel \vec{b}\vec{b} \cdot \nabla V_{i\parallel} - \mu_\perp \vec{b}_\perp \vec{b}_\perp \cdot \nabla m_i n_i V_{i\parallel} \right) = -\vec{b} \cdot \nabla p + S_m, \tag{2.13}$$

$$\nabla \cdot \left(\frac{5}{2} n_e T_e V_{i\parallel} \vec{b} - \kappa_e \vec{b}\vec{b} \cdot \nabla T_e - \frac{5}{2} T_e D_i \vec{b_\perp} \vec{b_\perp} \cdot \nabla n_e - \chi_e n_e \vec{b_\perp} \vec{b_\perp} \cdot \nabla T_e \right) = -k \left(T_e - T_i \right) + S_{ee}, \tag{2.14}$$

$$\nabla \cdot \left(\frac{5}{2} n_i T_i V_{i\parallel} \vec{b} - \kappa_i \vec{b}\vec{b} \cdot \nabla T_i - \frac{5}{2} T_i D_i \vec{b_\perp} \vec{b_\perp} \cdot \nabla n_i - \chi_i n_i \vec{b_\perp} \vec{b_\perp} \cdot \nabla T_i \right) = +k \left(T_e - T_i \right) + S_{ei}. \tag{2.15}$$

The fluid equations represent conservation of mass (Eq. 2.12), conservation of momentum along $\vec{b}$ (Eq. 2.13), and conservation of energy for electrons and ions (Eq. 2.14 and Eq. 2.15 respectively) where $\vec{b}$ is the unit vector along the magnetic field and $\vec{b_\perp}\vec{b_\perp} = \overleftrightarrow{I} - \vec{b}\vec{b}$ with $\overleftrightarrow{I}$ as the unit tensor. The perpendicular transport coefficients D_i, χ_i, and χ_e represent the cross-field particle diffusion, the thermal diffusivity for ions and the thermal diffusivity for electrons, respectively. $V_{i\parallel}$ is the parallel ion velocity, $\mu_\perp$ is the perpendicular viscosity, $\eta_\parallel$ is the parallel Braginskii viscosity, and $k = 3 n_e \nu_e m_e / m_i$. In EMC3, $\mu_\perp = D_i$ for simplicity. The coupled fluid equations are solved while keeping the source terms fixed. These 4 source terms are particle (S_p), momentum (S_m), and energy (S_{ee} and S_{ei} from electrons and ions respectively). The losses from impurity radiation ($S_{e,imp}$) can be added to S_{ee}. These source terms capture the neutral particle interaction with the plasma via ionization/recombination, charge exchange, molecular dissociation, and excitation/radiation.

Next, we note the following assumptions present in EMC3. Because the cross-field coefficients of D and χ are input parameters, these values do not change in the simulation. The plasma model in EMC3 also assumes no drift contributions in equations 2.12-2.15. Furthermore, the magnetic equilibrium input is fixed and does not evolve over the iterative simulation scheme. It should be noted that while EMC3-EIRENE has the capability of

including trace impurities in the simulation, the results in this thesis will ignore impurities and only simulate pure hydrogen plasmas. The input power and density are prescribed along a toroidally topological surface as initial conditions on the plasma. The input power is through the LCFS and the input density is typically defined at the separatrix (which is also referred to as the upstream or separatrix density). The recycling flux is computed and adjusted while this upstream density is held constant. Finally, the Bohm condition is imposed on the PFCs.

The outputs of EMC3-EIRENE include the temperature, density, and Mach flow through the plasma edge along with the neutral particle density. The main results relevant to this thesis from EMC3-EIRENE are the simulated heat and particle flux on PFCs across the different stellarator geometries and magnetic configurations. These results will be compared with the simulations performed with FLARE. EMC3-EIRENE simulations are the final step in the analysis workflow from studying the impact of the varying edge field line behavior.

Once a field-aligned mesh is obtained (described in the next section) iteration between EMC3 and EIRENE is necessary to achieve a self-consistent solution. We use the high performance computing resource at the Center for High Throughput Computing (CHTC) at the University of Wisconsin-Madison [88] and the National Energy Research Scientific Computing (NERSC) Center, a DOE Office of Science User Facility supported by the Office of Science of the U.S. Department of Energy under Contract No. DE-AC02-05CH11231 using NERSC Award FES-ERCAP0028693. Typically, 40,000 particles and 8 nodes were used for each EMC3-EIRENE simulation for the device size and scale of CTH and HSX. To reach a converged solution, this can take at least 30 iterations where each iteration can take at least an hour. These times can vary, however, based on the set boundary conditions and the plasma state (such as detachment) of each simulation.

2.3.4 FLARE Magnetic Mesh Generation

As mentioned, FLARE provides a suite of tools that can be leveraged for generating field-aligned grids for codes such as EMC3-EIRENE. A magnetic mesh is useful for fast reconstruction of field line segments[8]. This is particularly advantageous for EMC3 since the code requires repeated evaluation of field line segments. A description of this mesh generation process for EMC3-EIRENE using the example of the 10 kA case for CTH is provided below. The details of this configuration are discussed in chapter 3 where it is the most chaotic case out of all the magnetic configurations simulated for CTH.

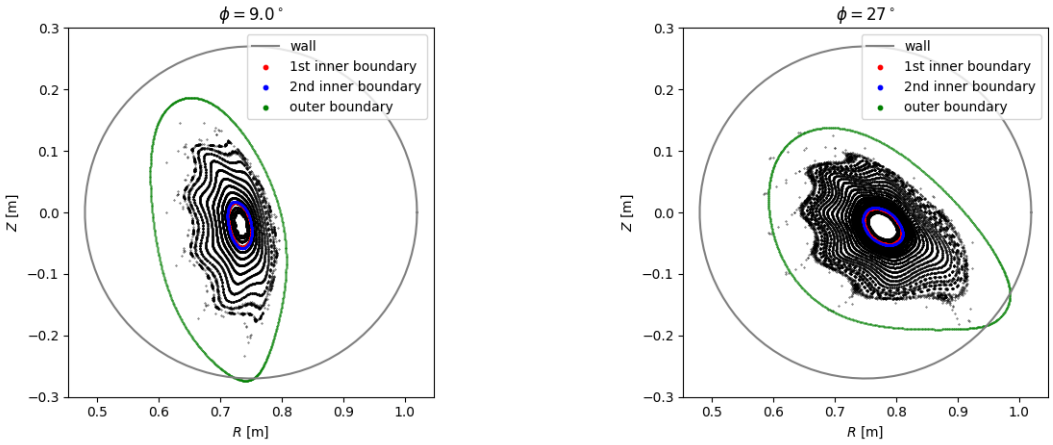

(a) $\phi = 9°$ plasma boundaries

(b) $\phi = 27°$ plasma boundaries

Figure 2.13: Poincaré map in black at $\phi = 9°$ (a) and $\phi = 27°$ (b) for one of the 6 magnetic configurations studied in CTH in chapter 3. The inner boundary surfaces are shown in red and blue, the outer plasma boundary in green, and the wall is gray.

EMC3-EIRENE requires a grid with two domains - one for simulating plasma processes and the other which will track neutral particles. The latter does not require magnetic field information. As EMC3-EIRENE is a plasma edge code, it does not solve for the plasma core region. For modeling edge plasmas of large-scale devices, the grid domain does not need to extend toward the plasma core region. However, for the example of CTH described here which is a low density stellarator, the plasma domain should be large enough such that most neutrals are ionized in the plasma domain. This explains why the magnetic mesh

[8] In general, due to the strong anisotropies in plasma behavior, field-aligned meshes can help improve accuracy for both Monte Carlo and deterministic methods.

represents the majority of the volume as shown in figure 2.14. The following paragraphs explain the grid generation procedure for the example of the 10 kA case in CTH starting with the plasma domain and followed by the neutral domain.

First, an inner and outer boundary of the plasma domain is required for an EMC3-EIRENE simulation as the plasma domain must be an annular domain. The inner boundary requires identification of two good closed flux surfaces, which can be identified via a Poincaré map. Figure 2.13 displays the $\phi = 9°$ and $\phi = 27°$ Poincaré map for the CTH 10 kA case with their selected inner boundaries. Because stellarators have up-down symmetry[9] and CTH has 5-fold symmetry, we can simulate the first half-field period spanning $\phi \in [0°, 36°]$ for this case. The red and blue surfaces in the figure 2.13 are the inner boundaries of the plasma domain.

Next, the outer boundary must be identified. A constraint on specifying the outer boundary is that it must intercept a PFC. For a limited plasma wall scenario, the outer boundary can be chosen at or just inside the LCFS if the flux surface intercepts the PFC. In non-limited magnetic configurations, this is not the case. This becomes even more challenging for cases like figure 2.13 where the field lines in the edge become chaotic and the surfaces just beyond the inner boundaries are quite corrugated. These field lines which do not sufficiently extend beyond plasma exposed surfaces can lead to gaps in the mesh where field lines may travel too radially inward. Hence, the green curve in figure 2.13 extends beyond the LCFS to include the chaotic plasma edge region in this equilibria and intercepts the boundary, which is shown in figure 2.14 at $\phi = 9°$ and $\phi = 27°$. We note that the PFC here is an axisymmetric surface located at $r = 27$ cm depicted in the figure as the gray circle in figure 2.13.

Once the plasma domain is specified by identifying these inner and outer boundaries, this is followed by construction of a 2D base mesh at specific toroidal locations. Other toroidal locations of the base mesh are generated by following field lines across the toroidal domain. For the example case here, the complexity of the plasma edge of the CTH 10 kA case is an example of an EMC3 grid which requires that the toroidal domain is split into

[9] A half-field period is the up-down mirror of the next half-field period.

multiple toroidal blocks. This case features a chaotic region causing large radial excursions of the field lines which in turn deforms flux tubes in the edge. Furthermore, the flux surfaces appear quite corrugated beyond the inner boundaries previously identified for the plasma domain. For this simulation, the two toroidal domains are one from $\phi \in [0°, 18°]$ and the other from $\phi \in [18°, 36°]$. This is why figure 2.13 shows the inner and outer plasma boundaries at $\phi = 9°$ and $\phi = 27°$ since these locations are halfway through each toroidal block. From these two blocks, two 2D base meshes are then generated.

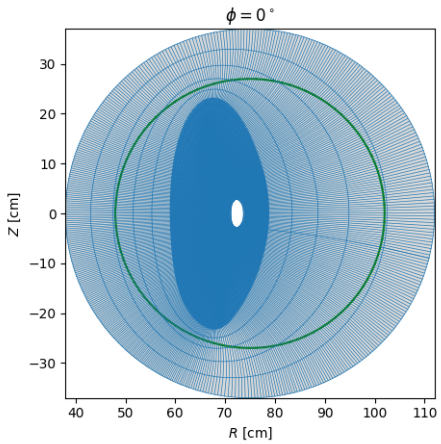

(a) $\phi = 0°$ grid cross section

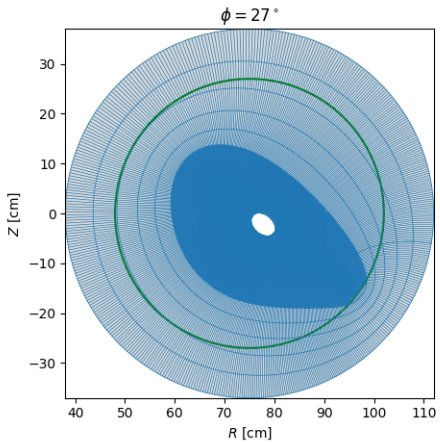

(b) $\phi = 27°$ grid cross section

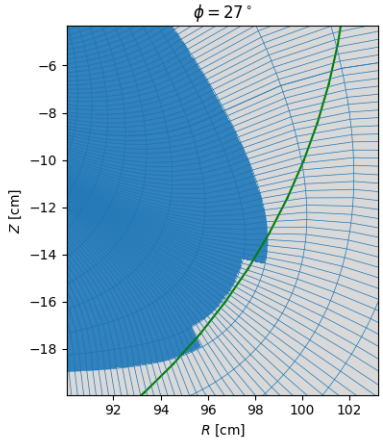

(c) $\phi = 27°$ magnified at wall intersection

Figure 2.14: Example magnetic mesh for one of the 6 magnetic configurations studied in CTH in chapter 3. The blue and white cells represent the plasma and neutral domain respectively. The green circle is the axisymmetric wall boundary.

The neutral mesh is generated next by extending the current mesh. The neutral cells

are geometrical and do not solve for any plasma conditions and thus do not have the same constraints as the plasma domain. To more accurately represent the experiment, the neutral domain must cover the entirety of the vacuum domain outside of the plasma cells. To extend the neutral grid cells in this configuration, we choose the neutral cells to mimic the vacuum vessel shape. Alternatively, the neutral cells can be chosen to be an expansion of the outer plasma boundary. The plasma and neutral domain meshes together are shown in figure 2.14 for (a) $\phi = 0°$ and (b) $\phi = 27°$ where all the grid cells are outlined in blue. The plasma cells filled in blue while the neutral ones are unfilled.

Finally, FLARE requires files of PFCs in order to generate plate boundaries. The plate boundary is the axisymmetric wall indicated in green in figure 2.14. In this process, FLARE will mark which cells belong to the neutral or plasma domain with respect to the plate(s). Figure 2.14 (c) shows the white neutral cells and blue plasma cells in the vicinity of the wall. In this example, cells which intersect the boundary are marked based on whether or not the majority of the cell lies within the plate boundary. The field lines and cells outside of the boundary will not be evaluated during the iteration process for EMC3-EIRENE.

A method for magnetic mesh grid making which utilizes an unstructured mesh with adaptive refinement for complex 3D configurations is described in reference [97].

Chapter 3

Exploring NRD features in the Simple Geometry of CTH

The focus of this chapter is the plasma edge structure of CTH for studying NRD features. The major findings have been published in [18].

The Compact Toroidal Hybrid (CTH) experiment is a stellarator tokamak hybrid located at Auburn University. It has configurational flexibility through variation of the currents in the magnetic field coils and the induced plasma current driven by its central solenoid. Thus, it is possible to change the rotational transform over a broad range and alter the edge behavior strongly. It is shown for the first time in CTH that a chaotic edge structure is formed from these configuration changes, and yet these intersection patterns on the wall elements are resilient to the edge structure evolution. The structural details of the chaotic magnetic boundary will be identified from the intersection patterns on several wall targets in section 3.2. It is shown that these details in the intersection pattern dictate the heat flux pattern and that the resulting heat flux is shifted within the overall resilient helical intersection pattern across these configuration changes. The implications of these findings for possible mechanical divertor designs are discussed.

In section 3.1, the CTH experiment is described and the set of configurations that will be used for the rest of the thesis is introduced. In section 3.2, the calculations of the

strike line evolution as the configuration changes are presented and they are compared to connection length analysis on the wall surfaces at different radii. In section 3.3, EMC3-EIRENE simulations for dedicated configurations are provided. In section 3.4, the results are discussed in terms of the impact of designing mechanical structures around the magnetic structure of the boundary in an NRD configuration. Finally, a summary is provided in section 3.4.

3.1 CTH Edge Structure

CTH, depicted in figure 3.1, is a 5-field period torsatron device that also features a central solenoid that can be used to inductively drive toroidal plasma current I_p [19]. The "hybrid" part of the name refers to the fact that CTH spans the space between a tokamak and a stellarator. The vacuum vessel is a circular torus with major radius $R_0 = 75\,\text{cm}$ and minor radius $a = 29\,\text{cm}$. A CAD rendering of the CTH layout is shown in figure 3.1 from [20]. In this figure, the helical coil that produces the 3D field is shown in red and the central solenoid is shown in brown. CTH includes many shaping coils, but in this thesis, the current in all coils is kept fixed, and the only difference between configurations is the amount of I_p driven in the plasma by the central solenoid. The set of coil currents for the configuration considered here is shown in Table 3.1.

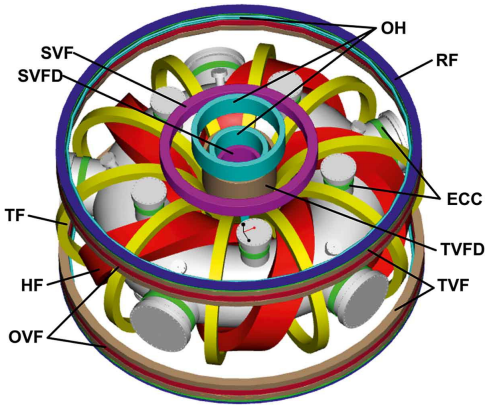

Figure 3.1: Vacuum vessel and magnetic coils of CTH [20].

Coil ID	# of Windings (Polarity)	Current (A)
HF*	4	3333
OVF*	-6	3333
TVF	-4	535
SVF	30	-200
TF	48	900

Table 3.1: CTH coilset ID, number of turns in the coil, and currents for high- ι operation. If an ID is not listed, it carries no current. *Connected in series.

3.1.1 Calculating the Magnetic Field Structure

The systematic exploration of the NRD at CTH is conducted by an analysis of the magnetic field structure in the plasma edge with various wall positions for six different levels of I_p, ranging from no inductive current to 10 kA. The centrally-peaked current density profile is proportional to $I_p' = dI_p/dS \propto \left(1 - S^3\right)^5$, where S is the normalized toroidal magnetic flux. This current profile is similar to the 2-power parameterization that is empirically motivated by CTH experimental data [98]. We assume a zero pressure profile across the different magnetic configurations. Using the methods described in section 2.3, we employ a VMEC simulation [80] in free-boundary mode to establish an MHD equilibrium solution for each of the six levels of I_p. The Ohmic current drive causes the rotational transform to vary as seen in figure 3.2.

CTH can be scanned over a range of rotational transforms, and in this thesis, the chosen I_p were expected to produce non-limited plasma wall configurations at the higher I_p values. In figure 3.2, the rotational transform ι as a function of major radius R is shown for six equidistant values of I_p. The rotational transform is calculated up to each magnetic configuration's respective LCFS. This means that there are open field lines beyond the largest R for each level of I_p in figure 3.2. The top plot is generated from field line following and calculating ι while the bottom plot is the profile generated from the VMEC solution. It is noted that each I_p has a different magnetic axis and for each I_p case the axis shifts roughly between $0.71\,\text{cm} < R < 0.79\,\text{cm}$, and this can be seen in figure 3.3. From these plots in figure 3.2, it's observed that the configurations feature a very low magnetic shear, with almost entirely flat rotational transform profiles and some variation

towards the plasma edge. We also observe a shift of the profile from around $0.3-0.35$ for no current drive, to $0.7-0.8$ at 10 kA as I_p is increased. The flat profiles and the different values of ι imply that the equilibrium as a whole, and in particular the plasma edge, is governed by very different rational surfaces for each value of I_p.

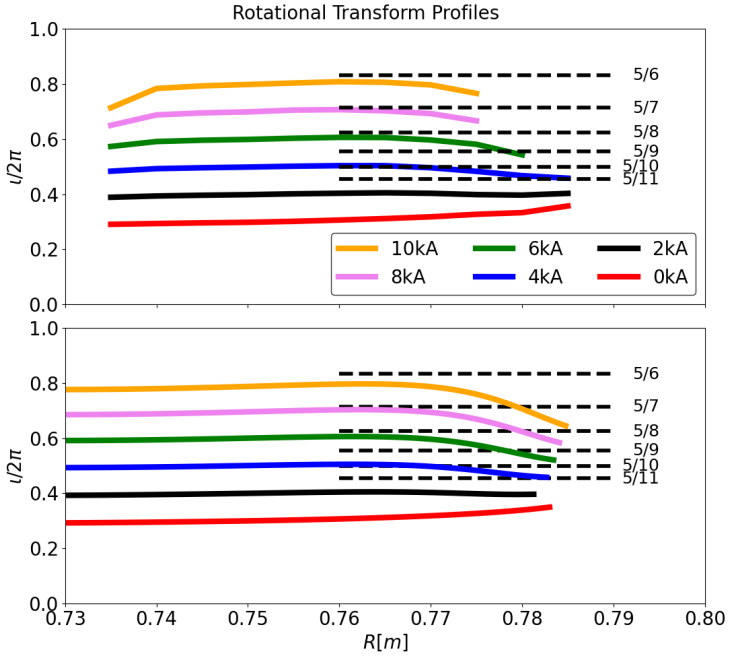

Figure 3.2: Rotational transform profiles ι for $I_p \in [0\,\text{kA}, 10\,\text{kA}]$ as a function of R. Top plot is calculated via field line following while the bottom plot is generated from the VMEC solution. Both plots share the same legend.

In each of the plots of figure 3.2, these possible rational surfaces are shown in dashed black lines for the rotational transforms values of $\iota = \frac{5}{6}$, $\frac{5}{7}$, $\frac{5}{8}$, $\frac{5}{9}$, $\frac{5}{10}$, and $\frac{5}{11}$. As I_p is increased, we see that each current case coincides with a particular ι value and eventually interacts with another separate set of rational surfaces. For example, in the case of $I_p = 4\,\text{kA}$, shown as a blue profile, this profile is governed by the $\iota = \frac{5}{10}$ island chain but eventually lowers to $\iota = \frac{5}{11}$ towards higher R at the edge. The impact of the magnetic structure is accordingly expected to be significant and, therefore, enables us to study how much the field line intersection patterns on wall elements are resilient to such changes in the equilibrium.

Section 2.3 describes the next steps to prepare the field line tracing routine to determine

the plasma contribution to the field outside of the LCFS. With this, the magnetic field structure can be calculated using the FLARE code also described in subsection 2.3.2. FLARE requires a geometric boundary representation, and for this, we use the circular vessel wall of CTH and do not consider any other physical sub-components of the vessel wall. The field line structure for the configurations can be seen, for the $\phi = 0°$ plane, in figure 3.3. In this figure, an overlay of the Poincaré map in black and the magnetic field line connection length L_C as color-coded contour map is shown. The six different plots are for an increasing level of inductive current, starting at 0 kA in the upper left corner in figure 3.3 A and increasing in 2 kA increments to 10 kA in the plot labeled F. The field line tracing calculation is performed for a maximum connection length L_C of 1 km in both the forward and backward toroidal direction along the field line. The white surfaces represent the confined plasma, that is, locations where $L_C > 1$ km in both directions. This is why the maximum combined L_C is 2 km on the color bar as it is the sum of both toroidal directions. The field line tracing calculation shown here is performed with respect to the boundary at 29 cm.

The Poincaré plots allow us to identify characteristic domains of the magnetic structure in the boundary. The inner plasma core is seen as long field lines (white color) forming intact magnetic flux surfaces. More radially outward of the core, the presence of magnetic island chains can be seen in all configurations. In the 0 kA case, the islands are well formed. However, as I_p is increased, the ι profile rises and lower-order poloidal harmonics define the island structure. Because they feature a larger radial width, adjacent island chains start to overlap and a chaotic region is formed. The structure of this chaotic edge is characterized by a mix of smaller and larger L_C flux channels formed by this interaction of magnetic islands from adjacent rational surfaces. The chaotic domain has areas of finite L_C which shows that this domain is connected to the wall on the maximum length scale of the field line tracing. Therefore, we call this yellow ($\mathcal{O}(10^3\text{m}) - \mathcal{O}(10^2\text{m})$) to red ($\mathcal{O}(10\,\text{m})$) colored domain in figure 3.3 an open chaotic layer. This description of the L_C structure is connected to the tangle features described in section 2.2. The dark red to black areas

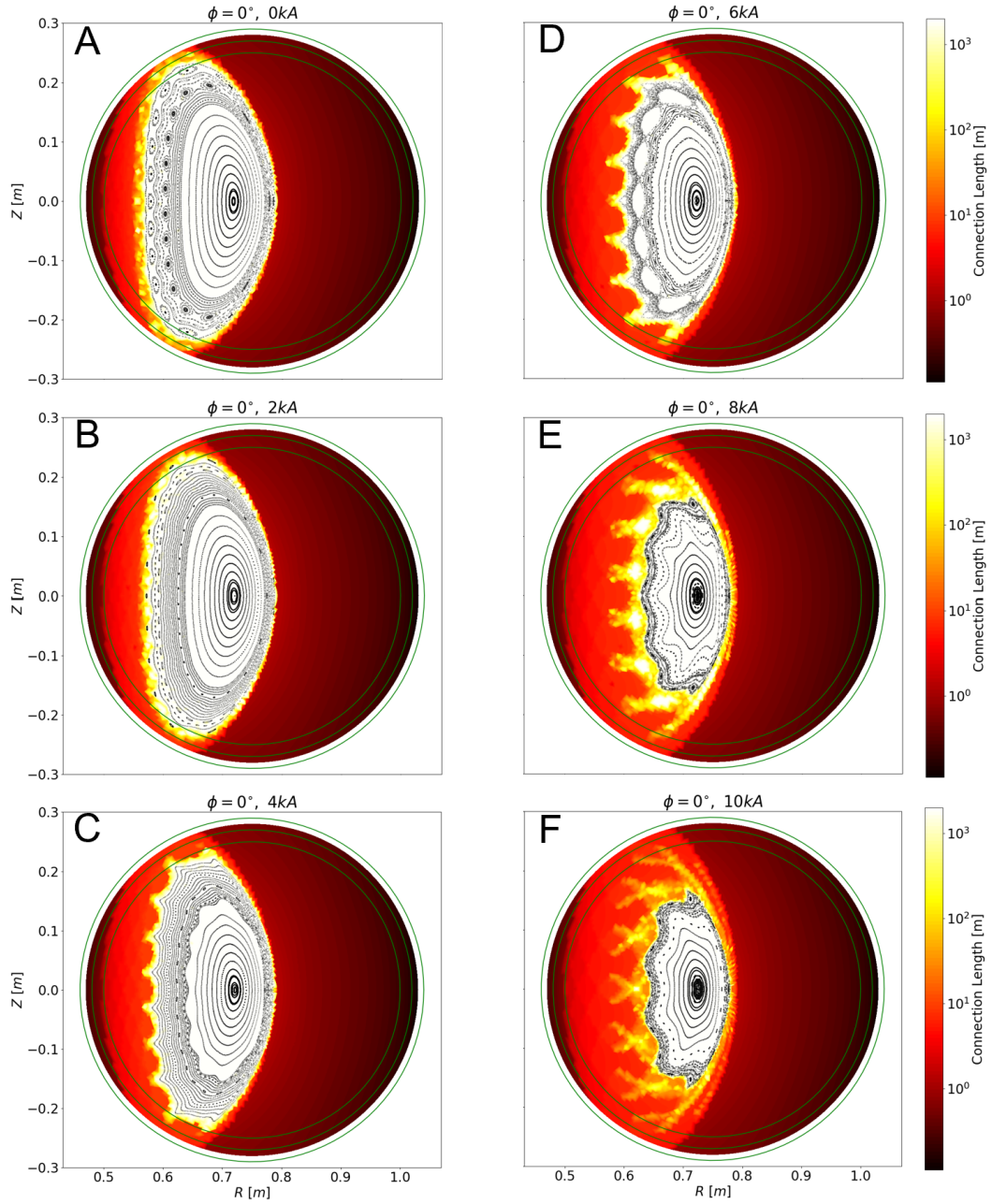

Figure 3.3: Logarithmic connection length (Lc) contour map for $I_p \in [0\,\text{kA}, 10\,\text{kA}]$ for $\phi = 0°$. A Poincaré map is superimposed as black points on all plots. Additionally, three circles are shown in green for $r = 25\,\text{cm}$, $r = 27\,\text{cm}$, and $r = 29\,\text{cm}$ to indicate the locations of the radial wall targets in the analysis performed in sections 3.2 and 3.3.

with very short connection lengths, $L_C < 1\,\mathrm{m}$ is the region far outside of the LCFS and represents the magnetic field that intersects the vessel wall after a short distance. The confined core region, seen as white colored field domain with intact magnetic flux surfaces, is observed to shrink significantly with increasing I_p and the rendering of the closed field lines becomes increasingly corrugated at the plasma edge. This is most visible in the right plots in figure 3.3 D−F with currents from $6\,\mathrm{kA} - 10\,\mathrm{kA}$. This corrugation inhibits calculation of the ι values for higher R as discussed for the left plot of figure 3.2. The corrugated features of the magnetic field lines are characterized by magnetic flux bundle structures of finite L_C that resemble the shape of lobes described in section 2.2. These lobes structures extend radially outward and tend to intersect one another at the highest values of I_p. A key question that presents itself looking at these strong structural changes with increasing I_p is how the significant changes in chaotic magnetic boundary structure couple to the intersection of this open chaotic layer with the wall surfaces.

3.2 Effect of Open Chaotic Layer on Plasma-Wall Behavior

3.2.1 Strike Line Analysis

The intersection pattern of the open chaotic boundary with the plasma facing component (PFC) is investigated in this section with strike line calculations. The PFC in this calculation is an axisymmetric circular wall. The strike points are calculated with FLARE by following a field line that is launched inside the plasma LCFS for a maximum L_C of 10 km in the forward and backward directions. Since field lines launched inside the LCFS are confined by good flux surfaces, we include a user-defined magnetic field line diffusion parameter, d. This is a numerical approach that allows for the field lines to enter the open chaotic edge layer, intersect the PFC, and map out a strike line pattern. For these calculations, we choose the value $d = 4.4 \times 10^{-7}\ \mathrm{m}^2/\mathrm{m}$ which is approximately what would be expected from a 15 eV electron that experiences a particle diffusion of $D = 1\,\mathrm{m}^2/\mathrm{s}$. This calculation, where field lines diffuse outward from the confined region into the open

chaotic system that eventually intersects the wall elements, is similar to work done on other stellarators [15], [99].

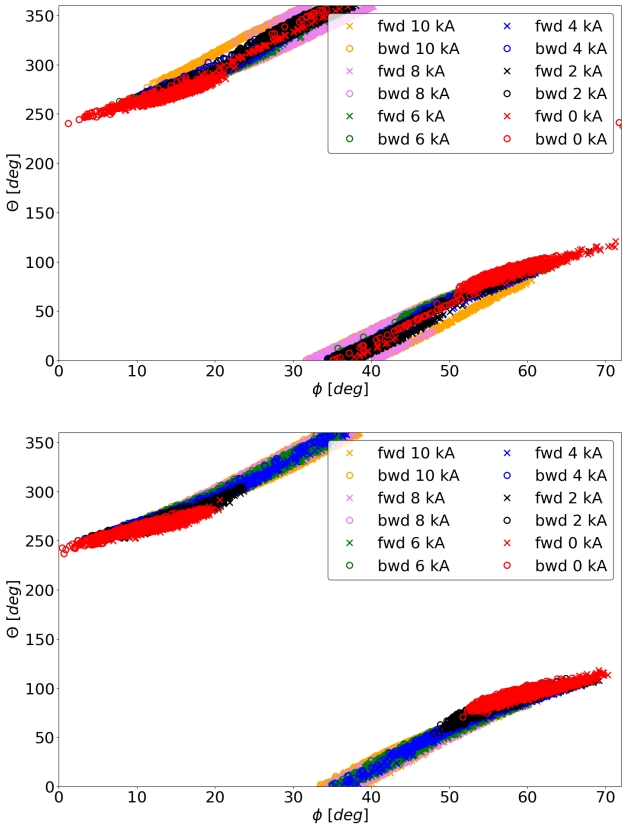

Figure 3.4: Forward and backward strike point locations along the CTH boundary at $r = 29\,\text{cm}$ (top) and $r = 25\,\text{cm}$ (bottom) for $d = 4.4 \times 10^{-7}\ \text{m}^2/\text{m}$ followed for a maximum L_C of 10 km plotted for a single field period.

An overview of these field line tracing results is shown in the top plot of figure 3.4. In this plot, the toroidal and poloidal angles of the intersection point of each traced field line with the PFC are recorded. Since CTH has 5-fold symmetry, only one field period is shown, spanning toroidal angle $\phi \in [0°, 72°]$. Because the wall has circular cross sections, the poloidal angle, θ is the usual cylindrical polar angle. This intersection pattern is shown in figure 3.4 for all toroidal currents considered, i.e. $0\,\text{kA} - 10\,\text{kA}$. The minor radius of the PFC is also altered to vary the aspect of the edge structure that intersects the PFC. Hence, the bottom plot of figure 3.4 shows the strike points corresponding to the minor radius of $r = 25\,\text{cm}$ and will be discussed further in section 3.2.2.

Figure 3.5 corresponds to the top plot of figure 3.4 and shows each toroidal current starting with the 0 kA current configuration in the upper plot of the left column (figure 3.5 A), with increasing I_p going downward, starting again in the right column to end at 10 kA in the lower right column (figure 3.5 F). The upper left section of strike points and the lower right region are exactly symmetric due to stellarator symmetry, with forward/backward directions inverted.

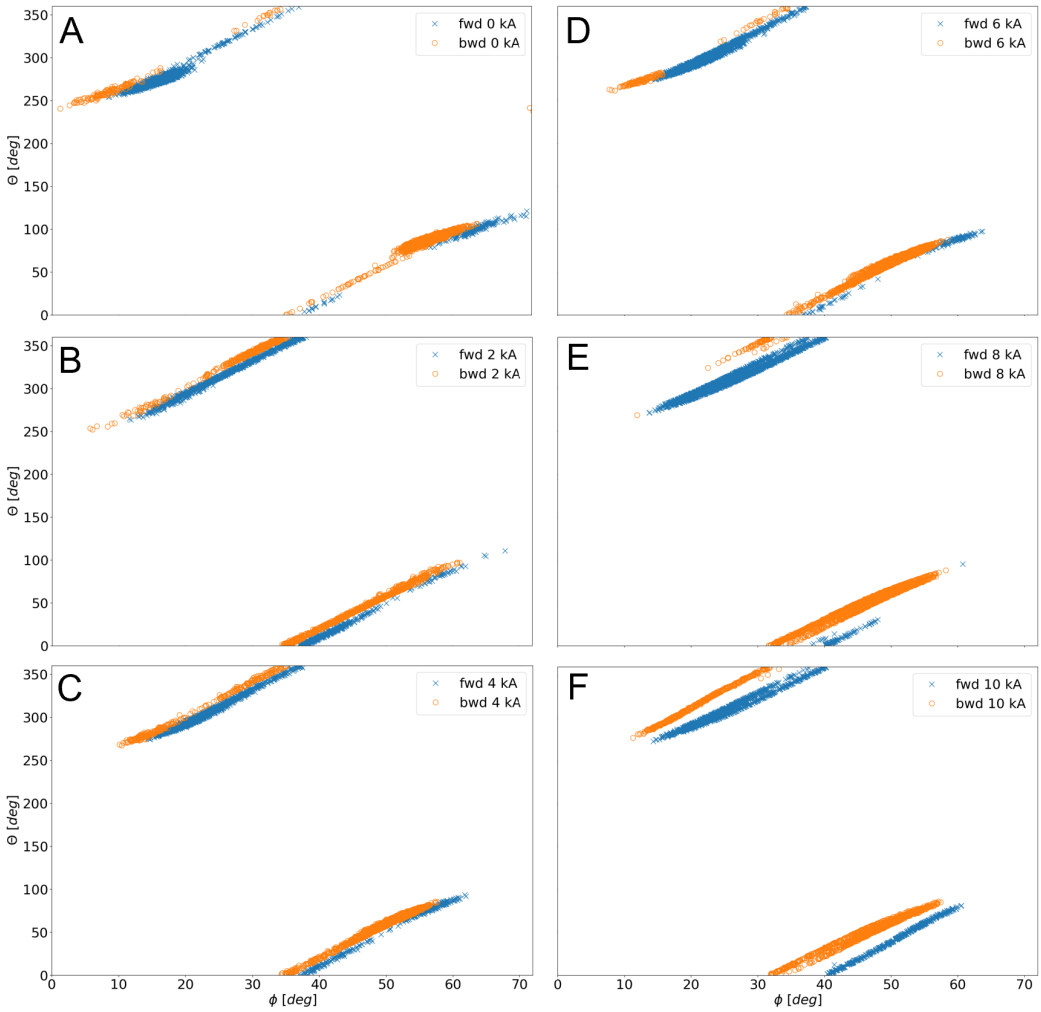

Figure 3.5: Forward and backward strike points for $r = 29$ cm plotted for all I_p cases for $d = 4.4 \times 10^{-7}$ m^2/m followed for a maximum L_C of 10 km plotted for a single field period.

This strike point calculation follows the field lines for a maximum of 10 km. Because of the randomness in the diffusive property, approximately 60% of the launched field lines

strike the wall in the 0 kA configuration. Meanwhile, 90% of the points intersect the wall in the higher current cases. The difference in the number of wall-intersecting points between the low and high current case can be understood by considering that lower I_p configurations have a larger confined volume. This allows for more particles to remain in the confined region. The top plot of figure 3.4 indicates that the general shape of the strike point pattern is resilient in terms of being a helical pattern with a narrow spread, ranging from just a few degrees poloidally for the 0 kA case to up to 20 degrees for $I_p = 10$ kA. This occurs despite the drastically changing magnetic structure of the open chaotic layer as shown in figure 3.3. However, detailed analysis of these initial strike line calculations show that the intersection pattern can move along the helical strike line and also perpendicular to it resulting in "splitting" of the strike line. This split feature is observed particularly for the highest current cases discussed next.

3.2.2 Varying Wall Position

In addition to changing the current, it is also possible to alter the wall position. We study the impact of a reducing PFC radius of the axisymmetric circular wall. Specifically, in addition to the vacuum vessel radii at $r = 29$ cm, we simulate the field line behavior for wall radii 27 cm and 25 cm. These inner radii were chosen to compare with the simulated heat flux deposition in section 3.3.

In the bottom plot of figure 3.4, the same calculation as the top plot of 3.4 is shown, but with the wall at 25 cm instead of 29 cm. In figure 3.3, the boundary at 25 cm is plotted as the innermost green circle. The boundary at 29 cm is just outside of the connection length contour map and is plotted in green. A similar characteristic strike line pattern with a dependency on the current levels is seen with a wall at 25 cm compared to 29 cm. The strike points remain in the same general area in toroidal and poloidal angles and the helical movement as well as the spread in the poloidal angle perpendicular to the helical pattern is comparable. However, there are some differences that result from the wall position. To explore the features of the strike lines in more detail, we compare the

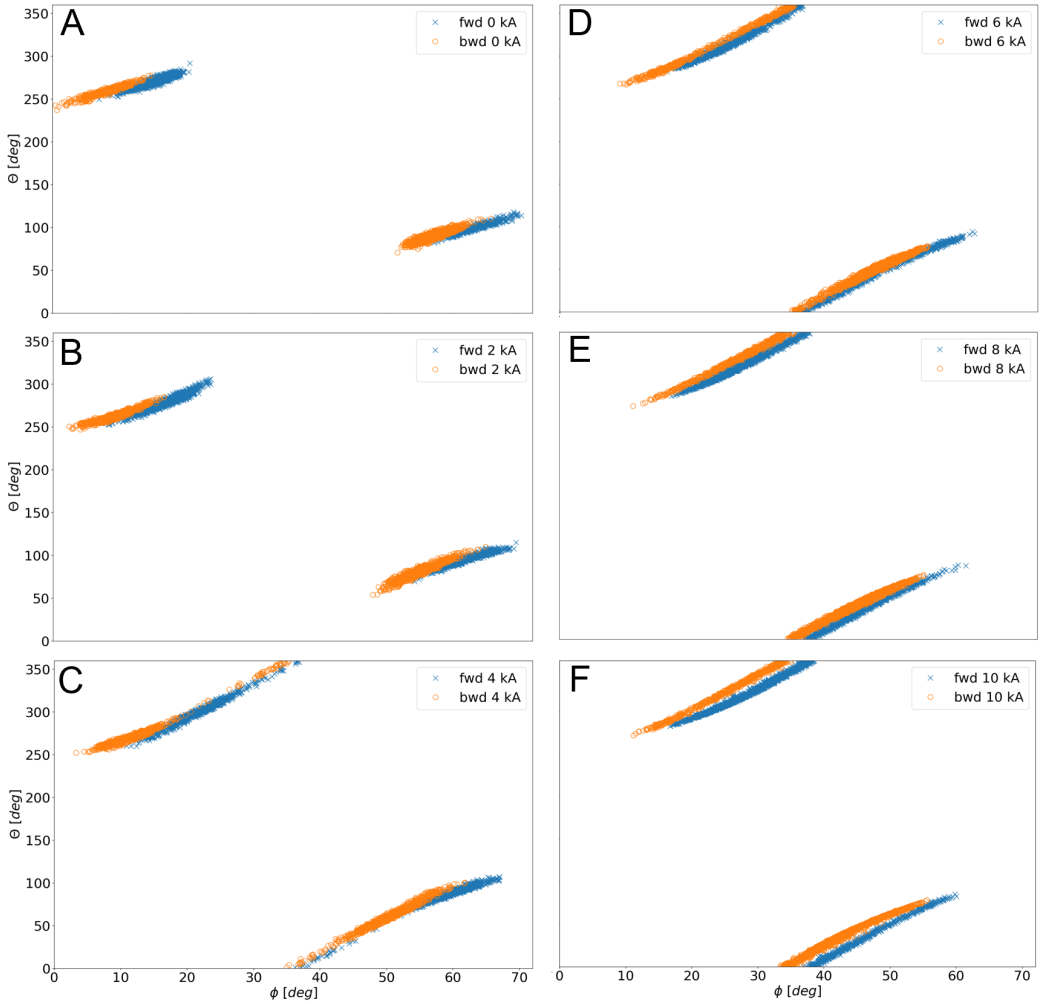

Figure 3.6: Forward and backward strike points for $r = 25\,\text{cm}$ plotted for all I_p cases for $d = 4.4 \times 10^{-7}\ \text{m}^2/\text{m}$ followed for a maximum L_C of 10 km plotted for a single field period.

individual results for each strike point location at both radii, shown in figures 3.5 and 3.6.

Starting with the low current configurations at the innermost wall position (figure 3.6), the strike points from lower I_p cases are split into two separate and distinct regions as seen in the 0 kA and 2 kA cases (figure 3.6 A and B). In the 0 kA case, one region exists from toroidal angle 0° to about 20°, with another region appearing from about 50° to 72°. As the current increases to 2 kA, the regions move towards the center of the field period, and at 4 kA (figure 3.6 C) the two regions are connected, and they remain that way for the rest of the higher I_p cases.

Another method to analyze the strike line pattern is the way field lines traced in the forward and backward toroidal directions intersect the wall in the strike line pattern. This is of interest because particles will follow these directions and their direction is indicative of the geometry and deposition pattern of later particle fluxes. Because these fluxes can yield a momentum exchange between adjacent flux tubes, understanding their geometry is particularly important for high-density and detachment scenarios. The interaction between counter-streaming particle flows is not explicitly analyzed here but has been shown to be an important influence in high-performing plasmas [45], [100]. In figure 3.6, these two directions are separated in color and marker (forward is plotted as blue $\times$ and backward as orange $\circ$). In the 0 kA case, the separation, or splitting, of the areas in which the forward and backward traced field line intersect the target extends approximately 20° in the poloidal direction. As the current increases, the separating line between the intersection areas from both tracing directions begins to extend more toroidally. Increasing the plasma current increases this separation further. The forward and backward strike point regions develop a helical line of separation, and at the highest current, 10 kA (figure 3.6 F), these two regions begin to separate entirely from each other.

The general helical strike line pattern across all I_p configurations at $r = 25$ cm span a similar region along the wall even when the wall is moved further out to $r = 29$ cm as seen in figure 3.5. However, at this radius, even at the 0 kA case (figure 3.5 A), an almost complete toroidal continuation between the two forward and two backward strike regions is visible, which was not seen in the 0 kA case in figure 3.6 A for $r = 25$ cm. At 2 kA (figure 3.5 B) these forward and backward regions are already completely toroidally connected. In addition, these regions are separated mostly by a helical line already in the 0 kA (figure 3.5 A) case similarly to the higher I_p cases on the innermost wall. At 8 kA (figure 3.5 E), the forward and backwards strike patterns are completely helically separated. It is important to note, that the separated strike point patterns at $I_p = 8$ kA and 10 kA are correlated with the appearance of lobe-like structural flux bundles in the open chaotic layer as plotted in figure 3.3.

3.2.3 Magnetic Footprint on Wall Targets

To better understand the structural behavior within the field line intersection pattern on the walls and how this structure influences the heat flux deposition in section 3.3, we examine the connection length $L_C(\theta, \phi)$ maps on the walls without diffusion similar to what has been done in references [72], [87], [101]. This is called the magnetic footprint and is shown as a contour plot of connection length $L_C(\theta, \phi)$ along the PFC shown in figures 3.7, 3.8, and 3.9 for the same six different plasma current values I_p which are labeled A-F in each of these figures. Unlike the strike point calculation, the field lines for this analysis were not started from the inside the LCFS and were not given a diffusion parameter. Instead, the field lines were started from a spatially high-resolution mesh of launch points constructed 1 mm inward of each respective wall boundary. As an example, the calculation mesh is at $r = 24.9\,\text{cm}$ for the cylindrical wall boundary at $r = 25\,\text{cm}$ which is plotted in figure 3.7. For all points on the calculation mesh, the field lines are followed, without diffusion, for 1 km in both directions, or until they hit the wall. These plots within figure 3.7 each show the first half field period for $215° < \theta < 360°$ in high resolution, which provides the details of the magnetic footprint structure. The magnetic footprints for the wall boundary of radius $r = 27\,\text{cm}$ in figure 3.8, and for $r = 29\,\text{cm}$ in figure 3.9 at multiple I_p are calculated and shown in the similar manner as figure 3.7. The intermediate wall is shown as the intermediate green circle plotted in each Poincaré map in figure 3.3. This wall is chosen because it is the furthest wall radius simulated with EMC3-EIRENE in section 3.3 and enables direct comparison between the simulated heat flux and field line following calculations. Simulation of magnetic footprints with a higher level of spatial resolution without diffusion enable the analysis of how the structural details within the intersection pattern influence the heat and particle flux deposition. The previous sections detailing the variation in strike line calculation across the various configurations give an approximate location of the anticipated heat and particle flux. This will be discussed further in sections 3.2.4 and 3.3.

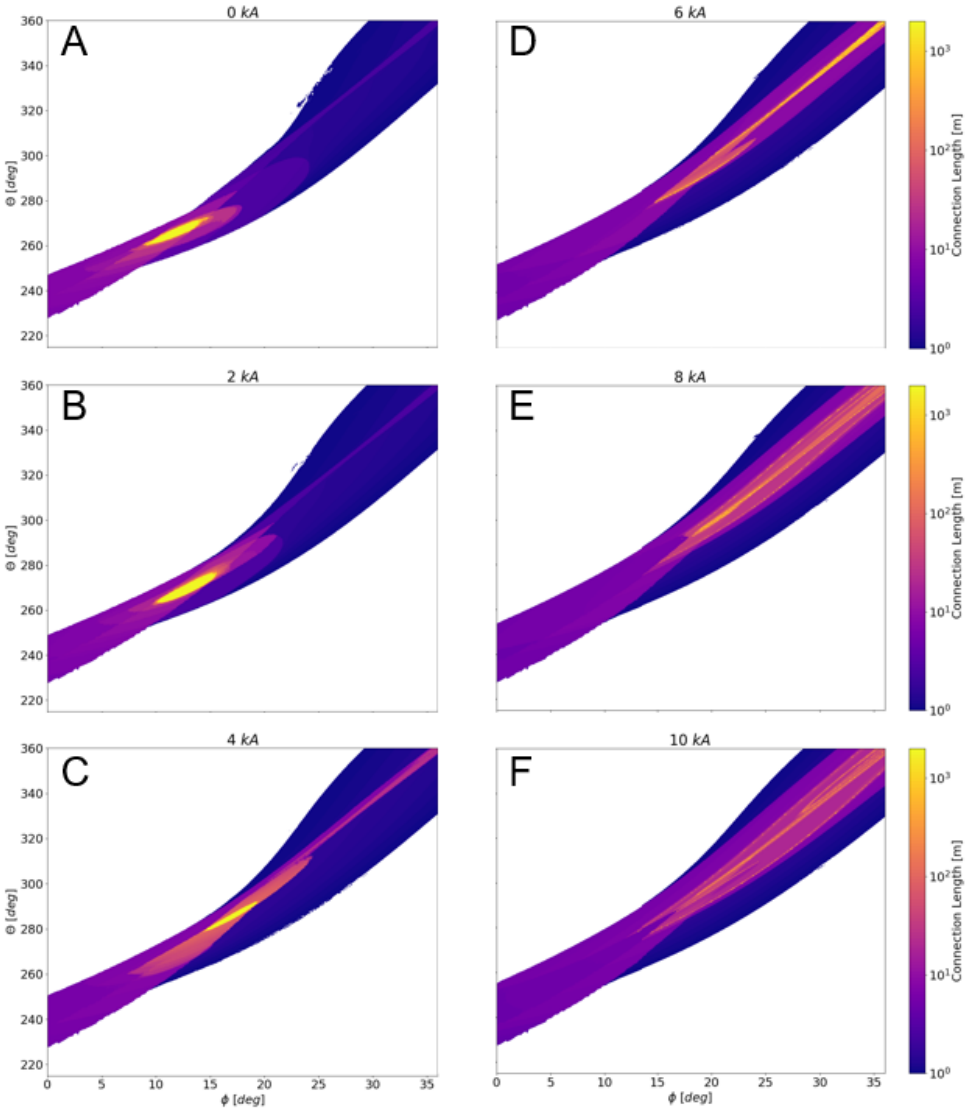

Figure 3.7: Connection length sampled on target at $r = 25\,\text{cm}$ for 6 different I_p.

In the lower I_p cases, there tends to be a localization of higher L_C with lengths greater than 1 km as seen in figure 3.7 as a yellow-colored cluster of field lines in the 0 kA, 2 kA, and 4 kA cases (figure 3.7 A, B, and C) with the innermost wall boundary at $r = 25\,\text{cm}$. In these plots, the yellow regions are predominately concentrated between $10° < \phi < 20°$. If $L_C = 2\,\text{km}$, it indicates that the field line launched in the calculation is connected to the core and may reach a good flux surface, seen as the white region in the figure 3.3. This can only happen if good flux surfaces exist within 1 mm of the wall. Therefore, the

presence of yellow regions of 2 km connection length, which we attributed before to the confined regions, suggests a limiter rather than a divertor configuration with the open chaotic system. Instead of lobe structures and short L_C connection length flux bundles that represent the SOL, good flux surfaces are in direct contact with the wall. There is still a small radial domain of an open chaotic layer, and we will analyze this with 3D plasma edge transport modeling later which will show its role for impacting the heat exhaust.

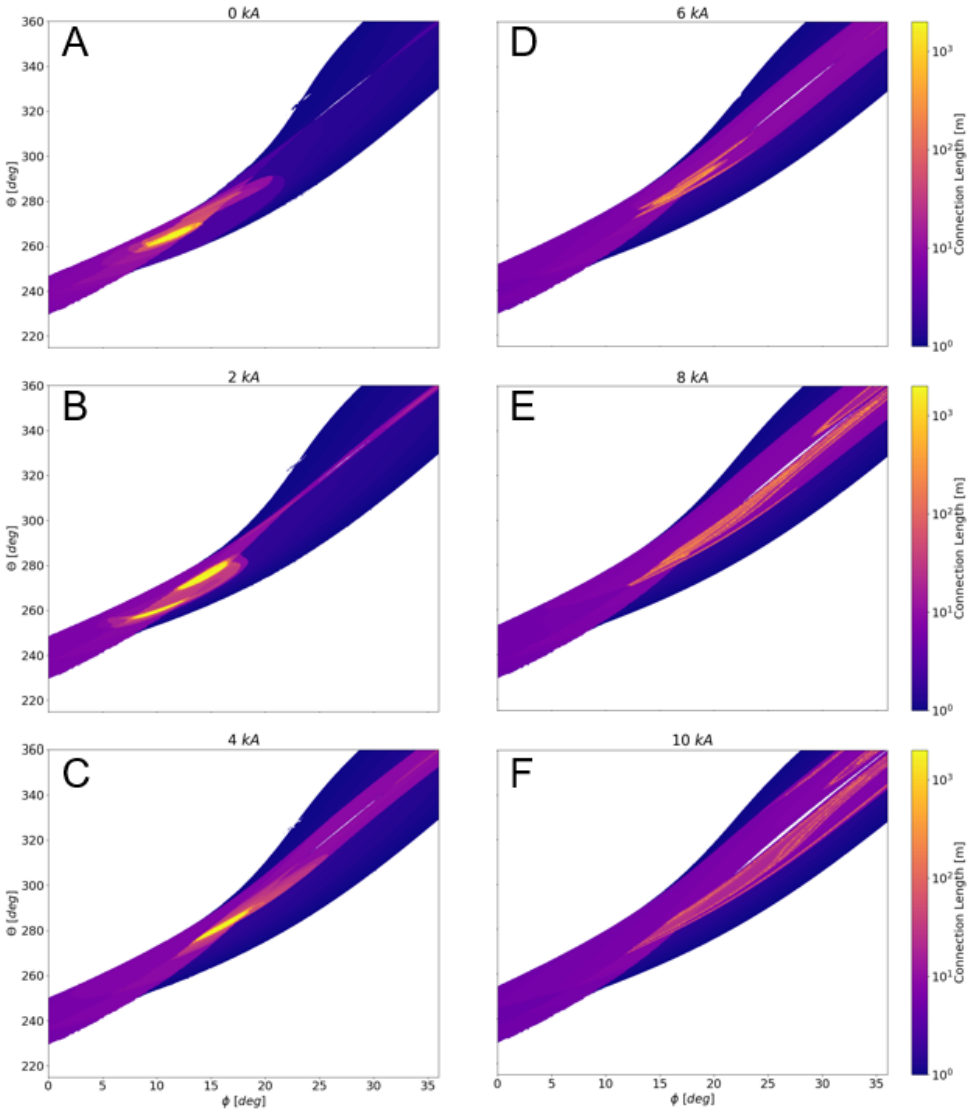

Figure 3.8: Connection length sampled on target at $r = 27$ cm for 6 different I_p.

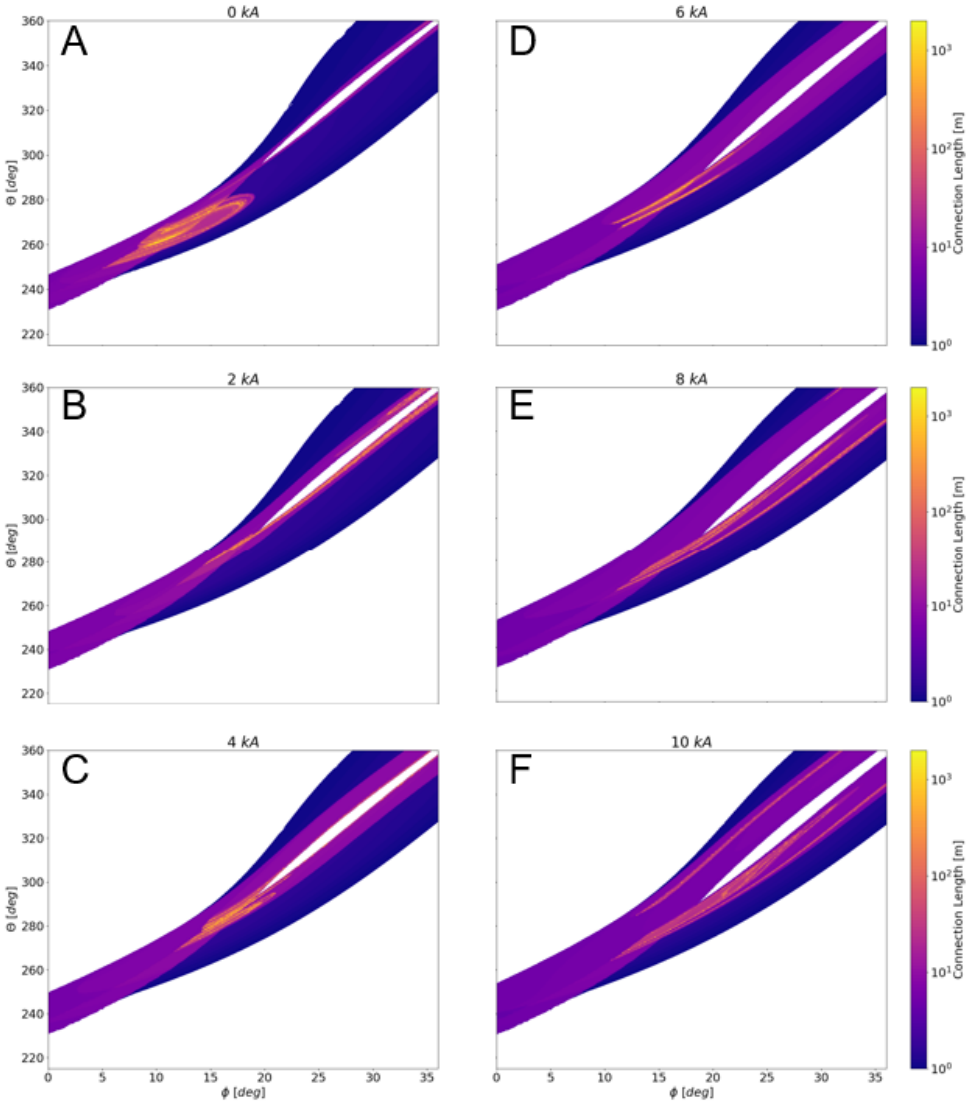

Figure 3.9: Connection length sampled on target at $r = 29\,\text{cm}$ for 6 different I_p.

When I_p is increased, we find similar trends in the magnetic footprints to the diffusive strike point calculations. The region of longest L_C migrates with increasing I_p to higher ϕ toroidally and towards the outboard mid-plane, which is defined at $\theta = 360°$, poloidally. Furthermore, the high-resolution magnetic footprint pattern exposes a higher level of complexity, corresponding to the complexity of the open chaotic boundary layer that intersects the wall. First, at $I_p > 6\,\text{kA}$, no regions exist of $L_C = 2\,\text{km}$ which supports the hypothesis that no good flux surface directly touch the walls. Therefore, these con-

figurations are not limited but rather are diverted. This is congruent with the fact that based on figure 3.3 we identified a larger radial domain covered by field lines with finite L_C and characteristic magnetic structures associated with the magnetic island chains and the invariant manifolds that form the skeleton of this divertor structure. It can be seen that the impact of increasing I_p is that the areas of highest L_C become less and less localized and eventually become diverted between roughly $20° < \phi < 36°$.

In the diverted region just mentioned, the appearance of these divertor strike lines becomes increasingly evident as the boundary is placed radially outward for this calculation. This is demonstrated in figures 3.8 and 3.9. The splitting between the divertor strike lines increases with increasing radius at these I_p values and even a private flux region can be identified which separates these divertor legs. The private flux regions appear as a narrow white region for $\phi > 20°$ and $\theta > 300°$. This feature is most present at higher I_p and even $I_p = 0\,\text{kA}$ case begins to display this feature at the 27 cm boundary between $25° < \phi < 30°$ and $320° < \theta < 340°$ in figure 3.8. In figure 3.9, all I_p cases have these divertor strike lines present.

3.2.4 Transition from Limited to Diverted Edge Behavior

By examining the variation in strike line behavior and magnetic footprint patterns across the magnetic configurations, we can conclude if the magnetic configuration may be limited or diverted. This is first examined by observing the separation of these strike lines seen in figure 3.5 where the different directions of the strike points are plotted in blue and orange. This separation is manifested similarly in the magnetic footprint calculations and can be correlated with PFC interaction with divertor legs. As I_p is increased, the higher yellow L_C regions migrate to these divertor strike lines in figures 3.7 - 3.9. These strike lines are the intersection point of the divertor legs with the wall as described before. The magnetic flux bundles corresponding to the finger-like structures in figure 3.3 are seen to be intercepted by the wall structures. This strongly supports a transition between a limited to diverted configuration based on the separation of these flux bundles depicted in

these figures, especially for regions for $\phi > 20°$ for the more radially outward walls.

The calculations of strike points using field line following and the connection lengths on the walls and in the plasma volume all point to a complicated evolving edge behavior in these CTH equilibria. We find clear evidence for a limited plasma wall scenario and a diverted one. The most clear indication of a limited situation is a region of infinite connection length slightly in front of the wall. These are indicated by the localized yellow regions on the connection length plots in figures 3.7 A-C and 3.8 A-C which correspond to the localized strike points in figure 3.6 A-C.

The diverted plasma configurations feature the appearance of a private flux region on the wall connection length, and a splitting of the strike line pattern in the forward and backward directions as seen in figures 3.5 A-F and 3.9 A-F. In these regions from approximately $20° < \phi < 36°$, the long L_C field lines stretch into long and thin bands of field lines surrounded by much shorter L_C field lines. This behavior is analogous to what is seen in classical divertors, where we find infinite L_C right at the separatrix intersection and rapidly decaying L_C values outward from the separatrix into the SOL. Therefore, we refer to these elongated long L_C regions that are seen for high I_p values as divertor strike lines. In these configurations, the heteroclinic tangles are playing the role that is played by the divertor legs in a classical tokamak.

In between the limited and clearly diverted configurations, the interpretation is more difficult. Regions of long connection lengths appear, but these do not form into coherent regions. These regions first appear consistently with a breaking of the edge flux surfaces, often resulting in what appear to be lobe-like structures as seen in figure 3.3. These fine structures, although visible in both the wall and volume connection length plots, tend to be smeared out by diffusive properties in both the calculations of strike points from diffusive field line following and fluid plasma simulations.

Figures 3.7, 3.8, and 3.9 along with the strike point figures 3.6 and 3.5 demonstrate the variation in behavior in the magnetic structure in the edge region. We have shown the presence of a chaotic edge and demonstrated that this edge structure evolves with varying

I_p. Furthermore, higher rotational transform ι, associated with higher I_p in figure 3.2, in turn increases the width of the chaotic layer in the edge region and the confined plasma shrinks, as seen in figure 3.3. These strike points and the magnetic footprint calculations can serve as a proxy for the expected heat and particle fluxes in these regions as it has been shown in previous work that the magnetic structure is correlated to these expected fluxes [68], [101].

3.3 Heat Flux Calculations

The analysis of the magnetic edge structure prompts questions about the transport within this open chaotic edge layer. This will be addressed using the EMC3-EIRENE 3D plasma edge fluid and kinetic neutral transport code. More on the code itself is described in subsection 2.3.3.

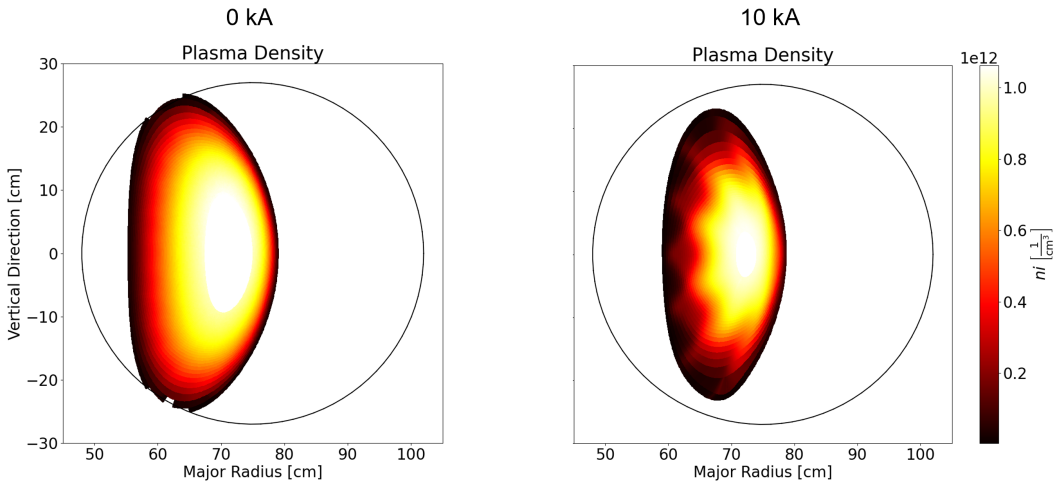

Figure 3.10: Plasma density n_i for 0 kA (left) and 10 kA (right) with wall target at $r = 27$ cm.

The input parameters for this analysis are as follows: The total input heating power is set to 5 kW along with an upstream density set to 3×10^{18} m^{-3}. The perpendicular transport parameters D, χ_i, and χ_e represent the cross-field particle diffusion, the thermal diffusivity for ions and the thermal diffusivity for electrons, respectively. These values are not known for CTH, so we choose characteristic values of $D = 1$ m^2/s and $\chi_i = \chi_e =$

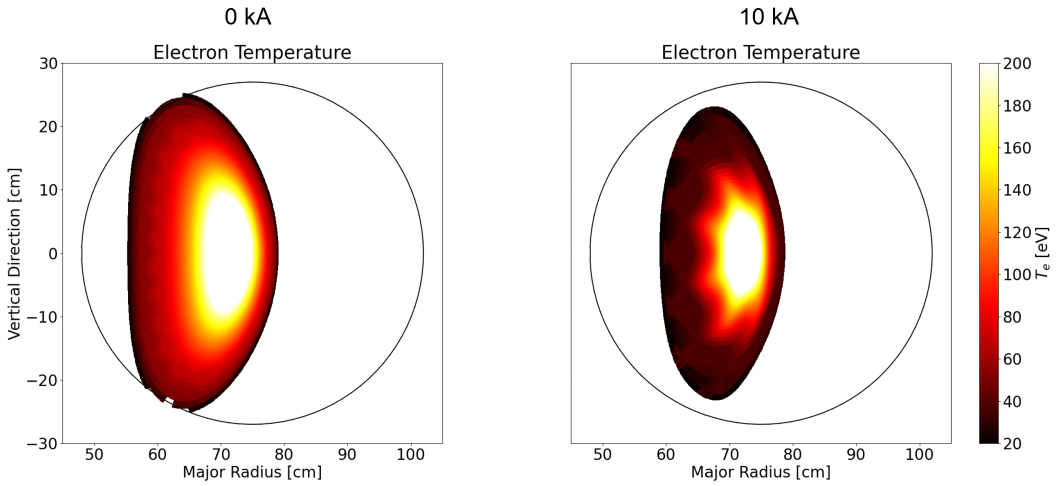

Figure 3.11: Electron temperature T_e for 0 kA (left) and 10 kA (right) with wall target at $r = 27$ cm.

3 m^2/s. No impurities are included in this modeling. In figures 3.10, 3.11, 3.12, the plasma density, electron temperature, and Mach number, respectively, are shown for the 0 kA and 10 kA I_p cases with the wall target at 27 cm plotted in black. This wall is the furthest wall radius simulated with EMC3-EIRENE due to grid generation issues. The plasma profiles reveal that the 0 kA case has a very moderately corrugated plasma edge. This can be seen as the slight alteration in the small magnetic islands which are visible in the electron temperature in 3.11 and the plasma flow approaches the intersection point predominantly from one side in 3.12. This result strongly supports that the plasma in the 0 kA case is in a limited configuration, because there is no significant radial distance between the target and the good flux surfaces which poloidally have quite homogeneous plasma parameters in close proximity to the intersection point. In contrast, the 10 kA case seen in figure 3.12 features a significant radial domain where distinct parallel flow channels exist which separate the intersection points on the target from the remaining confined plasma region. The same is also seen in the electron temperature in figure 3.11 where a radially extended cold region is seen and is also observed in the electron density in figure 3.10 where this region features much reduced density values. Last but not least, the Mach number shows the evolution of independent flux tubes which feature flows of opposite sign. This clearly supports the existence of independent convective transport channels that carry the plasma

flow through this radial domain. These results, therefore, strongly support that the low current configuration is limited, meanwhile, the higher current case of 10 kA is diverted.

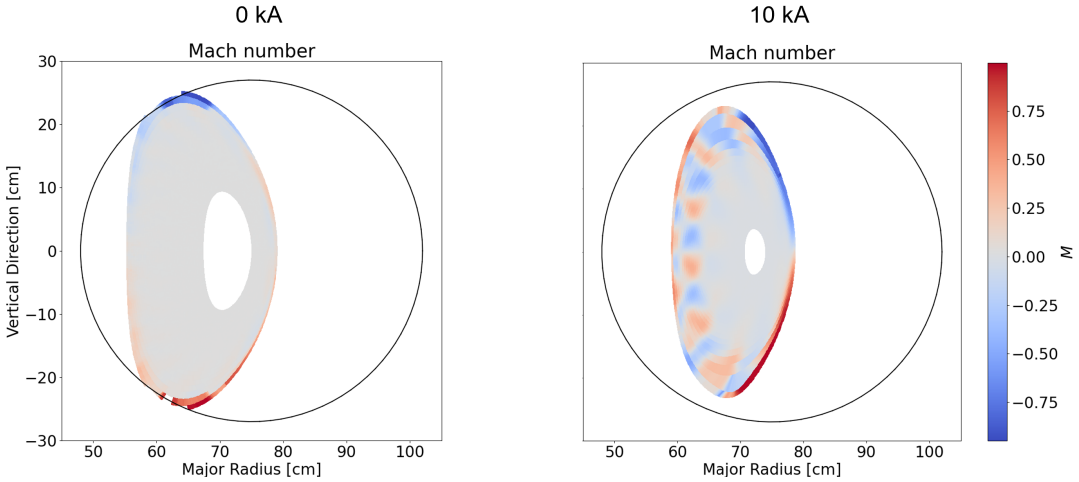

Figure 3.12: Mach number M for 0 kA (left) and 10 kA (right) with wall target at $r = 27$ cm.

After this analysis of the volumetric plasma characteristics in these perturbed edges, the target heat flux is analyzed using post-processing routines in EMC3-EIRENE for the 0 kA, 4 kA, and 10 kA current configurations on the two wall positions at $r = 25$ cm and $r = 27$ cm for each I_p. An example description of mesh generation for the 10 kA case with wall radii $r = 27$ cm is provided in section 2.3.4. Due to the difficulty in grid generation for highly chaotic and corrugated plasma configurations, only 3 out of the 6 I_p cases are simulated with EMC3-EIRENE - the lowest (0 kA), maximum (10 kA), and intermediate case (4 kA). This also limits the simulated wall radii, particularly for the 10 kA case because it has the smallest plasma volume out of all the magnetic configurations and, as mentioned in section 2.3.4, the outer plasma boundary must intercept the PFC. The results for 0 kA, 4 kA, and 10 kA are depicted in figures 3.13 and 3.14. In each figure, the heat flux Q_t on the wall calculated by EMC3-EIRENE on the left, and an overlay of the strike points for that current case from the field line diffusion calculation using FLARE on the right is shown. The forward direction of the field line is shown in green $\times$ and the backward direction in blue $\circ$, such that the points are more visible on the overlay plot.

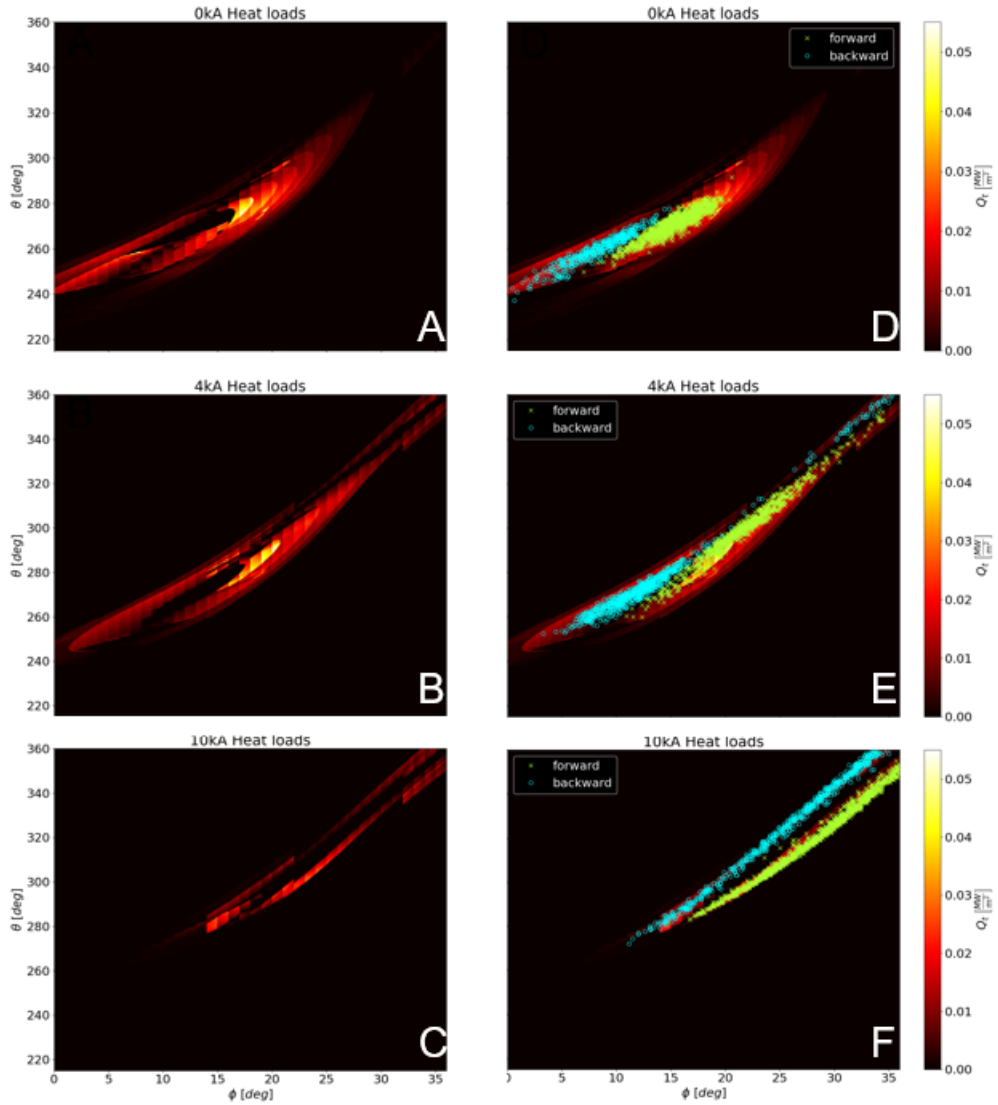

Figure 3.13: The left column shows EMC3-EIRENE generated heat flux deposition for a single half period on a high resolution wall target at $r = 25\,\text{cm}$ for $0\,\text{kA}$ (top row), $4\,\text{kA}$ (middle row), and $10\,\text{kA}$ (bottom row). The right column shows the same plot as the left but with FLARE strike points superimposed for the same target and with diffusion value $d = 4.4\ \times 10^{-7}\text{m}^2/\text{m}$.

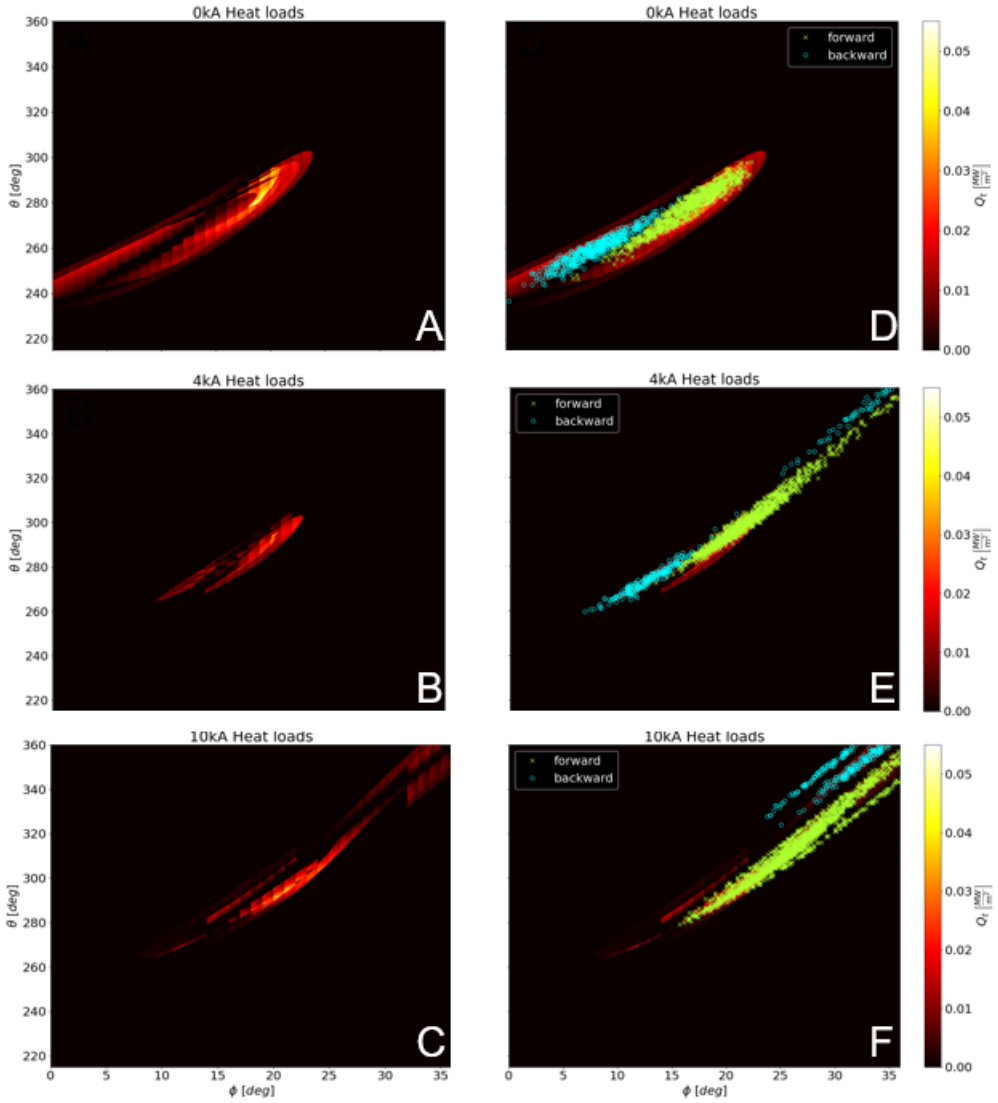

Figure 3.14: The left column shows EMC3-EIRENE generated heat flux deposition for a single half period on a high resolution wall target at $r = 27\,\text{cm}$ for $0\,\text{kA}$ (top row), $4\,\text{kA}$ (middle row), and $10\,\text{kA}$ (bottom row). The right column shows the same plot as the left but with FLARE strike points superimposed for the same target and with diffusion value $d = 4.4 \times 10^{-7}\ \text{m}^2/\text{m}$.

The EMC3-EIRENE results capture all the basic features of our previous calculations, with the exception of the $4\,\text{kA}$ case where the wall is at $r = 27\,\text{cm}$ (figure 3.14 B), which will be discussed later. In particular, the EMC3-EIRENE heat flux calculations indicate that the migration of the heat flux pattern in the low current, i.e. $0\,\text{kA}$, configurations does not extend to $\phi = 36°$. Meanwhile, the heat flux deposition at high current, i.e.

10 kA, configurations is absent between roughly 0° and 10° in the toroidal direction and tend to extend toward $\phi = 36°$. In addition, the forward and backward strike points can be seen to correspond to the two major separated areas of localized heat flux for all the cases considered. In between the forward and reversed heat flux areas, the separated region of no flux eventually changes and becomes a toroidally elongated narrow band. This is most visible in the 10 kA simulation (figure 3.13 C and figure 3.14 C). In short, EMC3-EIRENE verifies the major conclusions of the previous sections including capturing the transition from a limited configuration (figures 3.13 A and D and figures 3.14 A and D) to an intermediate configuration (figures 3.13 B and E and figures 3.14 B and E) and finally to a diverted configuration (figures 3.13 C and F and figures 3.14 C and F).

Looking deeper into the heat flux calculations and the magnetic footprint results, these figures show substructures which indicate a behavior correlated with homoclinic tangles mentioned in section 3.1. Figure 3.15 displays the different wall boundaries (A is $r = 25$ cm, B is $r = 27$ cm, and C is $r = 29$ cm) for the 0 kA case and a magnification of the region $240° \leq \theta \leq 300°$ and $5° \leq \phi \leq 25°$ for each magnetic footprint calculation in plots D, E, and F of figure 3.15, respectively. By placing these alongside each other, the evolution of the substructures can be seen as the wall target configuration changes from one that is limited to one that is more diverted for a single current case. In the EMC3-EIRENE results, the two peaked heat flux regions in the current cases of 0 kA and 4 kA are comprised of substructures which appear to be boomerang-shaped lobes associated with the open chaotic layer. Plots A and B of figure 3.13 are magnified in figure 3.16 A and B for the results on the wall located at $r = 25$ cm for 0 kA and 4 kA, respectively. Plots C and D of figure 3.16 similarly magnify plots A and B of figure 3.7 where a similarly shaped boomerang-lobe structure is seen in the magnetic footprint maps in the areas with a concentration of long L_C. These substructures have been previously connected to different parts of stable and unstable manifolds, and they impact the heat load deposition on the targets [68]. It was observed in TEXTOR [68] that there is a dependence on the field line direction which determines which manifold, stable or unstable, will receive flux.

Because none of our calculations have a dependence on overall field direction, there is no expectation to see the same behavior, however, these could be observed in a dedicated experiment. Moreover, these boomerang-shaped lobes in the connection length figures tend to migrate and become helically elongated into stripes as I_p increases as described in section 3.2. The formation and migration of the helical stripes of long L_C are governed by fractal patterns which are seen to impact that heat deposition [101]. The details of these patterns are not resolved in the strike point behavior due to the diffusion as mentioned above.

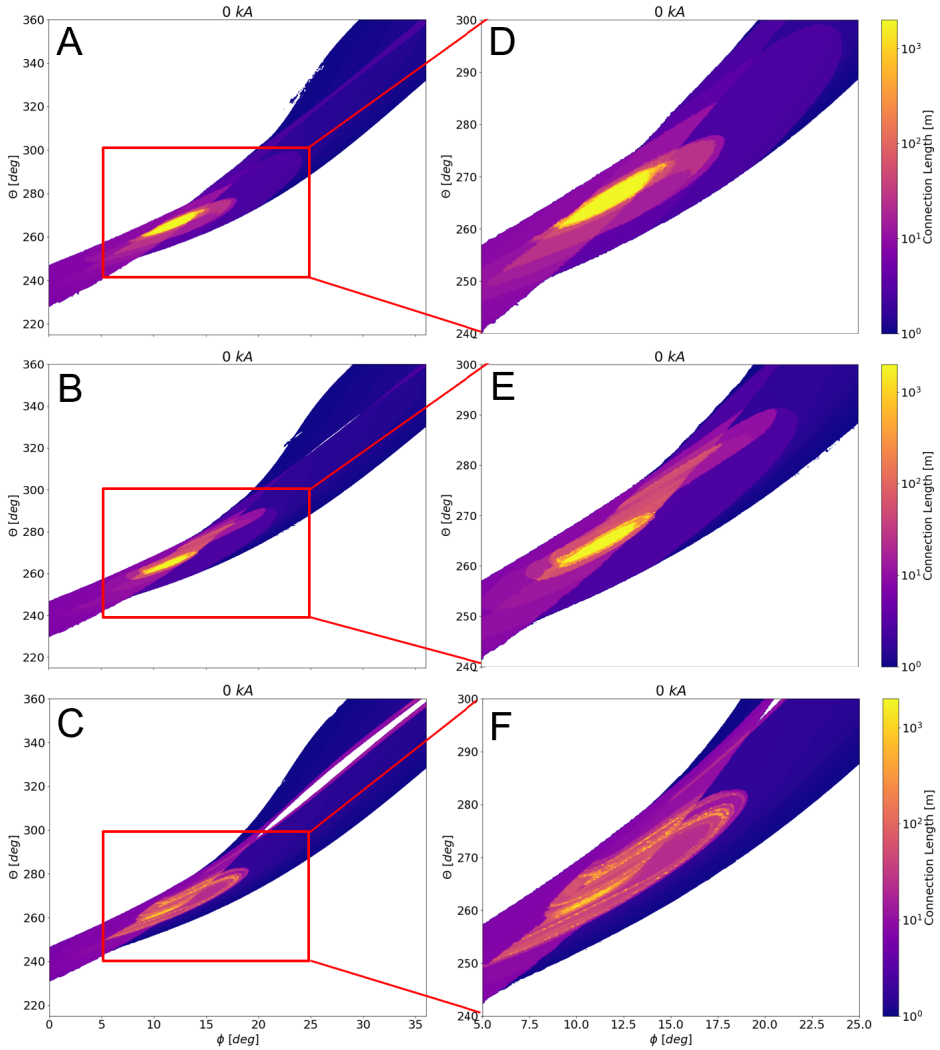

Figure 3.15: Magnified magnetic footprint maps of figures 3.7 A (shown in top row A and D), 3.8 A (shown in middle row B and E), and 3.9 A (shown in bottom row C and F).

Turning attention to the 4 kA result with a wall at $r = 27$ cm (figure 3.14 B). In this calculation, we see the largest discrepancy between the EMC3-EIRENE heat flux calculation, which shows a very limited region of plasma wall interaction, and the strike line calculation, which shows a more elongated structure. This is in contrast to the 0 kA result where EMC3-EIRENE shows a larger interaction region than the strike lines. There are also differences in the 10 kA result where there are some areas where EMC3-EIRENE calculates some heat flux, but no strike lines intersect, and some areas, such as the topmost blue strike line, where EMC3-EIRENE does not predict a corresponding heat flux. These details highlight the issues associated with using simple analyses, such as the strike point calculation, instead of more advanced edge codes. For example, field line following tends to under predict the heat flux location distributions in target shadowed regions, whereas codes like EMC3-EIRENE capture bidirectional heat transport in the shadowed flux tubes [102].

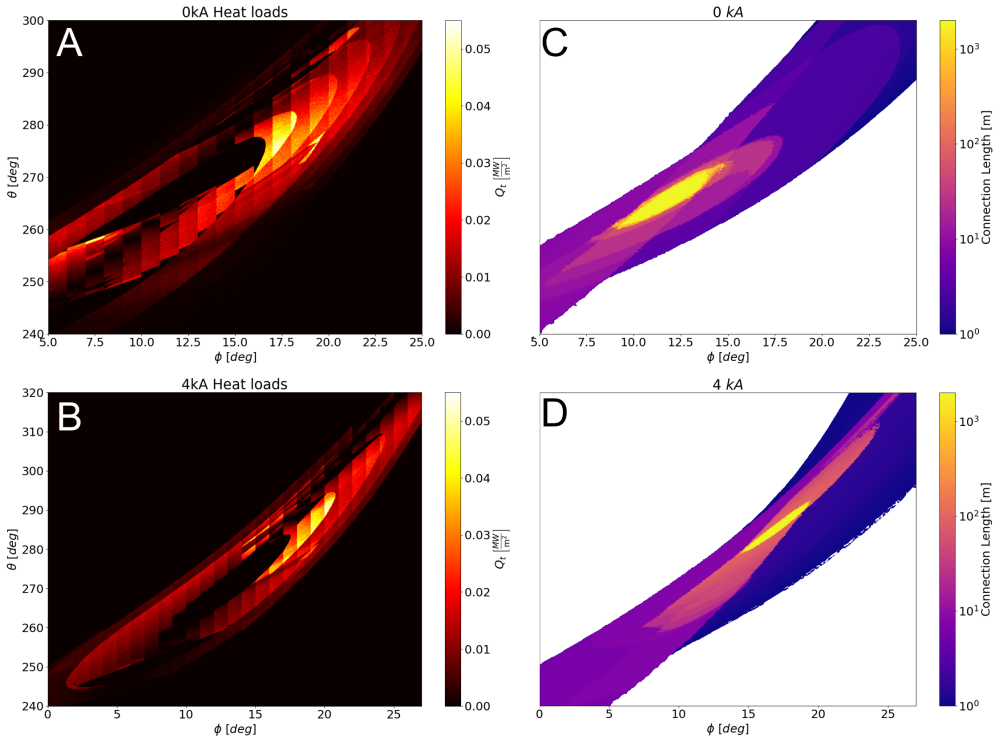

Figure 3.16: Plot A is a magnification of figure 3.13 A, plot B of figure 3.13 B, plot C of figure 3.7 A, and plot D of figure 3.7 B.

Another note of discrepancy is the different values of diffusion used in the field line following versus the EMC3-EIRENE results. As described in section 3.2, the value used for the diffusion is one of effectively distance corresponding to $d = 4.4 \times 10^{-7}$ m^2/m based on a 15 eV electron diffusing at 1 m^2/s. Meanwhile, the EMC3 simulations used characteristic diffusion of $D = 1$ m^2/s and $\chi_i = \chi_e = 3$ m^2/s and, as we can see in figure 3.11, there is a range of values in the edge for T_e. Therefore, these values inherently do not coincide with one another.

In spite of the noted differences comparing these analyses, the basic features that indicate an evolution of the strike points from a limited to diverted regime exist in both the EMC3 and strike point calculations.

3.4 Summary of Edge Analysis within CTH

The results shown here add important fundamental features to the concept of NRDs. We show that an open chaotic edge layer emerges during the toroidal current scan in CTH that is accompanied with the change from a limited to a diverted configuration through the formation of an open chaotic layer comprised of overlapping resonances outside the LCFS. The strike line pattern stays within a general helical pattern. Yet, differences are seen within the strike line structure. These features can be linked back to the well-established formalism of homoclinic and heteroclinic tangles used for the analysis of ergodic divertors. The tangles play the role of divertor legs where their intersections with the wall create the divertor strike line patterns.

The CTH analysis supports a transition from a limited to diverted edge regime. The expected heat flux deposition calculated with EMC3-EIRENE confirms the general features seen from field line following and that these strike points can serve as a proxy for overall expected heat flux distribution on the wall targets. In particular, it is seen that the open chaotic edge for diverted cases features independent parallel flow channels that separate the target PFC from the core plasma. The existence of these flow channels within the chaotic magnetic structure is connected to momentum transport in the plasma edge region

which is important for accessing high-recycling and detachment SOL regimes [45], [100], [103]. This will be discussed further in chapter 5 where the plasma transport behavior will be modeled in HSX to assess the viability of detachment.

Concerning the concept of "resiliency" in NRDs, first, there is a general resiliency of the overall intersection envelope of field lines on the wall. There exists a helical envelope that contains the strike lines for all configurations. However, the detailed intersection of the open chaotic structure that was identified within this helical pattern changes with toroidal current. For limited cases the intersection is localized while for higher current cases, that were classified as diverted, the strike line stretches out along the target, but stays within the overall helical envelope. This suggests that divertor target plates can be designed with respect to the helical intersection envelope. Experimentally, ongoing work at CTH has shown qualitative agreement between the modeled strike line location and measurements of plasma equilibria with similar features modeled in this thesis [104].

The variation in complex CTH equilibria served as a test-bed to study resilient NRD features within a simple geometry since CTH has a circular vacuum vessel. Along with the circular wall boundary, CTH generates its equilibrium from straight toroidal coils, a single helical coil, and current which is driven in the plasma. This geometry and design are in contrast with what is currently being pursued for stellarator reactor designs which make use of non-planar modular coils [105]–[107]. These designs are also optimized for neoclassical transport whereas CTH is not. In the next chapter, we will use the same tools to study a quasihelically symmetric example of the Helically Symmetric eXperiment (HSX). HSX features modular coils and has a complex stellarator geometry unlike the simple circular vacuum vessel geometry of CTH. Using a similar workflow described in this chapter, we will examine multiple magnetic configurations and describe the differences which arise across the resilient strike line. It is a key question to examine how different magnetic geometry and topology in HSX influences understanding of NRDs and resilient behavior as a QHS device compared to what was observed in CTH.

Chapter 4

Investigating Resilient Stellarator Divertor Features in HSX as a QHS Configuration

The focus of this chapter is the plasma edge structure of HSX for studying NRD features and divertor resiliency. The major findings have been published in [16]. The style and formatting of this chapter's text was adjusted from the publication for the flow of this document.

The previous chapter emphasized the differences observed when the plasma configuration is altered from a limited to a diverted edge regime by the formation of an open chaotic layer. This distinction was made based on associating features within the observed helical strike line pattern with magnetic structures such as tangles which function as divertor legs for diverted plasma wall scenarios. Like the last chapter, this chapter considers the differences observed within the simulated resilient strike line but for a complex shaped stellarator device that is optimized with respect to neoclassical transport. Additionally, none of the studied magnetic equilibria in this chapter are limited plasma configurations. Rather, this chapter distinguishes between NRD-like versus 'island divertor-like' configurations. This is done, in part, by examining differences manifested from varying island

size and location. To quantitatively discern the differences in open field line interaction with the wall due to islands, cantori, or turnstiles, we introduce a new metric and use its deviation from an empirical scaling law. The analysis of the edge magnetic field structure and the interaction between open field lines and the PFC in this chapter lays the groundwork for investigating the plasma transport behavior with EMC3-EIRENE in chapter 5. study of the magnetic field struture is hence a preparation to investigate plasma transport and divertor behavior at higher density with EMC3-EIRENE in chapter 5. This is of particular interest because our work in this chapter identified two configurations that are very different in terms of their magnetic structure.

This work expands on previous NRD research specifically for HSX as done in [15] by using the field line tracer FLARE [83]. To explore the chaotic structures present in the HSX plasma edge, a lofted wall [24] is used for simulations rather than the current physical vessel wall of HSX. This lofted wall is the largest extent the current vessel wall can be expanded such that the wall remains within the physical coils. The advantage of using an expanded wall further away from the plasma core is that this increases the width of the plasma edge region where various features in the magnetic structure, such as islands and collimated flux tubes, exist. This increased physical space also allows for future design and implementation of a mechanical divertor structure. How such a divertor is constructed depends on the specific features of the edge magnetic structure and its transport. We study these features in this chapter. The work presented in this thesis adds to the fundamental understanding of how chaotic structures arising in plasma edge influence the details of the NRD characteristic resilient deposition pattern. These details additionally influence how a divertor unit could be built for a future fusion pilot plant.

HSX is the first and only stellarator experiment optimized for quasi-helical symmetry (QHS) [23] shown in figure 4.1. Investigating NRD properties in a QHS device is important for designing resilient divertors for future reactor-scale quasi-symmetric stellarators [5], [108] in order to optimize a divertor solution that is compatible with an optimized core plasma solution. Specifically, quasi-symmetric configurations that scale towards a future

pilot plant will have self-generated bootstrap currents [6], [7] which necessitate the drive for a resilient divertor that remains unchanged with respect equilibrium effects. Even in quasi-isodynamic (QI) magnetic configurations with relatively low bootstrap compared to quasiaxisymmetric (QAS) and QHS stellarators, a functional NRD may be able to reduce the requirements on the plasma edge, expanding the acceptable configuration space. The NRD has been shown to exhibit resilient properties with respect to equilibrium and pressure changes in particular for HSX [15]. Hence, this work aims to expand on this previous research with the addition of the aforementioned lofted wall to enable further study of the field line-wall interaction for NRDs. We apply the new knowledge gained about chaotic structures, tangles and turnstiles, to more exactly identify the underlying plasma edge structures and their resulting transport that make a stellarator divertor "resilient".

The layout of the chapter is as follows. Section 4.1 describes the varying chaotic edge topology in four magnetic configurations. Special attention is dedicated to the resulting chaotic edge field line behavior in the vicinity of the lofted wall as we explore the characteristic resilient strike line pattern of NRDs in HSX. A new metric, the radial connection $\min(\delta_N)$, is introduced to aid in this analysis. Section 4.2 then uses $\min(\delta_N)$ to suggest the field line behavior that can be attributed to the presence of magnetic islands and to differentiate it from the other chaotic edge structures that were identified in the previous studies. We will discuss how both structural features influence the field line-wall intersection pattern across the different plasma equilibria. Finally, in section 4.3 we discuss the impact of the different magnetic edge structures on the field line-wall intersection pattern for understanding NRDs and summarize this work.

4.1 HSX Edge Structure

In this section, we will look at two methods for characterizing the magnetic structure and plasma transport in the boundary region of HSX with the lofted wall. We first introduce the four different plasma equilibria in this study followed by tracing the field lines in the vicinity of the wall to examine the interaction of the magnetic edge structure with the

wall. This analysis builds off of the insight from the previous chapter where we study beyond the strike line pattern. Solely examining the strike point calculations, as was done in [15], can appear to show identical behavior across several configurations. This approach can miss the underlying magnetic structure that gives rise to the strike line pattern. The metrics calculated in this section will show differences in the field line-wall intersection pattern in section 4.2 which will be connected to different plasma edge structures. This expands on what was initially done in reference [15].

4.1.1 Chaotic Layer Variation Across 4 Magnetic Equilibria

To analyze the magnetic structure of the plasma boundary in HSX across various magnetic equilibria, we perform field line tracing with the FLARE code [83]. FLARE requires a magnetic model and a defined boundary. For the magnetic model, we use a vacuum field grid approximated via a Biot-Savart calculation from the coils. The lofted vessel wall [24] is implemented as an extended physical boundary to analyze the topological structures present in the plasma edge of the configurations considered in this work.

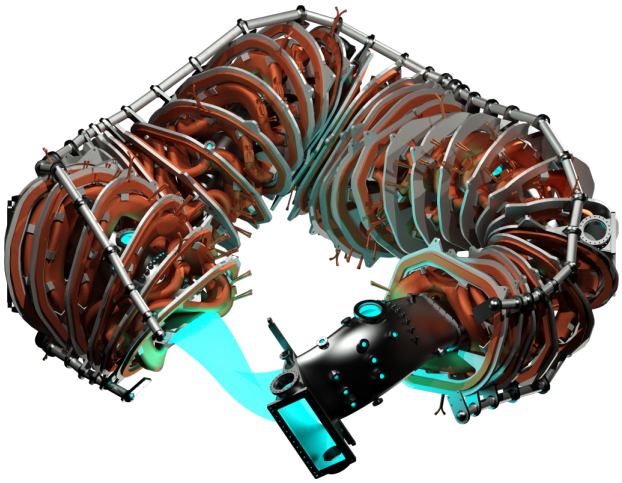

Figure 4.1: CAD rendering of HSX from https://hsx.wisc.edu/gallery/. The plasma is shown in cyan along with the vacuum vessel in gray which follows the shape of the plasma contour. There are 48 3D-shaped main coils (brown) and 48 planar auxiliary coils (gray).

HSX is a 4-field period stellarator with a minor radius of $a = 0.12\,\mathrm{m}$, a major radius of $R = 1.2\,\mathrm{m}$, and an aspect ratio of $R/a = 10$. The device is shown in figure 4.1 and it

is equipped with 48 3D-shaped main coils (brown) and 48 planar auxiliary coils (gray). A single field period is comprised of 12 main coils and 12 auxiliary coils. Furthermore, only 6 of the 12 main and 6 of the 12 auxiliary coils are unique because of stellarator symmetry. Altering the current in these coils enables the variation in plasma equilibrium. This includes allowing the rotational transform to be tailored to alter the magnetic structure in the plasma edge. Figure 4.2 provides a rotational transform profile ι inside the LCFS as a function of R of the four magnetic configurations considered in this chapter: the standard quasi-helically symmetric configuration (QHS), the small island configuration, the large island configuration, and the reduced trapped electron mode configuration (TEM) developed in [109].

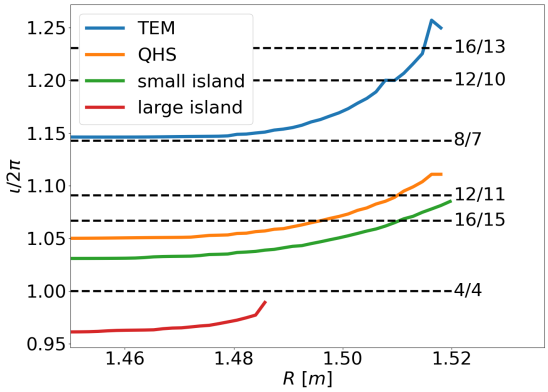

Figure 4.2: Rotational transform profile for the TEM (blue), QHS (orange), small island (green), and large island (red) magnetic configurations. The dashed black lines indicate different m/n rational surfaces.

The first three configurations are equilibria which are similar to the ones studied in reference [15]. They enable comparison with previous results but with a different wall location. These three configurations feature different island chains and flux tube substructure. This permits the study of variation in magnetic edge structure such as change in island size and location. The TEM case is a recently developed configuration due to the growing interest in turbulence optimized configurations [109] where the edge field line behavior has yet to be explored. The current values in the main and auxiliary coils for a single half-field period of each plasma configuration are tabulated in table 4.1. In figure 4.2, the dashed

lines in black indicate the different m/n rational surfaces, where m and n are integers. The large island configuration in red has the smallest core plasma volume because ι approaches the 4/4 rational surface at the edge as seen in figure 4.2. This case is characterized by the presence of the 4/4 island chain, which can be seen in figures 4.3 (c) and 4.4 (c). It will be shown that the presence of the 4/4 island chain and its intersection with the lofted wall makes this case the most "island-divertor-like" configuration in contrast to the others. Next, the small island and QHS cases in green and orange, respectively, both have ι which cross the 16/15 rational surfaces and approach higher-order rational surfaces, such as the 8/7 island chain. This will be discussed more in figures 4.3 (a)-(b) and 4.4 (a)-(b) where the location of the X and O-points of the 8/7 islands are plotted and influence the wall intersection pattern to be studied later. Finally, the TEM case in blue has the highest ι in contrast to the other 3 configurations along with an increased plasma volume. Figure 4.2 shows the higher-order rational surfaces that this profile crosses. The details about this magnetic configuration can be found in reference [109]. All cases of these configurations show that ι tends to increase especially toward the higher plasma edge values of R. These structures in the magnetic edge are systematically investigated in order to assess how the field line-intersection with the wall changes.

We will now present the edge magnetic structure for all four configurations displayed as contour maps of the connection length (L_C) in logarithmic scale. These are shown specifically for the $\phi = 5°$ and $\phi = 18°$ planes, respectively, of the four different magnetic configurations where ϕ and θ are the toroidal and poloidal angles respectively. These two toroidal angles were chosen to highlight some specific features of the HSX edge which will be emphasized in section 4.2. A Poincarè map is superimposed in black in each case along with the extended vessel wall. This analysis is displayed in Figures 4.3 and 4.4.

The connection length is the sum of the distances in the forward and backward directions along a field line until it strikes the lofted vessel wall. This computation was performed for a maximum L_C of 1 km in each direction, therefore, field lines in the confined plasma region that do not intersect the wall have maximum $L_C = 2$ km. This is shown as

white in the contour plots. Field lines radially outward of the core have $L_C < 2\,\text{km}$, and it is in this edge region of the plasma where the details of the L_C give rise to differences in magnetic configuration topology.

		Magnetic Configuration			
		TEM	QHS	Small Island	Large Island
Coil Type	Main Coil #1 (A)	-10722	-10722	-9649.8	-10722
	Main Coil #2 (A)	-10722	-10722	-10722	-10507.56
	Main Coil #3 (A)	-10722	-10722	-10722	-10722
	Main Coil #4 (A)	-10293.12	-10722	-10722	-10614.78
	Main Coil #5 (A)	-10722	-10722	-10722	-10722
	Main Coil #6 (A)	-9757.02	-10722	-9757.02	-10722
	Aux. Coil #1 (A)	15010.8	0	-15010.8	-15010.8
	Aux. Coil #2 (A)	15010.8	0	0	-15010.8
	Aux. Coil #3 (A)	15010.8	0	15010.8	-15010.8
	Aux. Coil #5 (A)	15010.8	0	0	-15010.8
	Aux. Coil #6 (A)	0	0	-15010.8	-15010.8

Table 4.1: Coil current amplitudes indicated for a half-field period for the studied magnetic configurations.

Starting with the large island magnetic configuration shown in figures 4.2 (red), 4.3 (c), and 4.4 (c), the 4/4 island chain dominates the plasma edge and the core plasma domain with closed flux surfaces is reduced. This is seen by the Poincaré map that is superimposed on these L_c figures. The figures shows that the islands are embedded in a region of chaotic field lines outside the LCFS. Around the islands in these figures, radially short collimated flux tubes of $L_C \leq 1\,\text{km}$ (yellow on the colorbar) overlap one another around the islands and create a chain of small secondary X-points. These are most visible in figures 4.11 (e) and 4.12 (d) to be discussed later. Each poloidal cross section in the two figures shows that the lofted wall intercepts islands in the edge making this configuration "island divertor-like". Although unlike the island divertor of W7-X, the intersection between the island and the wall is limited to the very outer edge of the island. Nevertheless, island divertor-like features are discernible while exhibiting resilient behavior with the lofted wall. This will be shown later when discussing the field line intersection pattern on the wall.

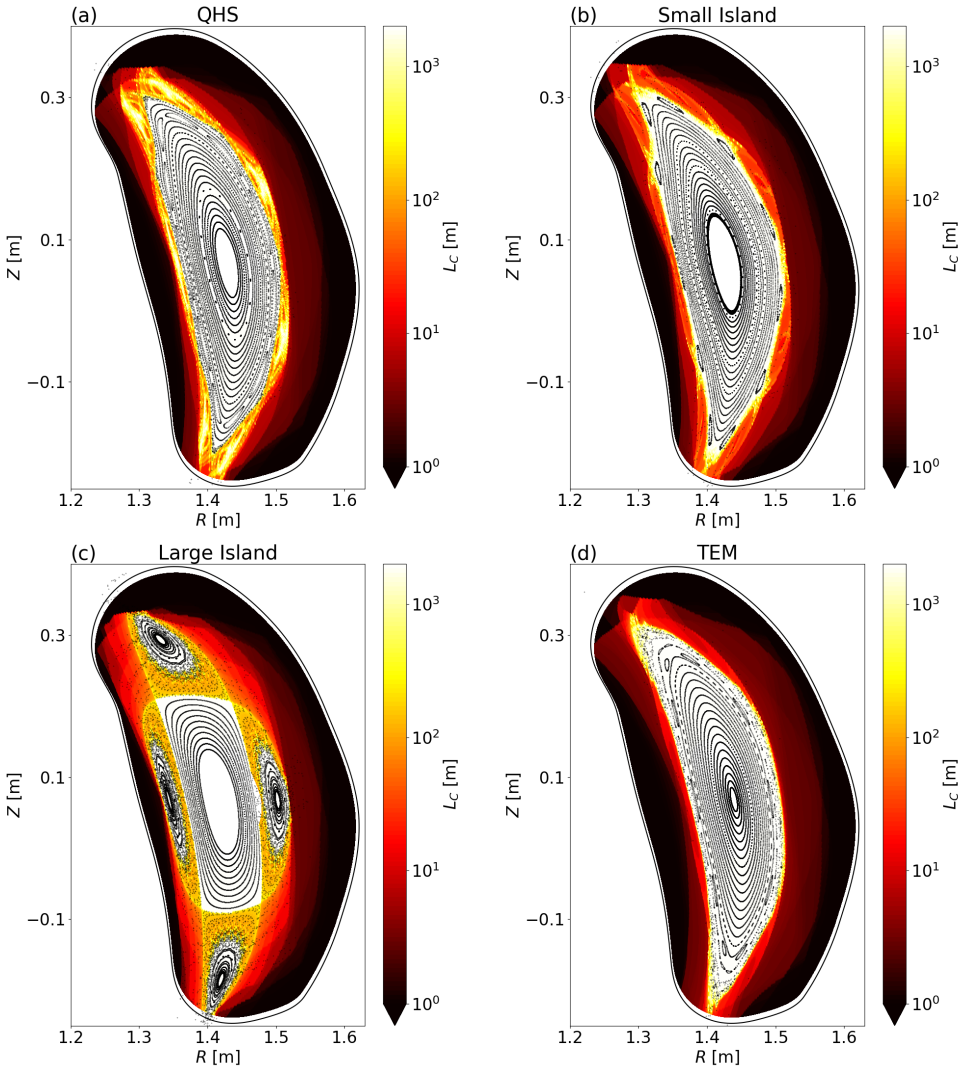

Figure 4.3: Connection length L_C contour map and Poincarè plots at $\phi = 5°$ for 4 different equilibria: (a) QHS, (b) small island, (c) large island, and (d) TEM.

Next, we discuss the small island configuration. The rotational transform is shown in green in figure 4.2, where the value approaches the 12/11 and 8/7 island chains at the edge. The 12/11 island chain is visible in the Poincaré plot. The 8/7 islands are also present in the edge. These islands are flattened and appear as red regions of medium connection length outside the confined plasma and intersect the wall as shown in figures 4.3 (b) and 4.4 (b). Small flux tubes of long L_C (yellow) are most visible and present near the X-points and resemble divertor legs. Figures 4.3 (b) and 4.4 (b) show that the

X-points at $(R, Z) \approx (1.4\,\mathrm{m}, -0.22\,\mathrm{m})$ and $(R, Z) \approx (1.37\,\mathrm{m}, -0.18\,\mathrm{m})$, respectively, have flux tubes (divertor legs) which are intercepted by the wall within a short radial distance. This intersection with the wall occurs poloidally in the region of highest curvature as seen in these figures. These X-points are magnified in figures 4.11 (d) and 4.12 (d) which will be discussed later.

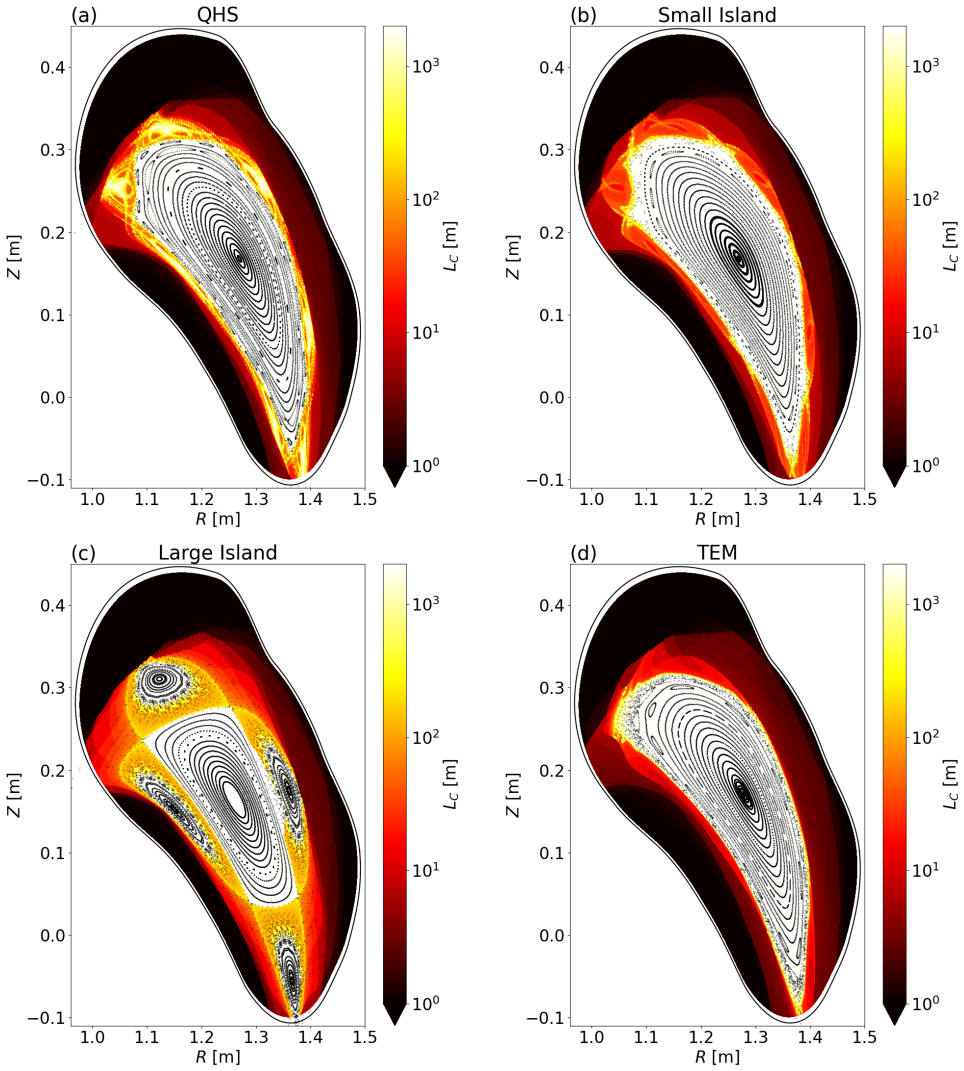

Figure 4.4: Connection length L_C contour map and Poincarè plots at $\phi = 18°$ for 4 different equilibria: (a) QHS, (b) small island, (c) large island, and (d) TEM.

This behavior can be contrasted with the QHS magnetic configuration shown in figures 4.3 (a) and 4.4 (a). The QHS case plasma edge also features the 8/7 island chain, as seen

in figures 4.2 (blue). Complicated internal structure of the island is visible with several regions of long, but not infinite, connection length. These flux tubes reach the vessel wall in regions of high curvature corresponding to $R \sim 1.4\,\mathrm{m}$ and minimum Z in figures 4.3 (a) and 4.4 (a). These flux tubes may be homoclinic and/or heteroclinic tangles mentioned in section 2.2 and observed in the CTH configurations in chapter 3. A similar flux tube presence observed in the TEM configuration case in figures 4.2 (orange), 4.3 (d), and 4.3 (d). However, due to the nature of the magnetic structure of this configuration, where no edge islands are visible of any size due to the island overlap of the 12/11 and 16/13 resonances, these flux tubes do not have a pronounced coherent shape like in the QHS and small island cases.

The selected magnetic configurations showcase a variety of magnetic edge structures that are present in stellarators: large islands, small islands, and chaotic substructures which feature collimated flux tubes. The next sections are dedicated to resolving the link between each magnetic configuration's plasma edge structure and the resulting field line-intersection pattern along the wall.

4.1.2 Magnetic Footprint on the Lofted Wall of HSX

Examination of the interaction of the magnetic field structure with the lofted wall is performed by calculating the field line-wall intersection pattern. In figures 4.5-4.7, a dense mesh approximately 0.5 cm away from the lofted vessel wall was generated to sample the field lines in the vicinity of the wall, similar to what was done for CTH in [18]. HSX has 4-field symmetry and previous work shows that the field line behavior for each half-field period is symmetric to the one in the next half-field period [15]. Therefore, we simulate the first half-field period in order to examine the details of the field line intersection pattern on the wall.

The magnetic footprint expected on the wall is shown in figure 4.5 as a contour map $L_C(\phi, \theta)$ distribution for all four magnetic configurations discussed. The magnetic footprint is calculated by starting the field lines near the wall and tracing them for 1 km or

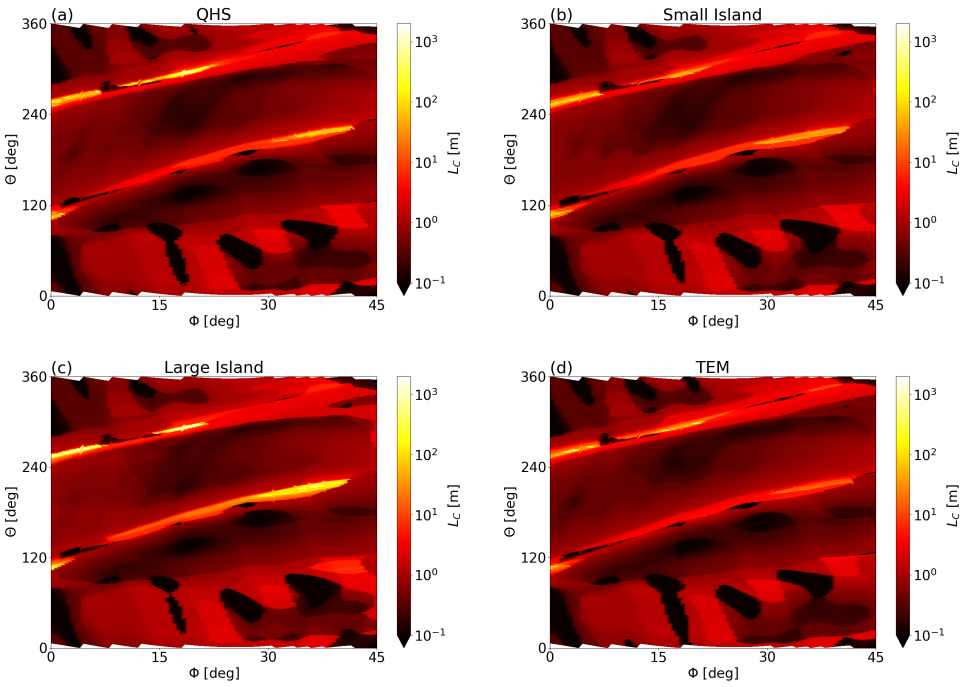

Figure 4.5: Magnetic footprint $\sim 0.5\,\text{cm}$ away from the expanded vessel wall for (a) QHS, (b) small island, (c) large island, and (d) TEM.

until they intersect the wall. Magnetic footprints in general serve as a proxy for heat and particle flux deposition on the PFC, where the actual value of L_C can be directly related to the heat flux [18], [85].

The resilient helical feature is observed by the long $L_C \sim 1\,\text{km}$ helical band corresponding to white and yellow on the colorbar. These helical bands of long L_C are approximately in the regions of $0° \leq \phi \leq 20°$ near $\theta \sim 240°$ along with $30° \leq \phi \leq 40°$ near $\theta \sim 200°$. The red and black regions of figure 4.5 with $L_C \leq 10\,\text{m}$ represent field lines of the far SOL. As these field lines are not contributing to the resilient helical band, their interaction will not be examined further. The most apparent difference can be seen between the large island result (figure 4.5 (c) and the TEM result (figure 4.5 (d)). Here the very bright region of very long connection length that is seen in the large island case is mostly missing in the TEM case. Nevertheless, it still manifests as a band of moderate (orange) connection length.

The field line intersection pattern on the mesh correlates strongly with the resilient

strike line feature of HSX seen in previous work [15]. We note that reference [15] did not observe resiliency for the large island case. This will be discussed later.

Across the four plasma configurations, there are minor differences observed between the different magnetic footprints seen in figure 4.5. These differences are based on what topological regions of the plasma edge are intercepted by the wall. This will be discussed later based on the details of figure 4.7 and further in subsection 4.2.

4.1.3 Radial Connection from Lofted Wall

Another figure of merit used in the tokamak community for characterization of resonant magnetic perturbations is the radial penetration depth of field lines [87], [110]. The purpose of this calculation is to quantify the deepest radial penetration of the field lines from along the PFC into the confined region with respect to the background equilibrium radial coordinate, the normalized poloidal flux ψ_N. With this metric, the field lines that can direct heat and energy via heat conduction and convection to the PFC have the deepest radial incursion ($\min(\psi_N) < 1$) [83], [87]. These calculations are typically done by evaluating the enclosed poloidal flux of the unperturbed (background) magnetic configuration. Then, field lines are launched in the perturbed configuration, while cataloging the minimum value of poloidal flux they reach. For the equilibria in this work, we attempt a similar calculation. However, there is no natural enclosed flux value that extends beyond the LCFS, therefore, we use a simplified approach. This is done by finding the minimum distance between a point along a field line's trajectory and the LCFS curve in the point's poloidal plane, and then taking the minimum of these values over the entire trajectory of the field line. We denote this as the radial connection ($\min(\delta_N)$) of the field line. The calculation is further complicated in that the LCFS differs significantly for each configuration. We choose to calculate each result with respect to the LCFS of each respective configuration. While this complicates comparisons across the configurations, it is necessary due to the significant LCFS differences.

Using the same mesh for the magnetic footprint computation, the minimum radial

connection $\min(\delta_N)$ of the field lines is simulated and plotted in figure 4.6. Similar to the magnetic footprint calculation, the field lines are followed for a maximum of $L_C = 1\,\text{km}$ in both directions. A positive $\min(\delta_N)$ indicates that this distance is radially outward from the LCFS. Like figure 4.5, the radial connection calculated on the mesh is qualitatively similar across the four cases despite the use of different LCFS values for all four configurations. Furthermore, the pattern of figure 4.6 also resembles the magnetic footprint pattern of figure 4.5. In the helical regions of long L_C in figure 4.5, the distance from the LCFS is minimal and corresponds to $\min(\delta_N) \sim 0.1\,\text{cm}$. This calculation combined with the magnetic footprint of figure 4.5 demonstrates that the resilient feature (regions of high L_C) seen across all configurations is dominated by long connection length field lines that approach very closely to the LCFS. These are the field lines that most influence the deposition of particles and energy onto the PFCs. This qualitative agreement can also be seen in figure 4.7 which shows $\min(\delta_N)$ and L_C on a higher resolution mesh for a smaller poloidal and toroidal range which will be discussed further in the next section.

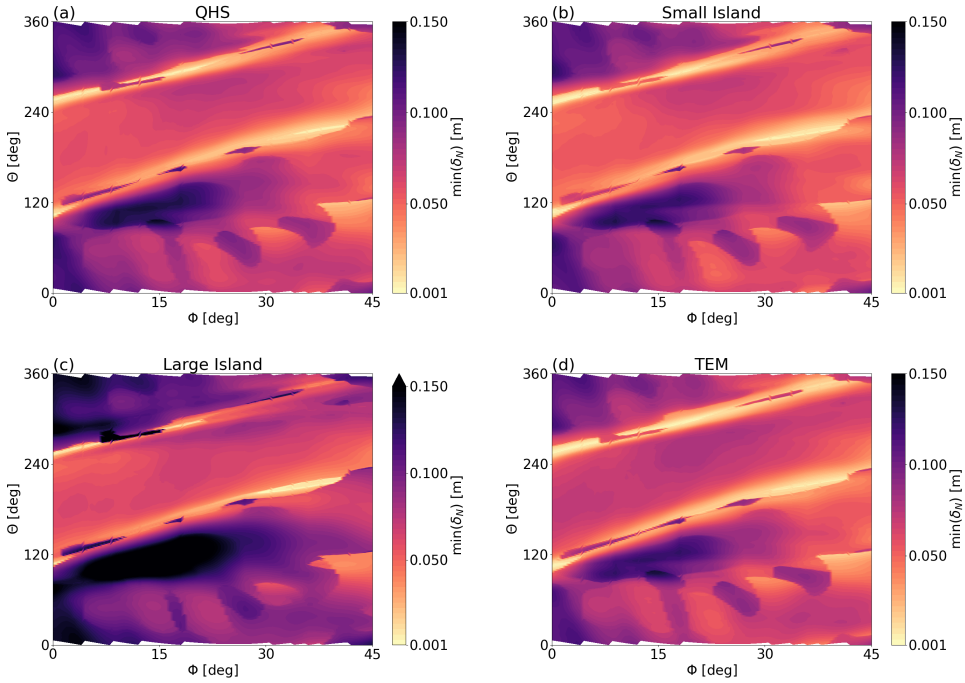

Figure 4.6: Radial connection $\sim 0.5\,\text{cm}$ away from the expanded vessel wall for (a) QHS, (b) small island, (c) large island, and (d) TEM.

From these figures, we observe that the deposition of particles and energy onto the PFC is connected to the plasma core via very long L_C with a short radial distance from the LCFS. The next section is dedicated to using L_C and $\min(\delta_N)$ together to quantify the differences within the details of the wall intersection pattern due to the different magnetic structures present across the edge configurations.

4.2 Radial Connection as a Metric for Determining Island Behavior

The previous sections convey that the relationship between L_C and $\min(\delta_N)$ of the field lines near the wall is an inverse one where large L_C is correlated with low $\min(\delta_N)$. We aim to quantify this relationship further in this section and with the results, we will associate the features of L_C and $\min(\delta_N)$ with resonant islands, cantori, and turnstiles. These results will guide the differences in the field line-wall intersection pattern across the different magnetic configurations which are emphasized through figures 4.7 - 4.12.

The plots in figure 4.7 are a higher resolution calculation of figures 4.5 and 4.6 for all four configurations considered. These plots in the figure are magnified to show the regions of $0° \leq \phi \leq 25°$ and $240° \leq \theta \leq 315°$. The left column is a contour map of $\min(\delta_N)$ and the right column displays the corresponding L_C for each case where the rows correspond to one configuration ((a) and (b) are QHS, for example). In these simulations, the computation was extended to a maximum $L_C = 10\,\text{km}$. The two localized regions of high L_C (one between $0° \leq \phi \leq 7°$ and the other at $15° \leq \phi \leq 22°$) correspond to regions of low $\min(\delta_N)$ across all of the magnetic configurations. The details of these localized regions, however, show that there are subtle differences in each configuration's wall intersection pattern.

Beginning with the small island configuration (figure 4.7 (c) and (d)), it is observed that the high L_C regions are mostly orange ($\mathcal{O}(10^2\text{m})$) with only some yellow ($\mathcal{O}(10^3\text{m})$) striations appearing between $0° \leq \phi \leq 7°$. The existence of very thin regions of long connection length indicates wall interaction with collimated flux tubes in the edge that

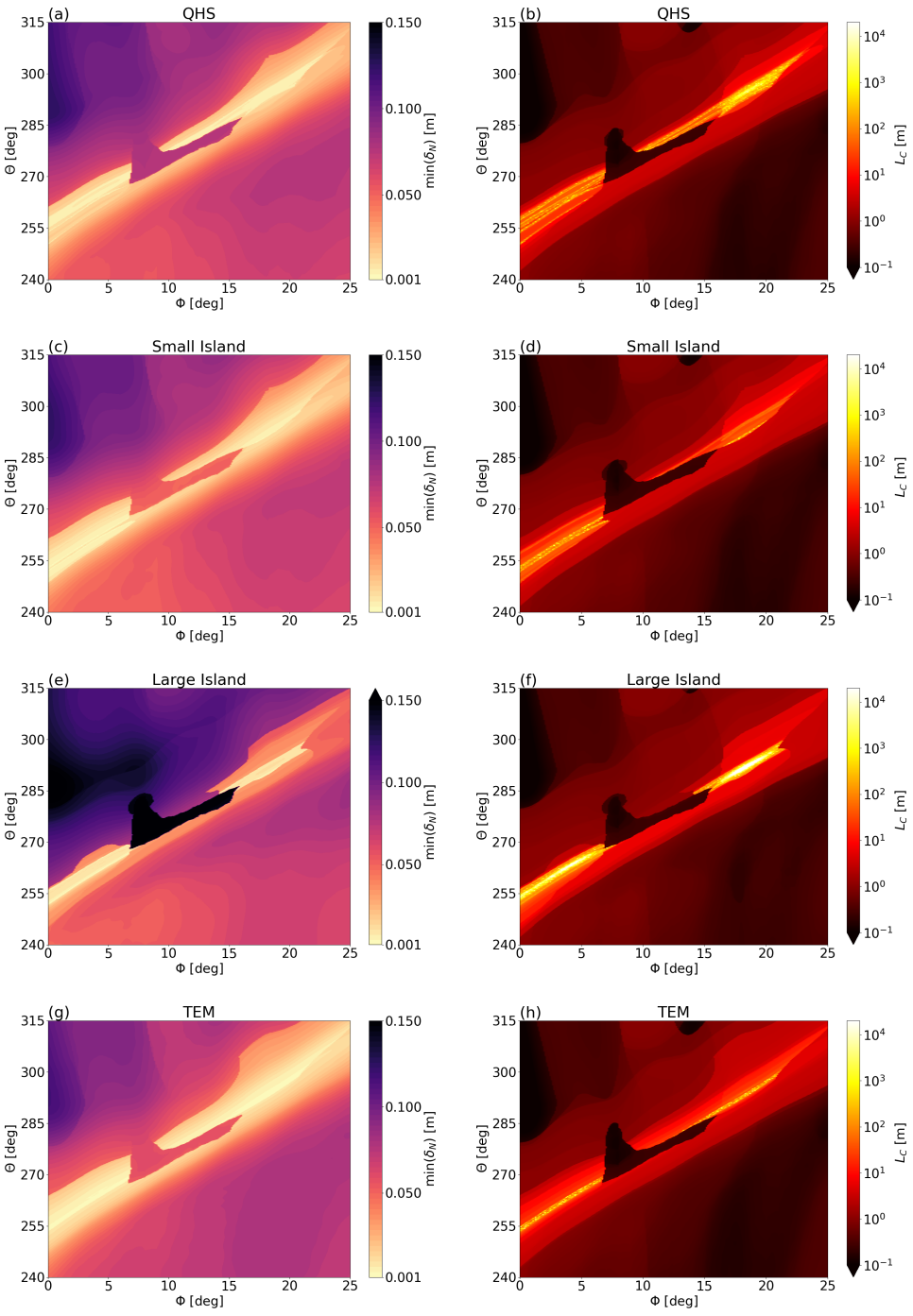

Figure 4.7: High resolution comparison of $\min(\delta_N)$ (left column) and L_C (right column).

extend toward the lofted wall. This pattern is similarly seen in the TEM case (figure 4.7 (g) and (h)) where the yellow striations also appear between $15° \leq \phi \leq 22°$. This is in contrast to the large island case (figure 4.7 (e) and (f)) which features a region of saturated L_C with less yellow sub-structure at very high L_C ($\mathcal{O}(10^3\text{m})$). Although the high L_C localization resembles the magnetic footprint structure of the CTH limited plasma wall scenarios in section 3.2.3, we will show later that this high L_C feature is due to the edge 4/4 island. Finally, the QHS plots (figure 4.7 (a) and (b)) exhibit both aspects that have just been described. Between $0° \leq \phi \leq 7°$ the high L_C area consists of yellow striations while between $15° \leq \phi \leq 22°$ there is some striation, however, a region of larger yellow localization is also present. The described high L_C features of the magnetic footprint are manifested similarly in the $\min(\delta_N)$ calculation where regions of high L_C correspond to low $\min(\delta_N)$. It will be shown that the regions of very localized and high L_C that lack yellow striations are due to the edge islands intercepting the wall. This will be done by highlighting the behavior of L_C and $\min(\delta_N)$ at $\phi = 5°$ and $\phi = 18°$ in the following paragraphs.

To better quantify the differences seen in the contour plot, we consider figures 4.8 and 4.9. The plots in these figures display L_C (left y-axis, solid lines) and $\min(\delta_N)$ (right y-axis, dashed lines) for a limited range of θ for only two toroidal angles from each plot of figure 4.7. Figure 4.8 shows $\phi = 5°$ while figure 4.9 shows $\phi = 18°$ for all four magnetic configurations. The distribution of L_C and $\min(\delta_N)$ are qualitatively characterized by a staircase-like distribution for $L_C \leq 10^2\text{m}$. This is an indication of the different nested connection length layers present in the plasma edge and has been seen in similar plots of L_C in devices such as Heliotron J [111], W7-AS [10], W7-X [112], and LHD [113]. Reference [111] shows the existence of a multi-fold layer consisting of constant L_C layers embedded within the chaotic structure in the plasma edge. Hence, this behavior of L_C, which is also associated with $\min(\delta_N)$, is consistent with what was seen in past work in different experimental devices. These constant L_C layers are similarly observed in figure 4.10 which will be discussed later.

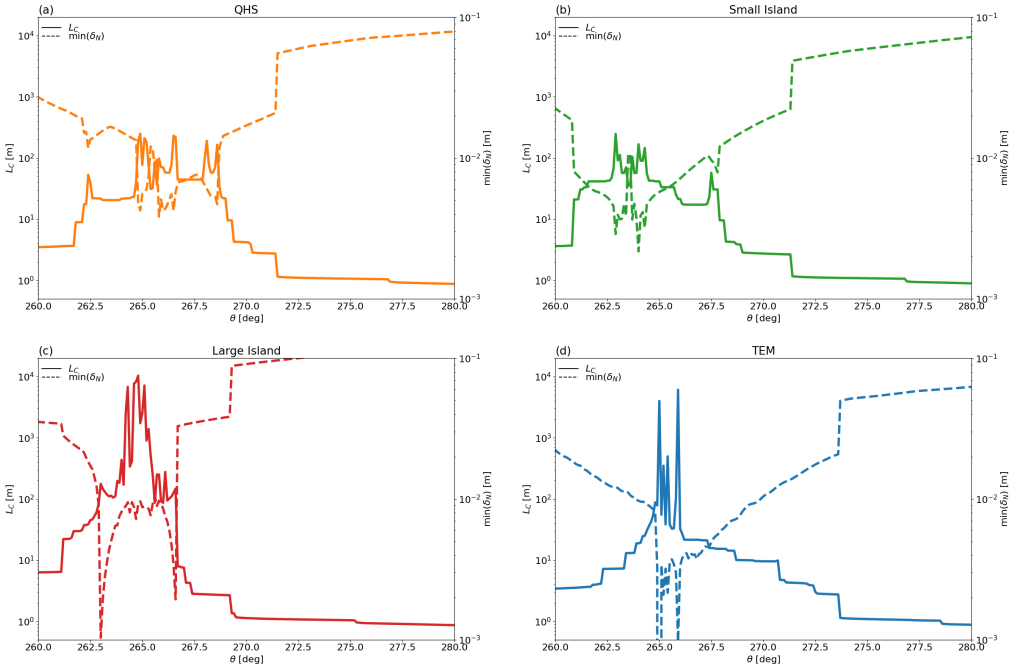

Figure 4.8: Each plot displays L_C (left y-axis, solid lines) and $\min(\delta_N)$ (right y-axis, dashed lines) as a function of θ at $\phi = 5°$ for the (a) QHS (orange), (b) small island (green), (c) large island (red), and (d) TEM (blue) configurations. This data is from figure 4.7.

Along with the aforementioned trend, figures 4.8 and 4.9 also demonstrate the differences in the influence of features in the open chaotic magnetic structure on the field line-wall intersection pattern, particularly for the areas of high L_C and low $\min(\delta_N)$. Figure 4.8 focuses on the poloidal region of $260° \leq \theta \leq 280°$ at $\phi = 5°$ while figure 4.9 focus on the poloidal region of $280° \leq \theta \leq 300°$ at $\phi = 18°$ from figure 4.7. As this calculation was performed for a maximum $L_C = 10\,\text{km}$, the only configuration with $L_C = 10\,\text{km}$ is the large island configuration (red) around $\theta \sim 290°$ in figure 4.9 (c) at $\phi = 18°$. This is where one of the 4/4 islands intersects the target surface. This is the only configuration with well-formed[1] islands intersecting the lofted wall. The QHS configuration ((a) orange) also has islands that intersect the wall, but they are not well-formed. Hence, the connection lengths are not as long in this region and are roughly up to $\mathcal{O}(10^2\text{m}) - \mathcal{O}(10^3\text{m})$. This is similarly observed in the small island configuration ((b) green) where the edge islands are

[1] We mean infinite L_C or in this case up to $L_C = 20\,\text{km}$ within the island.

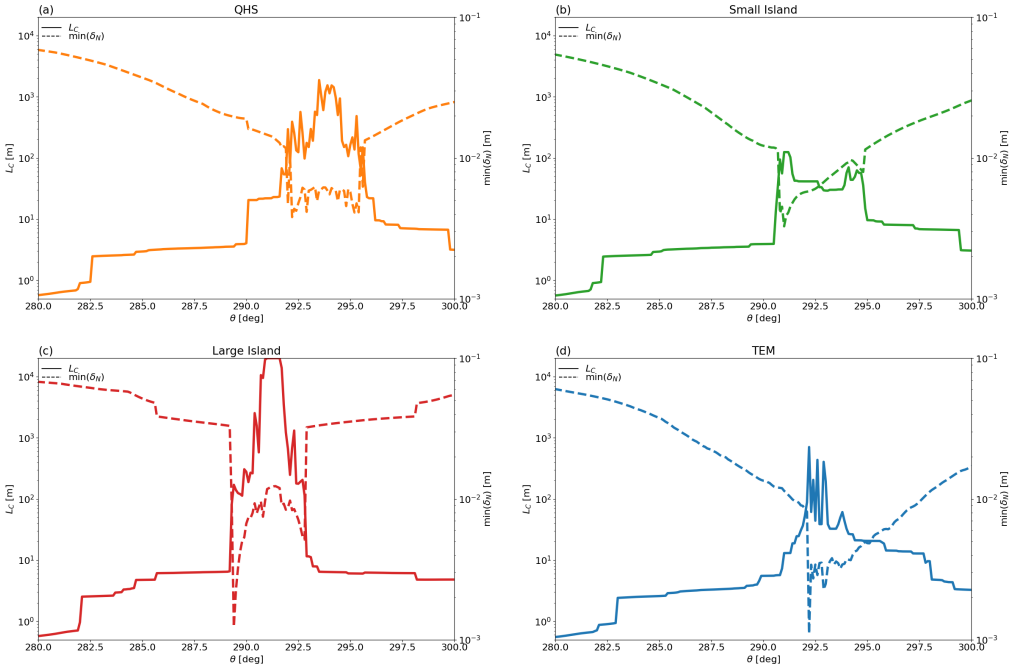

Figure 4.9: Each plot displays L_C (left y-axis, solid lines) and $\min(\delta_N)$ (right y-axis, dashed lines) as a function of θ at $\phi = 18°$ for the (a) QHS (orange), (b) small island (green), (c) large island (red), and (d) TEM (blue) configurations. This data is from figure 4.7.

even less formed and the maximum connection length is $\mathcal{O}(10^2\text{m})$. Finally, the TEM case ((d) blue) features long connection length field lines up to $\mathcal{O}(10^4\text{m})$ in the edge plotted in figure 4.8. This configuration has a large plasma volume extending toward the lofted wall where the edge region has open field lines from overlapping resonant islands. This can explain the presence of very high L_C close to the wall in the TEM case. The described features of the magnetic structure in the open chaotic layer intersecting the lofted wall with different values of L_C are also emphasized in figures 4.3, 4.4, 4.11, and 4.12.

Figures 4.8 and 4.9 with $\min(\delta_N)$ for all four configurations reveal that, although high L_C tends to be correlated with low $\min(\delta_N)$, the relation is nuanced. For example, the large island configuration shows that the field lines with $L_C \sim \mathcal{O}(10^4\text{m})$ at $\theta \sim 265°$ in figure 4.8 have $\min(\delta_N) \sim 10^{-2}\text{m}$. Meanwhile, the two smallest $\min(\delta_N) < 10^{-2}\text{m}$ in this figure occur when $L_C \sim 10^2\text{m}$. This is similarly observed in figure 4.9 (c) where field lines with $\min(\delta_N) \sim 10^{-2}\text{m}$ and $L_C \sim \mathcal{O}(10^4\text{m})$ are wedged between two $\min(\delta_N)$ minimums

in figure 4.9 (c). This behavior is not present in the other magnetic configurations.

It will be shown in figure 4.10 through the relationship between L_C and $\min(\delta_N)$ that this difference is due to edge island intersection with the wall in the large island case in contrast to the other cases. Figure 4.10 interprets figures 4.8 and 4.9 by plotting L_C versus $\min(\delta_N)$ for (a) $\phi = 5°$ and (b) $\phi = 18°$. The four configurations shown demonstrate the overall trend that L_C and $\min(\delta_N)$ have an inverse relationship. In order to analyze this relationship more quantitatively, we first describe how open field line trajectories have been described in the literature regarding chaotic magnetic structures. Recent theoretical work on the open field line behavior of NRDs have used power laws specifically for quantifying the probability that these field lines escape via turnstiles to intersect the wall/target [50], [51], [78]. Power laws in general have also been used to study the turnstile mechanism in chaotic systems [67]. Moreover, the rapid divergence of chaotic trajectories has also been studied via metrics such as Lyapunov exponents to quantify the level of chaos in these systems [114]. Thus, we apply an empirical power law as an ansatz for the relationship between the field lines' L_C and $\min(\delta_N)$. we employ a power law fit assuming $L_C = b\ \min(\delta_N)^a$ where a and b are parameters estimated in table 4.2 for each plot in figure 4.10. This fit is applied to the the small island configuration data (green) by performing a linear regression of the log-log data by linearizing $L_C = b\ \min(\delta_N)^a$ and a non-linear least-squares method from the SciPy library [115] is used to approximate a and b along with its error given by the covariance matrix calculated in this routine. The fit is overlaid in black in figure 4.10. While we use the power law scaling $L_C = b\ \min(\delta_N)^a$ to examine the general open field line behavior, the aim is to also explore if there are any deviations away from this scaling.

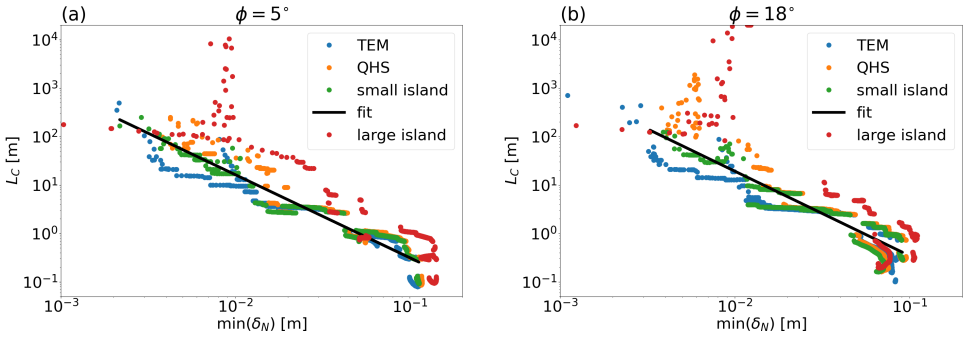

Figure 4.10: L_C vs $\min(\delta_N)$ for (a) $\phi = 5^\circ$ (from figure 4.8) and (b) $\phi = 18^\circ$ (from figure 4.9).

The small island configuration dataset was chosen for the fitting because it produced the highest quality power law. This configuration features an X-point very close to the wall as seen in figure 4.11 (c)-(d) and 4.12 (c)-(d). The values show that the exponential parameter a at the two different toroidal angles correspond with one another within a margin of error. The divertor legs of the X-point plotted in figures 4.11 (c)-(d) and 4.12 (c)-(d) clearly intercept the lofted vessel. This field line intersection pattern dominated by these divertor legs is another confirmation of the field line $\min(\delta_N)$ behavior along the separatrix.

figure	a	b
4.10 (a)	-1.71 ± 0.02	0.006 ± 0.0007
4.10 (b)	-1.74 ± 0.03	0.006 ± 0.0008

Table 4.2: Estimated values of a and b for figures 4.10 (a) and (b) assuming the relationship: $L_C = b \min(\delta_N)^a$. This fit is only performed for the small island configuration dataset.

The first observation in figure 4.10 (a) and (b) is that the configuration with the largest deviation from a power law is the large island case. The L_C versus $\min(\delta_N)$ relationship demonstrates that there is an apparent bifurcation in the behavior where very high L_C values have $\min(\delta_N) \sim 10^{-2}$m and do not follow the trend of the fitted power law in both figure 4.10 (a) and (b). This feature is somewhat weakly observed in the QHS case in figure 4.10 (b) for $\phi = 18^\circ$.

To explain this feature, figures 4.11 and 4.12 plot $\min(\delta_N)$ and L_C with an overlayed Poincarè map in black for $\phi = 5°$ and $\phi = 18°$, respectively, in the vicinity of the lofted wall. It is evident in the large island case in figures 4.11 (e)-(f) and 4.12 (e)-(f) that within an island $L_C \to \infty$. Hence, a field line that is started within an island will always remain separated from the LCFS and therefore have longer $\min(\delta_N)$. However, field lines about the X-point and along the divertor leg will have smaller $\min(\delta_N)$ because these field lines are diverted and quickly hit the PFC. This explains why in figure 4.10 the large island configuration has points in each branch of this bifurcated behavior depending on if the field line is near the leg of the X-point. This is similarly observed in the QHS case at $\phi = 18°$ of this figure, but because the edge island is less well-formed, the field lines' L_C are not as long as the field lines within the islands of the large island case. The edge island interaction described here also helps elucidate why there is a localization of high L_C ($\geq \mathcal{O}(10^3\text{m})$) in the large island case in figure 4.7 (f) and between $15° \leq \phi \leq 22°$ in the QHS case in figure 4.7 (b) due to the presence of an island and its location with respect to the lofted wall seen in figure 4.12 (b) at $\phi = 18°$.

Finally, the TEM configuration is considered. This case has the largest plasma volume out of all the cases where the LCFS is closest to the wall. The points from this dataset that follow the power law can be attributed to field lines near the LCFS which intercept the wall. Figures 4.11 (g)-(h) and 4.12 (g)-(h) show that outside the LCFS, the field lines appear quite chaotic which may be due to the presence and overlap of many high order edge islands. These field lines near the wall resemble a broken flux surface. Moreover, as this configuration does not feature a large island that intercepts the wall, the field lines at the wall similarly follow the empirical power law trend. This configuration's field line interaction with the wall appears similar to the small island case.

In this section, we have described how field lines that deviate from the empirical power law are correlated with island-wall interaction for the resilient field line feature. When the field lines approximately follow this power law relation, it suggests that these field lines are near or along the separatrix. This behavior of long L_C near the separatrix or

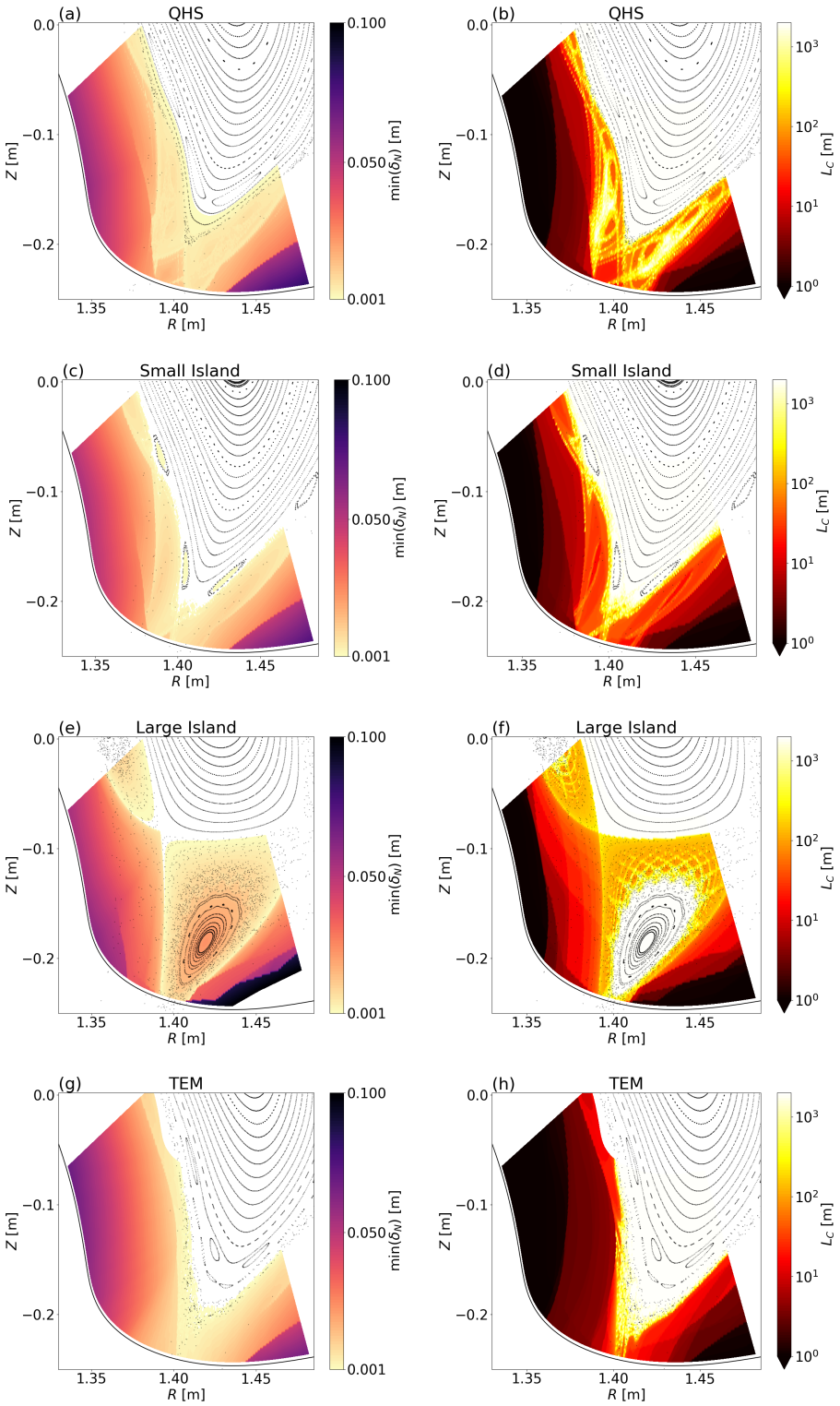

Figure 4.11: High resolution figures of the footprint corresponding to $\phi = 5°$ for each magnetic configuration. The right column is the connection length and the left column is the radial connection.

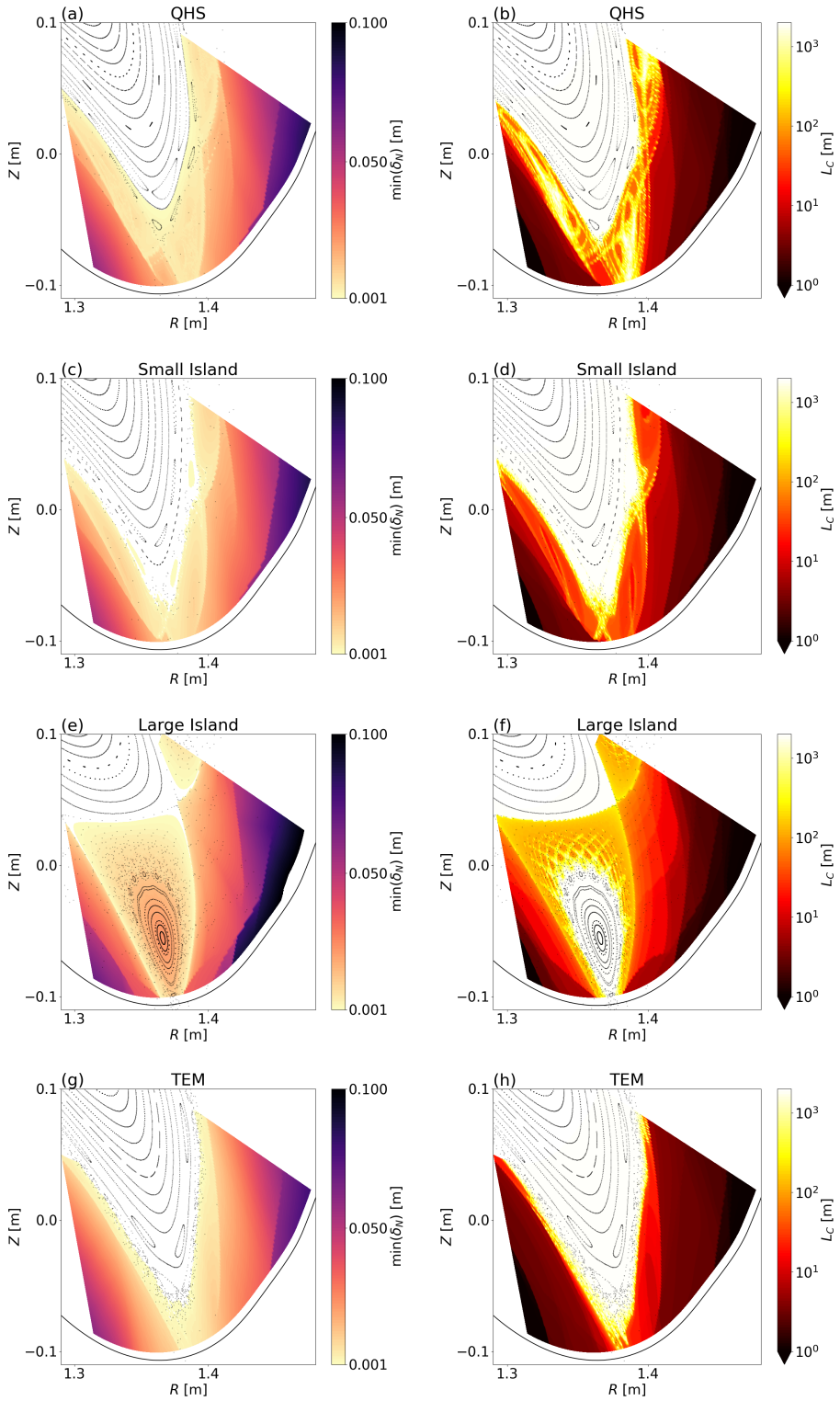

Figure 4.12: High resolution figures of the footprint corresponding to $\phi = 18°$ for each magnetic configuration. The right column is the connection length and the left column is the radial connection.

LCFS is consistent with what is described in reference [116] where it is suggested that field lines in the edge region which take the most transits tend be closest to the LCFS due to their interaction with cantori. Cantori act as partial transport barriers for field lines outside the confined region as described in section 2.2. This is why field lines can take many transits before eventually escaping through and reaching a PFC. The behavior of field lines escaping through cantori via turnstiles has been described in references [51], [78], [116] as the magnetic mechanism for non-resonant divertors. Thus, the field lines which follow the power law relationship with $L_C \geq 10^2$m and $\min(\delta_N) < 10^{-2}$m suggest interaction with cantori before eventually striking the lofted wall through turnstiles and appear as collimated flux tubes in the edge. This appears to be what is observed in the QHS, small island, and TEM configurations which have long L_C striations in the resilient field line region in figure 4.7. These striations can be connected to the flux tube magnetic edge structure shown in figure 4.11 which have high L_C and low $\min(\delta_N)$ near the lofted wall.

4.3 Summary of Field Line Following Edge Analysis in HSX

In this study, an expanded vessel wall, called the lofted wall, was used and a new metric, $\min(\delta_N)$ was introduced to quantify the structural differences of the field lines within the wall footprint. The results demonstrate that regardless of the magnetic configuration, the field lines intersect the lofted wall in a general helical band. Specifically, the regions of high L_C, which are the anticipated heat and particle flux regions, agree in general with low $\min(\delta_N)$ despite the vast differences in the open chaotic edge structure across the configurations. Introducing the minimum distance to the LCFS $\min(\delta_N)$ of the edge field lines provides insight regarding the structures responsible for the helical intersection pattern across the different magnetic configurations. The relationship between L_C and $\min(\delta_N)$ reveal that the presence of large islands near the PFC impact the helical strike line differently than the other cases. For the large island configuration specifically, this relationship revealed that field lines within an island that have long L_C tend to have lower

$\min(\delta_N)$ in comparison with the other magnetic configurations.

The field lines with largest values of connection length confirm what is described in reference [116] where field lines outside and nearest the LCFS which take many transits $L_C \to \infty$ until they impact the PFC are interacting with cantori. However, field lines in the vicinity of an edge island also behave similarly with $L_C \to \infty$. Figure 4.10 shows that the difference between island and cantori field line behavior may be manifested in the minimum radial connection of the field line with respect to the LCFS. Namely, the field lines which do not follow the power law with $\min(\delta_N) \sim 10^{-2}$m as their L_C becomes longer and longer are within an edge island. The field lines which follow a power law are close to the separatrix where very long L_C combine with very small $\min(\delta_N)$ may stay close to the LCFS or separatrix due to interaction with cantori. The study of field lines behavior crossing cantori and escaping through turnstiles has been studied for NRDs in references [50], [51], [78] where the probability of field lines lost to the wall through turnstiles assumes a power law. Thus, we employed an empirical power law to describe trend of the open field lines in the vicinity of the wall to study and distinguish the different magnetic edge structures.

Despite these noted field line behavior differences, identification of this overall resilient helical strike line for the lofted wall is fundamentally important for future design and implementation of a baffled divertor unit which can support neutral particle compression and hence particle exhaust. Figure 4.13 plots the current HSX wall as a dashed black line while the lofted wall is plotted as a solid black line. This is depicted for the QHS and large island configuration. The lofted wall's expanded physical position allows space for a mechanical divertor which was previously not possible due to the close proximity of the current wall to the QHS LCFS shown in figure 4.13. The placement of the current wall also helps elucidate why the large island configuration was previously not included in the resilient strike line calculated in reference [15]. The difference here is that a further expanded vessel wall was implemented as the PFC. The results demonstrate that if a large island is present and the wall or divertor target is outside of the island or separatrix,

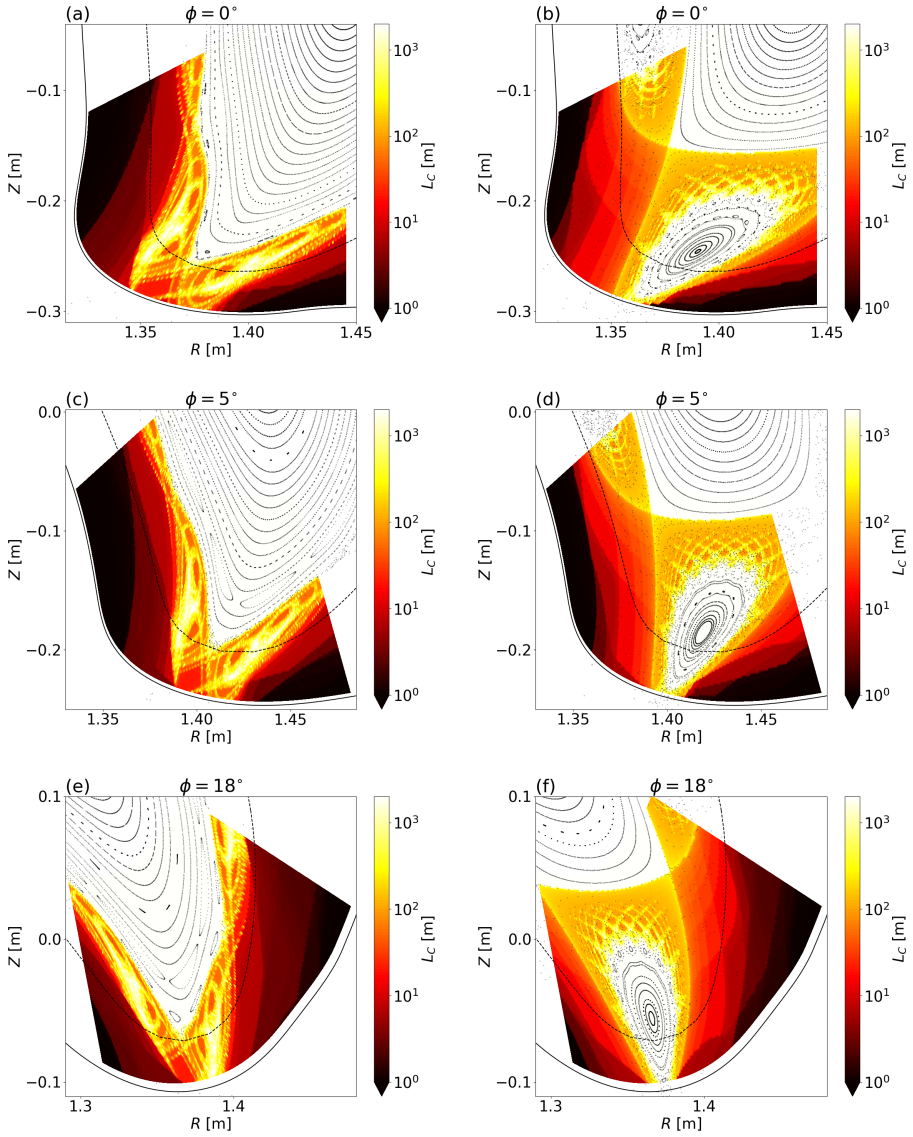

Figure 4.13: Current wall (dashed black line) and lofted wall (solid black line) superimposed on the connection length contour map of magnified poloidal cross sections near the strike line location at $\phi = 0°,\ 5°,$ and $18°$. The left and right columns plot the QHS and large island configurations, respectively.

then resilient field line-wall interaction is observed. This is similarly seen in reference [14], and is different than what is observed in the W7-X island divertor configuration or in reference [15] where the PFC in both cases deeply intersects the islands. Such effects of island divertor SOL geometry in W7-X has recently been shown to influence detachment behavior [117] and lack of efficient neutral exhaust [118]. Thus, future work in resilient divertors in general must simulate divertor performance, such as what is done in [119], since NRD research to date has focused on the behavior of magnetic field lines in the plasma edge. This is very important to assess the viability of the NRD for future stellarator fusion reactors. Moreover, this motivates the next chapter which will model the plasma edge transport behavior with the EMC3-EIRENE code to confirm the heat and particle flux deposition on the lofted wall for the large island and QHS configurations.

In this thesis, by introducing the metric $\min(\delta_N)$ for field lines and analyzing their relationship with field lines' L_C, we have distinguished between island versus NRD-like field line behavior within the resilient field line behavior in HSX. This is in contrast to what was shown in chapter 3 where the field line analysis in CTH helped distinguish between limited versus diverted behavior of the resilient strike line. These field line analysis tools show that by examining the details within the resilient feature of the field lines, we can determine if the magnetic edge structure of a plasma configuration and its proximity to the PFC is limited, island-diverted, or non-resonant diverted. This magnetic structure identification helps scope out implementation of a potential mechanical structure for resilient stellarator divertor studies.

Chapter 5

Analysis of Plasma Edge Transport and Divertor Conditions in HSX Using EMC3-EIRENE

The following chapter attempts to analyze the transport in the plasma edge of HSX on the simulated lofted wall with EMC3-EIRENE. The configurations studied in this chapter are selected based on their magnetic edge structure featuring island chains of different size and location with respect to the PFC. Additionally, since generation of an EMC3-EIRENE field-aligned grid is challenging, we show a limited number of results for two selected magnetic configurations from the last chapter. Namely, we study the QHS and large island configurations. To generate these field-aligned grids, FLARE's mesh-generation capability described in section 2.3.4 was used in addition to the field line tracing analysis performed in the previous chapters.

Previous studies of the edge transport in HSX using EMC3-EIRENE have been done in reference [120]. This reference studied HSX and a 2 times scaled HSX with the current wall. The plasma edge transport simulated in this chapter, however, adds to the results of

the last chapters. These results resolved the features of the overall resilient strike line due to island or chaotic magnetic structures via field line tracing. The aim of this chapter is to make use of the analysis into the structural details and characterization of the strike line resiliency and connect this to the plasma edge transport modeled with the EMC3-EIRENE code. We note that the EMC3-EIRENE code has undergone several improvements over the last 12 years, especially with regard to detachment calculations [95], [121].

The layout of this chapter is as follows. Section 5.1 provides the simulation set up for modeling the plasma edge transport of both magnetic equilibira with EMC3-EIRENE. This is followed by comparison of the simulated heat and particle flux deposition pattern with the results from field line following in chapter 4. After, a discussion on the basic SOL transport behavior is provided in context of scoping out detachment in HSX with the lofted wall. Then, section 5.2 details the power losses manifested in the EMC3-EIRENE simulations from grid misalignment issues. Potential improvements for future divertor transport modeling in HSX are also discussed here. Finally, we summarize this chapter in section 5.3.

5.1 Simulation Results for QHS and Large Island Cases

For consistency with chapter 4, the lofted wall [24] is used rather than the current vessel wall as the main PFC. Since the lofted wall increases the width of the plasma edge, this is a continued computational exercise to examine the impact of complex structures present in the edge on the plasma edge transport. Like what was shown in the previous chapter, the additional space enables the exploration of divertor features in HSX. Thus, simulating the plasma edge transport behavior with EMC3-EIRENE is an initial scoping study into how to implement a divertor structure in HSX. Moreover, the set input power and upstream densities are chosen to exceed the device's current experimental limitations. This is done at high operational limits to assess whether divertor detachment could be reached in HSX with the lofted wall. Furthermore, this chapter serves as a basis for future grid improvements for analysis of the edge plasma transport with EMC3-EIRENE.

magnetic configuration	number of zones	n_t	n_r	n_p
QHS	5	10	170	400
Large Island	5	10	183	400

Table 5.1: Grid resolution for the QHS and large island configurations where n_t is the number of toroidal cells, n_r number of radial cells, and n_p number of poloidal cells per zone.

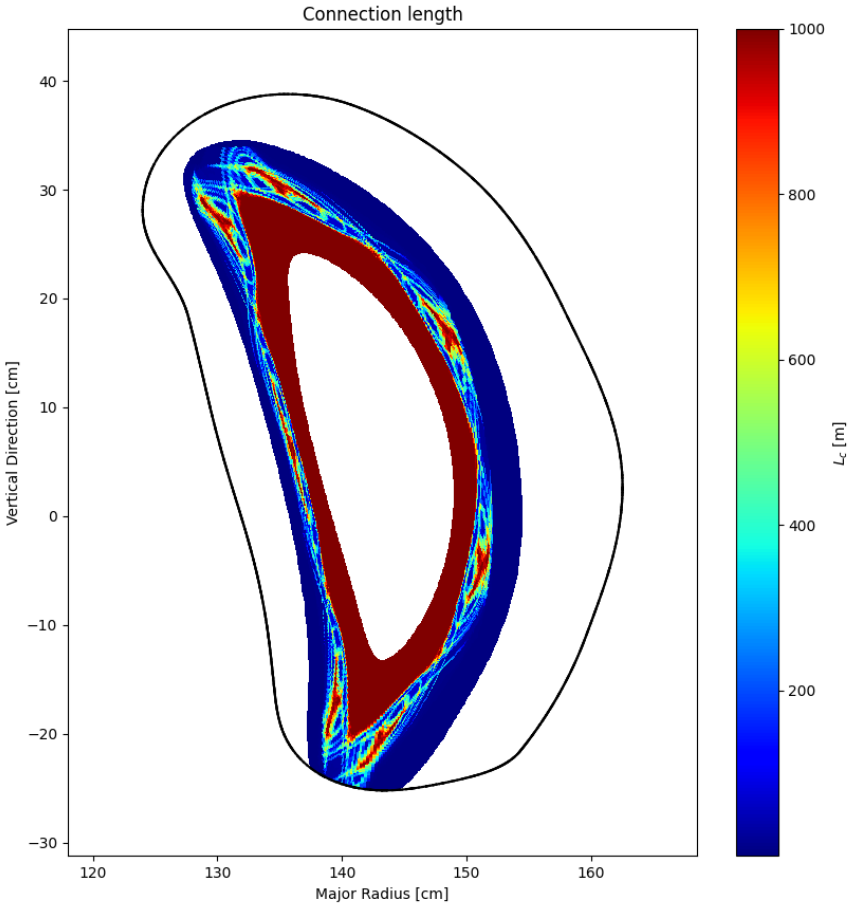

Figure 5.1: Connection length map at $\phi = 4.5°$ for the QHS configuration generated with EMC3-EIRENE and not FLARE like in chapter 4. The region of connection length is calculated on the plasma domain of the EMC3-EIRENE grid. This shows that plasma domain encompasses the chaotic region along with the 8/7 island chain and extends toward the wall.

We continue with a description of the simulation set up. The procedure described in section 2.3.4 is applied to the QHS configuration. As the plasma domain must extend to the wall, grid generation is challenging for this configuration since chapter 4 showed that outside the LCFS there is an open chaotic layer in the edge that extends toward the wall for the QHS case. More specifically, the edge region featuring the 8/7 island chain has long and short L_C flux tubes outside of the confined plasma region and is shown in figure 5.1 for $\phi = 4.5°$. Thus, creating a smooth toroidal surface as the outer boundary of the EMC3-EIRENE plasma domain mesh complicates this task. In general, it is because of the increasing proximity of the plasma grid toward the coils which introduces large radial values of the field along with the complexity of the open field line region from large magnetic shear and the presence of islands among other topological structures that the cells of the plasma domain tend to be susceptible to cell deformation. This is complicated further by employing the lofted wall as the main PFC since this wall is meant to be as close as physically possible to the physical coil. Radially expanding the computational plasma domain toward the lofted wall to capture more plasma can cause further cell deformation due to the described open field line region complexity. Additionally, the lofted wall is a highly shaped vessel which can also lead to further grid cell deformation, especially in the regions with high curvature. To help with this, the half-field period simulation domain, which represents 1/8 of HSX since it is 4-fold symmetric, is broken up into 5 zones. By increasing the number of zones, this can help mitigate cell deformation and improve representation of the magnetic field [122], similar to what was described in section 2.3.4 in the 10 kA CTH configuration which was split into 2 zones[1]. Table 5.1 lists the toroidal, radial, and poloidal resolution ($n_t,\ n_r,\ n_p$ respectively) per zone for the QHS grid and the large island configuration's grid. Figure 5.1[2] shows the extent of the plasma domain of the EMC3-EIRENE grid for the QHS generation at $\phi = 4.5°$. This connection length calculation is performed with EMC3-EIRENE and shows that the plasma domain

[1]It should be noted that disadvantages of splitting the toroidal domain this way include increased computation time and misalignment of the zones. The latter is discussed at length in section 5.2.

[2]This poloidal cross section was used to generate the first zone spanning $\phi \in [0°, 9°]$ of the QHS EMC3-EIRENE grid.

encompasses closed flux surfaces (deep red $L_C \sim \mathcal{O}(1\,\mathrm{km})$) and region outside the LCFS including the open chaotic layer (yellow to light blue L_C) along with the 8/7 island chain (red to yellow L_C). This plasma domain is separate from the neutral domain of the EMC3-EIRENE grid.

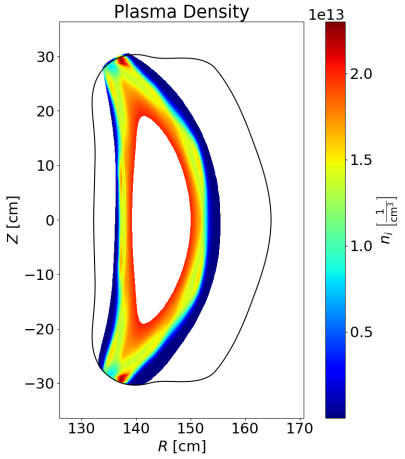

(a) QHS $n_e = 2 \times 10^{13}$ cm^{-3}

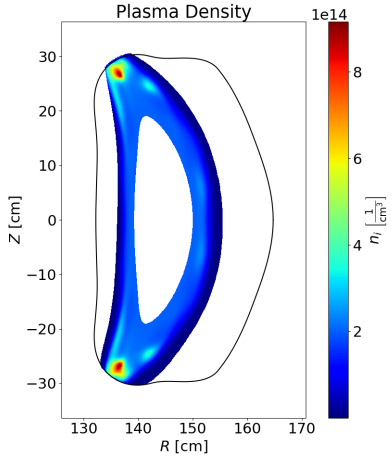

(b) QHS $n_e = 20 \times 10^{13}$ cm^{-3}

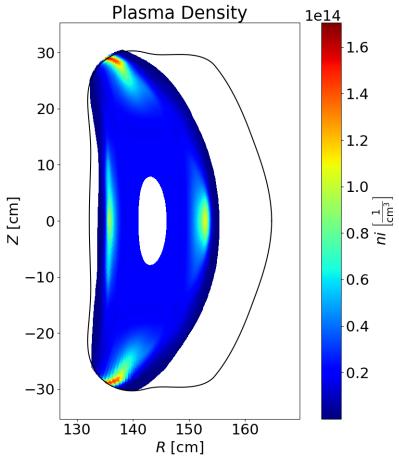

(c) Large island $n_e = 2 \times 10^{13}$ cm^{-3}

Figure 5.2: n_i profile at $\phi = 0°$ of the QHS configuration with n_e of (a) 2×10^{13} cm^{-3} and (b) 20×10^{13} cm^{-3} along with (c) the large island configuration with n_e of 2×10^{13} cm^{-3}.

The total device input power is set to 500 kW corresponding to a power of 62.5 kW per half-field period. The perpendicular transport coefficients were set to: particle diffusion $D = 0.25\,\mathrm{m}^2/\mathrm{s}$ along with ion/electron thermal diffusion $\chi_{i/e} = 0.75\,\mathrm{m}^2/\mathrm{s}$, although previous experimental studies indicated smaller anomalous transport coefficients are possible

[89]. We note that these diffusion values are lower than what was selected in the CTH simulations in section 3.3. Furthermore, no impurities were included in the modeling. These parameters were fixed across all simulations except for the density set at the inner boundary (also referred to here as the upstream density n_u). For QHS, this density varied between 2×10^{13} cm^{-3} $\leq n_e \leq$ 20×10^{13} cm^{-3} while for the large island configuration only 2×10^{13} cm^{-3} and 3×10^{13} cm^{-3} were modeled.

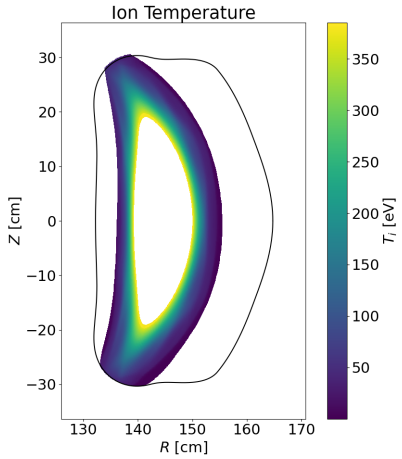

(a) QHS $n_e = 2 \times 10^{13}$ cm^{-3}

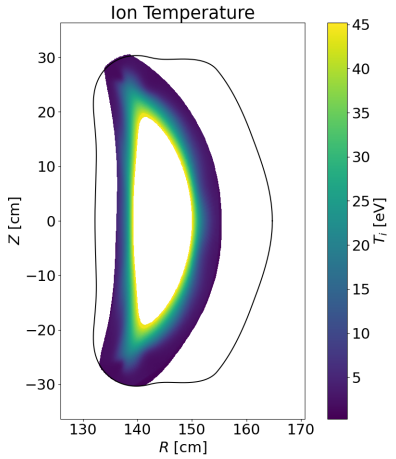

(b) QHS $n_e = 20 \times 10^{13}$ cm^{-3}

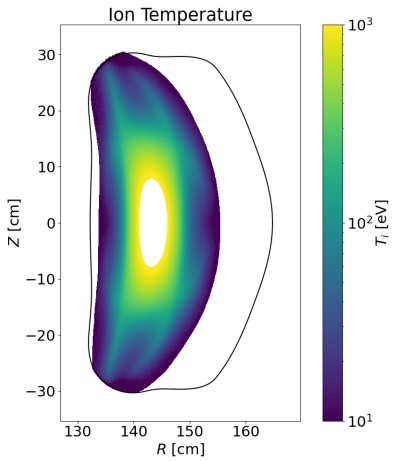

(c) Large Island $n_e = 2 \times 10^{13}$ cm^{-3}

Figure 5.3: T_i profile at $\phi = 0°$ of the QHS configuration with n_e of (a) 2×10^{13} cm^{-3} and (b) 20×10^{13} cm^{-3} along with (c) the large island configuration with n_e of 2×10^{13} cm^{-3}.

Figures 5.2, 5.3, and 5.4 show the ion temperature T_i, ion density n_i, and Mach number M profiles, respectively, from EMC3-EIRENE modeling. These profiles are given at $\phi = 0°$

for the lowest and highest cases of the density scan for QHS (figures 5.2 (a)-(b), 5.3 (a)-(b), and 5.4 (a)-(b)) and only the lowest density for the large island case (figures 5.2 (c), 5.3 (c), and 5.4 (c)). Across these figures corresponding to the QHS configuration, the 8/7 island chain visibly influences the shaping of the n_i, T_i, and M profiles. The influence of the 8/7 island structure on these quantities is consistent with previous simulation and experimental observations [15], [89]. For the large island case, the 4/4 island chain has a similar impact on the shaping of the n_i, T_i, and M profiles. Within the island O-points in both configurations, there is some density build-up seen in figure 5.2 corresponding to each plot's colorbar (yellow to green). This build-up is largest near the target (red) and, at this toroidal angle, this peak region corresponds with the strike point on the wall. In figure 5.4, counter-streaming flows can be seen around the island O-points and are oppositely directed at the X-points. The observed flow structure in both the open chaotic layer in the QHS case and the island chain in the large island case convey how the SOL is organized into flux channels which deposit particles and energy to the target. Particles which enter the SOL via perpendicular transport are accelerated along the open field lines of these flow channels by the pressure gradient along these field lines [40]. We will continue to discuss the flow structure in relation to the chaotic edge structures identified in the previous chapter in figures 5.5 and 5.6 later in this section.

Furthermore, we see that by increasing n_u for the QHS case, this results in T_i decreasing significantly in figure 5.3 indicating plasma recombination and the generation of neutral gas. In section 5.2, analysis of the power balance demonstrates that at this high n_u, power is radiated due to interactions with neutral gas. Along with a description and analysis of the power balance in the SOL, section 5.2 also details the power loss mechanisms due to misalignments of the field-aligned grid. We continue to examine plasma profiles and relate the edge structure to what was found in the previous chapter with FLARE. The heat and particle flux deposition on the wall are then compared with field line following.

To examine the field line magnetic structure alongside the EMC3-EIRENE calculated plasma profiles, we consider figures 5.5 and 5.6. Plots (a) and (b) show the Mach number

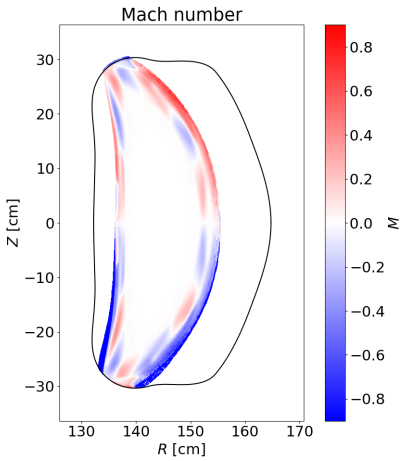

(a) QHS $n_e = 2 \times 10^{13}$ cm^{-3}

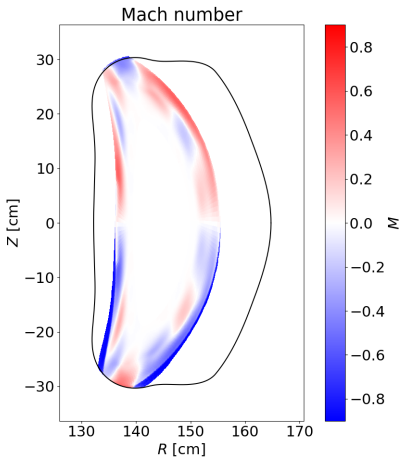

(b) QHS $n_e = 20 \times 10^{13}$ cm^{-3}

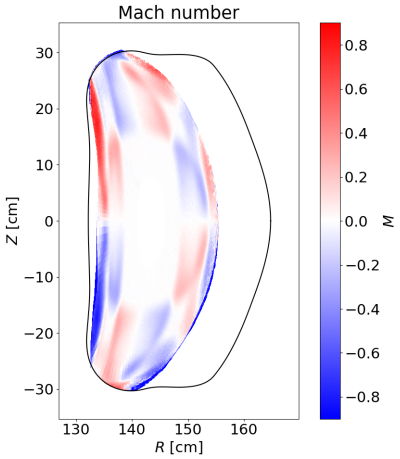

(c) Large Island $n_e = 2 \times 10^{13}$ cm^{-3}

Figure 5.4: M profile at $\phi = 0°$ of the QHS configuration with n_e of (a) 2×10^{13} cm^{-3} and (b) 20×10^{13} cm^{-3} along with (c) the large island configuration with n_e of 2×10^{13} cm^{-3}.

(M) and electron temperature (T_e) profiles, respectively, in a magnified region of the $\phi = 0°$ poloidal cross section near the strike line at the target. These profiles are for the lowest n_u of 2×10^{13} cm^{-3} for both QHS and large island configurations. The FLARE calculated L_C for the corresponding poloidal region is plotted in (c) of figures 5.5 and 5.6. While the overall influence of the island chains for each magnetic configuration's plasma edge is visible in the M and T_e profiles, we note that these profiles do not capture all details of the high L_C ($\mathcal{O}(10^3\text{m})$) yellow substructure which surround the major O-points displayed in figures 5.5 and 5.6 (c). In the large island configuration, these substructures are the

noted secondary X-points around the 4/4 island O-point. Meanwhile, the substructure outside of the O-point of the 8/7 chain in the QHS configuration resembles collimated flux tubes which extend toward the target and the confined plasma region. The flow pattern in figures 5.4 (a) and (b) and 5.5 (a) demonstrates that counter streaming flows are present in the open chaotic layer in the QHS configuration. Like what is seen in the large island configuration which features the 4/4 island chain, however, the flow pattern appears to mostly follow the island structure. The fine L_C substructures in the chaotic edge observed in figures 5.5 (c) and 5.6 (c) appear to not be reflected in the flow pattern nor in the T_e profile. This may be a result of the perpendicular particle transport exceeding local parallel transport within the chaotic substructures. Rather, the pattern of M and T_e in this region pattern follow the larger magnetic structures in the SOL which are the 8/7 and 4/4 island chains for the QHS and large island configurations, respectively.

However, these substructures may also not be reflected M and T_e profiles due to limitations in the EMC3-EIRENE simulation. It has been shown in references [63] that the role of diffusion tends to obscure the detailed features/patterns of these smaller scale magnetic structures, particularly for the heat and particle flux deposition on the PFC. We note that the diffusion of $D = 1$ m^2/s was selected in [119], however, lower diffusion values were employed here to more closely agree with what was measured experimentally in reference [89]. In reference [89], a local value of $0.03\,\mathrm{m}^2/\mathrm{s}$ was measured. However, lower values of diffusion could not be pursued further with EMC3-EIRENE due to unresolved simulation issues including longer computation time and numerical instabilities with respect to simulation convergence. The inclusion of diffusion is relevant to note since plots (c) of figure 5.5 and 5.6 were generated without diffusion in FLARE. It should also be noted that resolution of the EMC3-EIRENE field-aligned grid may also hinder resolving these finer magnetic substructures. This must be studied further, particularly for magnetic configurations like the QHS configuration, which have a complex chaotic structures along with islands.

The last chapter showed that the resilient strike line persists across the studied mag-

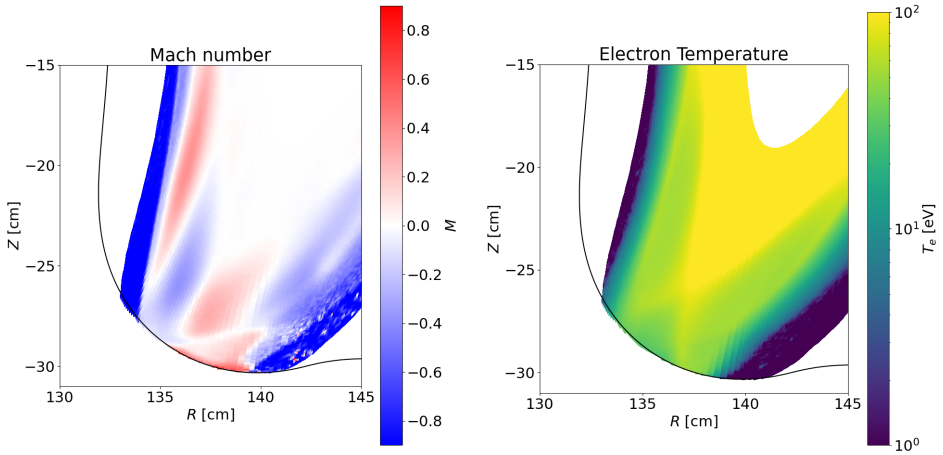

(a) EMC3-EIRENE $n_e = 2 \times 10^{13}$ cm^{-3} (b) EMC3-EIRENE $n_e = 2 \times 10^{13}$ cm^{-3}

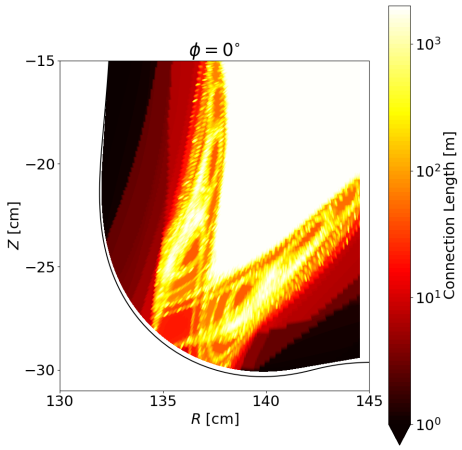

(c) FLARE reproduced from figure 4.13

Figure 5.5: Magnified poloidal cross sections near one of the strike points at the wall at $\phi = 0°$ for the QHS configuration. Plots (a) and (b) are of M and T_e, respectively, calculated with EMC3-EIRENE. Plot (c) shows the corresponding L_C calculated with FLARE in chapter 4.

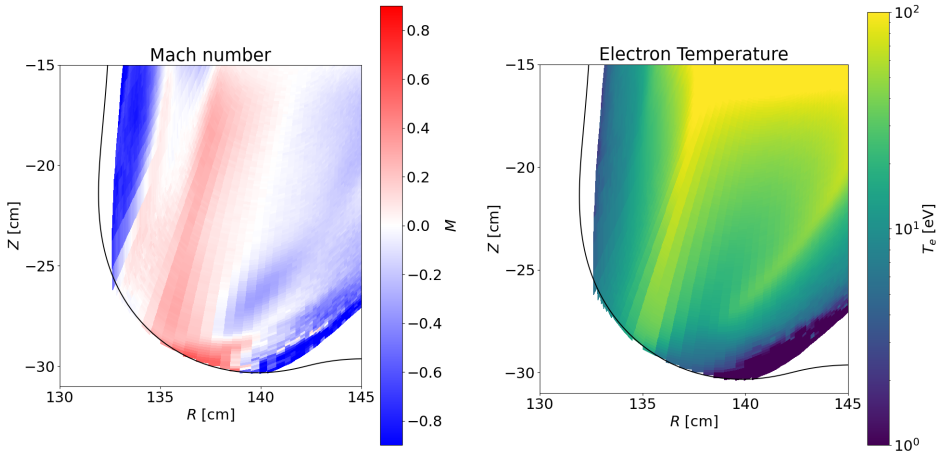

(a) EMC3-EIRENE $n_e = 2 \times 10^{13}$ cm^{-3} (b) EMC3-EIRENE $n_e = 20 \times 10^{13}$ cm^{-3}

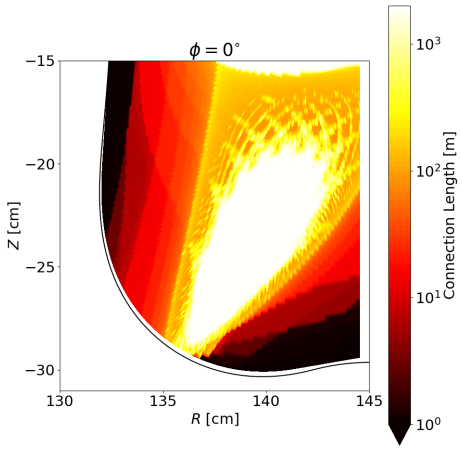

(c) FLARE reproduced from figure 4.13

Figure 5.6: Magnified poloidal cross sections near one of the strike points at the wall at $\phi = 0°$ for the large island configuration. Plots (a) and (b) are of M and T_e, respectively, calculated with EMC3-EIRENE. Plot (c) shows the corresponding L_C calculated with FLARE in chapter 4.

netic configurations and that the details of the strike line/footprint pattern convey which edge magnetic structures influenced the overall pattern. These field line following results combined with the EMC3-EIRENE target deposition and plasma profiles suggest that more attention must be considered to fully resolve how much L_C substructures observed in the chaotic edge region compete with anomalous diffusion to influence the details of the resilient strike line. Moreover, it remains to be seen if the details of the strike line need to be resolved further in the EMC3-EIRENE simulations. An open question also remains if a dedicated experiment will agree will resemble the field line following or EMC3-EIRENE results. Nevertheless, we will see in section 5.1.1 that there is still an overall resilient strike line feature present resulting from the provided calculation of the plasma transport shown in this section.

5.1.1 Wall Deposition Pattern for the QHS Configuration During a Scan of Upstream Density

To simulate the heat and particle flux deposition on the wall, the EMC3-EIRENE post-processing routine is performed and shown in figure 5.7. The top row and bottom row of figure 5.7 display the particle and heat load on the wall ($\Gamma_t,\ Q_t$) respectively for the first half-field period. As expected from the FLARE results which serve as a proxy for the heat and particle flux on the wall, the deposition pattern from low to high density is in the region of the resilient helical strike line and strongly resemble one another with respect to n_u. However, while these patterns are similar in location, increasing n_u changes the magnitude of Γ_t and Q_t deposited onto the wall. Namely, Γ_t is higher and Q_t is lower for $n_u = 20 \times 10^{13}$ cm^{-3} compared to $n_u = 2 \times 10^{13}$ cm^{-3}. This is more clearly shown in figure 5.10 discussed in section 5.1.2. The trend of Γ_t and Q_t corresponds with the change in behavior in the T_i and n_i profiles plotted in figures 5.2 and 5.3, respectively.

A comparison of the FLARE generated strike points with the heat flux in figure 5.8 is shown. The FLARE strike points are generated by following field lines inside the LCFS and imposing a FLARE diffusion of $d = 4.4 \times 10^{-7}$ m^2/m much like what was done

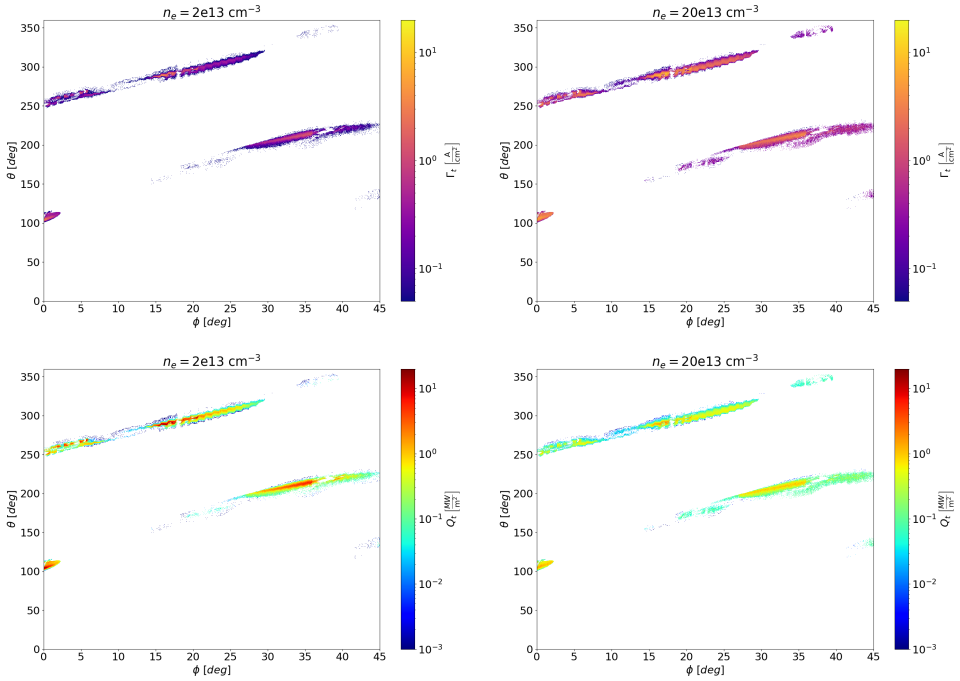

Figure 5.7: Particle flux deposition (top row) and heat flux deposition (bottom row) for $n_e = 2 \times 10^{13}$ cm^{-3} (left column) and $n_e = 20 \times 10^{13}$ cm^{-3} (right column).

in chapter 3 for modeling the CTH equilibria. The forward and backward points are superimposed in black $\times$ and gray $\circ$, respectively, in figure 5.8 (a) and (c). Overall, there is agreement between the main regions of EMC3-EIRENE calculated heat load and the FLARE generated strike points. The heat flux in this figure is from $n_u = 2 \times 10^{13}$ cm^{-3}. Figure 5.8 (b) and (c) magnify the upper region of plot (a) to assess if the peaked heat flux regions (orange ($\mathcal{O}(10$ MW/m^2)) to red ($\mathcal{O}(1$ MW/m^2))) coincide with the results from field line tracing. Similar to the heat flux deposition results in chapter 3, the different directions correspond to different regions of the peaked heat flux. This is the case between $12^\circ \leq \phi \leq 25^\circ$ at $\phi \sim 18^\circ$ where a gap in the heat load indicates a change in direction of the incident field line intersection with the wall. This feature was manifested similarly in CTH in chapter 3 where the separation of forward and backward strike points helped indicate if the plasma wall scenario was limited or diverted. These forward and backward regions on the deposition can be connected to the counter-streaming flow pattern shown in figures 5.4 and 5.5 (c).

The results of chapter 4 clearly distinguished for the QHS configuration which features of field line interaction with the wall are due to the 8/7 island chain or collimated flux tubes extending from these islands. This was shown in section 4.2 with figures 4.10 - 4.9. Furthermore, because the regions of anticipated deposition calculated with FLARE agree with what is generated with EMC3-EIRENE, this indicates that the magnetic structures identified in chapter 4 may be connected to the deposition seen in figures 5.7 and 5.8.

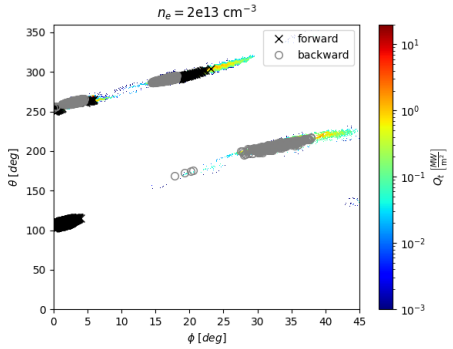

(a) FLARE strike points superimposed on full wall heat load

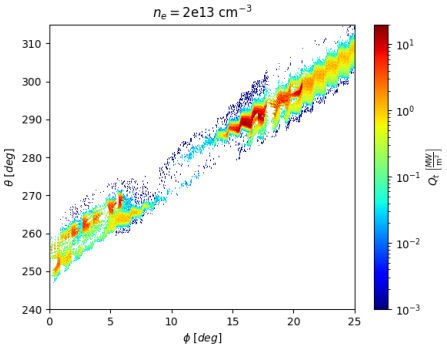

(b) magnified region of wall heat load

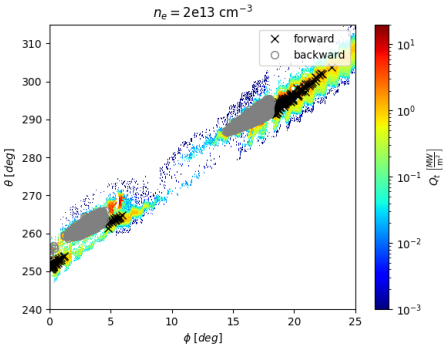

(c) magnified region of wall heat load with superimposed FLARE strike points

Figure 5.8: Comparison of FLARE strike points with EMC3-EIRENE post processed wall deposition for $n_u = 2 \times 10^{13}$ cm^{-3}. Plot (a) displays the entire simulated wall with the superimposed strike points, plot (b) shows a magnified region of the wall heat load without the superimposed strike points, and plot (c) is plot (b) but with the superimposed points.

Moreover, between $0° \leq \phi \leq 10°$, the different orange ($\mathcal{O}(1$ MW/m$^2)$) regions of high heat load also correspond to different localized regions of the strike points. While figure 5.8 corresponds to only $n_u = 2 \times 10^{13}$ cm^{-3}, the agreement between the deposition of the

two different n_u in figure 5.7 suggests that even as n_u varies, the FLARE strike points capture the peak regions of heat and particle flux across the varied n_u. These deposition patterns are also qualitatively similar to what is shown in figures 4.5 and 4.6 calculated with FLARE in chapter 4 showing the anticipated regions of heat and particle flux.

The results, combined with the field line tracing results of FLARE, show that the expected helical regions of heat and particle flux on the wall correspond with one another even when n_u is varied in EMC3-EIRENE. We next examine the SOL regime behavior based on the simulated downstream quantities as a function of n_u in the QHS configuration. This behavior will be connected with the trends of the peak particle and heat flux.

5.1.2 Examination of SOL Transport Behavior Trends for the QHS configuration

This section examines the downstream quantities of density and temperature as a function of n_u in order to assess if the SOL transitions from a low to high-recycling regime and if it eventually accesses detachment as described in section 2.1.3. The example given in section 2.1.3 describes the well-known ASDEX "rollover" illustrated in figure 2.7 [31]. In general, the "downstream" location refers to the target (the lofted wall) and this quantity is averaged over the target(s) in EMC3-EIRENE. Figure 5.9 plots (a) the downstream density n_d in blue, (b) the ratio n_d/n_u in orange, and (c) downstream electron and ion temperature $T_{\{e,i\}d}$ in green. The assumed error in figure 5.9 is between $20\% - 30\%$ which is discussed further in section 5.2. This is detailed in the context of power balance in the SOL simulated with EMC3-EIRENE.

Beginning with 5.9 (a) and (b), it is observed that n_d tends to increase roughly linearly with n_u until $n_u = 5 \times 10^{13}$ cm^{-3}. After this value of n_u, n_d/n_u then decreases in (b) while n_d in (a) plateaus with n_u. This is an indication of the transitioning out of low-recycling for densities $n_u < 5 \times 10^{13}$ cm^{-3}. This trend in n_d is accompanied with a marked decrease in $T_{\{e,i\}d} < 10\,\text{eV}$ at $n_u \geq 4 \times 10^{13}$ cm^{-3}. At this n_u, the temperature is $T_{\{e,i\}d} \sim 6\text{eV}$ and is well above the threshold for volumetric recombination and molecular

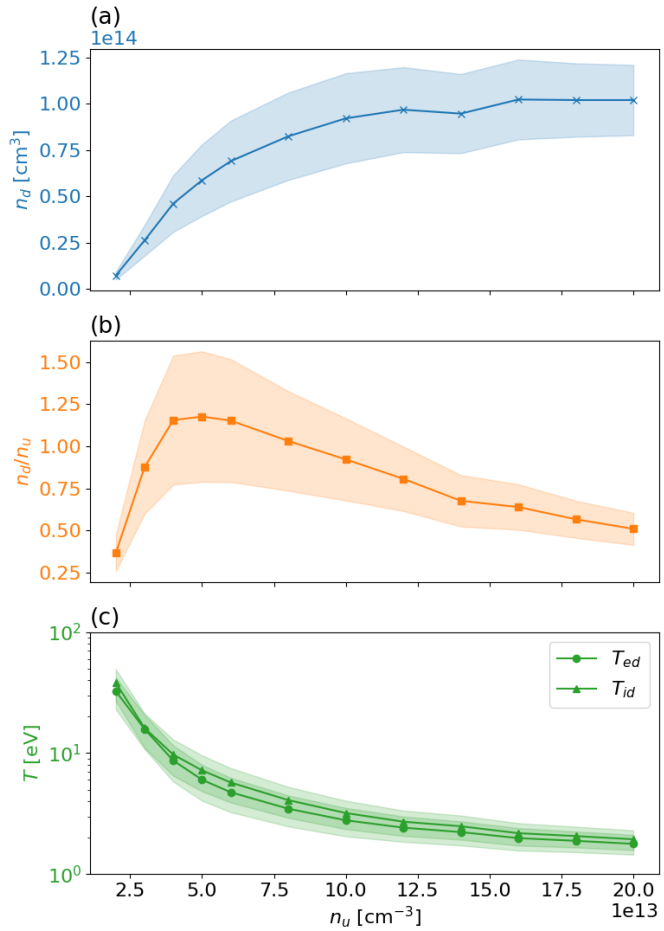

Figure 5.9: (a) Downstream density n_d in blue, (b) n_d/n_u in orange, and (c) downstream electron and ion temperatures $T_{\{e,i\}d}$ in green all as a function of n_u.

assisted recombination needed to detach the particle flux [44]. Moreover, the downstream density does not increase as $n_d \propto n_u^3$ meaning that high-recycling is not achieved. An indicator of achieving high-recycling is when $n_d \propto n_u^3$ as mentioned in chapter 2. While figure 5.9 (b) of n_d/n_u may resemble a "rollover" that indicates a SOL regime transition into detachment, it is n_d vs n_u that usually must exhibit this "rollover" as observed for tokamaks. It is seen in figure 5.9 (a) that n_d plateaus for $n_u \geq 10 \times 10^{13}$ cm^{-3} which is indicative of not reaching full detachment. While the temperature is observed to drop significantly, figure 5.9 (a) and (b) suggests that there is not enough build-up in n_d to trigger volumetric particle sourcing to access detachment of the particle flux from the

target (particle detachment). Reference [44] distinguishes between energy, momentum, and particle detachment in tokamaks. In this reference, energy detachment is linked with the trend in target heat flux, momentum detachment with target particle flux, and particle detachment with recombination events. Using this terminology, we proceed to link the downstream trends in figure 5.9 with the target heat and particle flux (Q_t, Γ_t respectively) to assess the mentioned detachment subcategories.

We examine the maximum Q_t and Γ_t as a function of n_u in figure 5.10. The maximum (a) Γ_t and (b) Q_t on the wall target are plotted as a function of all simulated upstream densities in 5.10. The implemented error bars are the same as in figure 5.9 to be described in section 5.2. The peak heat and particle flux values are taken from figure 5.7 in section 5.1.1. We note that the maximum values of heat and particle flux along the lofted wall vary between $\phi \in (15°, 18°)$ and corresponds poloidally to $\theta \sim 290°$ in figure 5.7. Figure 5.10 (a) shows that peak particle flux follows the downstream density trend. First, Γ_t increases approximately linearly until $n_u = 5 \times 10^{13}$ cm^{-3}. As Γ_t does not follow n_u^3, this is similar to earlier work in W7-X where it was found that the particle flux does not scale with n_u^3 and hence does not achieve high-recycling due to momentum loss from the presence of counter-streaming flows [45], [123]. After $n_u = 5 \times 10^{13}$ cm^{-3}, Γ_t is roughly constant at 15 A/cm^2 as n_u increases although we note a modest reduction. This slight reduction in Γ_t is not as pronounced as what is expected to reach momentum and particle detachment in tokamaks as described in reference [44]. The target heat flux, however, follows the downstream temperature trend. The reduction in Q_t coincides with T_{ed} decreasing to 1.78 ± 0.33 eV and suggests that the heat flux experiences detachment.

Because the simulations are of the lofted wall only and no other in-vessel divertor components are added (such as baffle structures), it is not expected that high recycling and particle flux detachment would be achieved in this HSX simulation study. Especially since there are no structures to help in the accumulation of neutral pressure for detachment which was described in section 2.1.3, the lofted wall as the only PFC makes this an "open" rather than "closed" divertor analysis. The modification toward a "closed" divertor con-

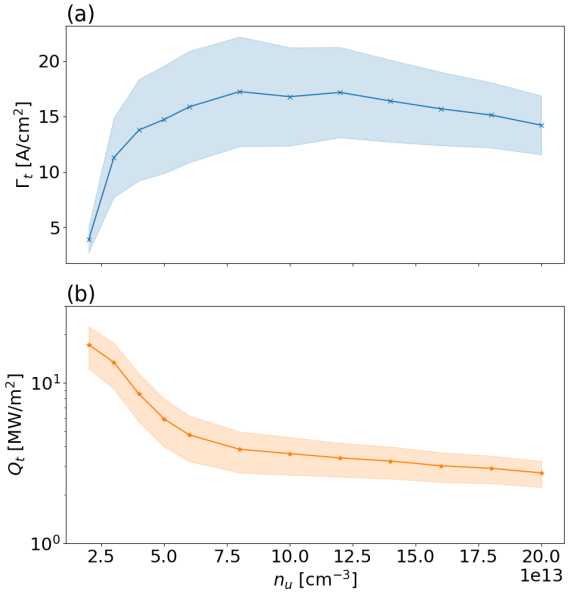

Figure 5.10: Maximum values of (a) Γ_t and (b) Q_t as a function of n_u. These values are taken from deposition shown in figure 5.7.

figuration in LHD was observed to improve neutral pressure by more than ten times when compared to "open" helical divertor operation [47], [124]. The "open" island divertor in W7-X, moreover, has been shown to exhibit low neutral pressures in the subdivertor region and hence causes issues with particle exhaust [35], [118]. Moreover, recent studies have shown that a "closed" divertor design for island-divertor like geometries shows a marked improvement in n_d for reaching detachment [125]. We also note that no impurities were added to the EMC3-EIRENE modeling in HSX. Inclusion of impurities would have added a contribution to the power balance (P_{IMP}) which is helpful for reaching detachment. This is because impurities introduce an additional radiator. Furthermore, as no molecular processes were included in the simulations, the recycled hydrogen species are released as purely atomic. This means that no molecular dissociation energy losses are included, which would likely increase the downstream power dissipation. Inclusion of impurities as well as molecular processes are areas of future work identified by this analysis.

The results in this section indicate that the QHS strike lines on the lofted wall accumulate heat and particle fluxes in HSX. The rise of n_i and decline of T_i in figures 5.2 and 5.3

as n_u increases for the QHS configuration suggest that the trends of n_d and $T_{\{e,i\},d}$ can be used as an indicator of the SOL regime transition. This analysis strongly suggests that a high-recycling regime was not reached. Other open stellarator divertor setups have also not observed high-recycling. In these configurations, this was connected to counter-streaming flows in the edge as a momentum loss mechanism which prevents access to high-recycling. While the M structure in the QHS configuration discussed earlier in this chapter show the presence of counter-streaming flows, further analysis is necessary to assess if this plays in role in not reaching high-recycling here. The dissipated heat flux, however, demonstrates that energy detachment is achieved while particle and momentum detachment are not. An improvement in the grid is needed for a deeper analysis of full detachment especially with respect to the details of the target deposition and for comparison across various magnetic configurations. Grid improvement would help establish the parameters or other needed physical structures needed to achieve detachment in HSX with the lofted wall. Section 5.2 next details the grid misalignment issues which manifest in power losses in the EMC3-EIRENE simulations.

5.2 Power Loss Analysis for EMC3-EIRENE Grid Improvement

This section examines the power losses associated with EMC3-EIRENE field-aligned grids. The amount of power loss from numerical errors in these simulations is important to track. If a significant amount of power is lost in the simulation, this influences the plasma transport calculation as the simulation reaches a self-consistent solution of the plasma parameters of, for example, the temperature and density in the plasma edge region. This in turn also impacts the post-processed deposition of heat and particle flux onto the target or PFC since EMC3-EIRENE takes into account power losses as an input for the deposition calculation. To examine these losses, we analyze how the input power at a given topological toroidal surface is balanced by the power output via:

1. heat deposited to the target(s) (P_T)

2. radiation due to plasma-neutral interactions (P_{NG}). The atomic and molecular processes included in EIRENE for the simulations in this chapter are tabulated in table 5.2.

3. loss due to radial transport across field lines from perpendicular diffusion at the radial boundary of the simulation domain (P_{RL}) and transport along field lines due to misalignments of the computational grid at zone boundaries (P_{SL}). The latter manifests from non-overlap of mapping surfaces from following along the field lines and is discussed at length in this section.

4. radiation due to interactions with impurities (P_{IMP}). As no impurities are included in these simulations, this power term is ignored.

The power loss due to grid misalignments is tracked in EMC3-EIRENE and is one of the contributions to the power output. It is also noted that these power losses are also influenced by the chosen initial conditions (such as input power and imposed upstream densities), however, we keep all initial conditions consistent except in variation of the upstream density n_u. We describe below the details of the grid and how power losses caused by these misalignments, and more specifically mapping surfaces, arise.

reaction	reaction type
$e + H_2 \rightarrow 2e + H_2^+$	ionization
$e + H_2 \rightarrow e + H + H$	dissociation
$e + H_2 \rightarrow 2e + H + H^+$	ionizing dissociation
$e + H_2^+ \rightarrow H + H$	recombining dissociation
$e + H_2^+ \rightarrow e + H + H^+$	dissociation
$H + e \rightarrow H^+ + 2e$	ionization
$H + H^+ \rightarrow H^+ + H$	charge exchange
$e + H^+ \rightarrow H + h\nu$	recombination

Table 5.2: Atomic and molecular reactions included in EIRENE for the simulations in this chapter.

Power loss due to grid misalignments occur at zone boundaries of the split simulation domain. Sections 2.3 and 5.1 describe splitting the simulated toroidal domain into

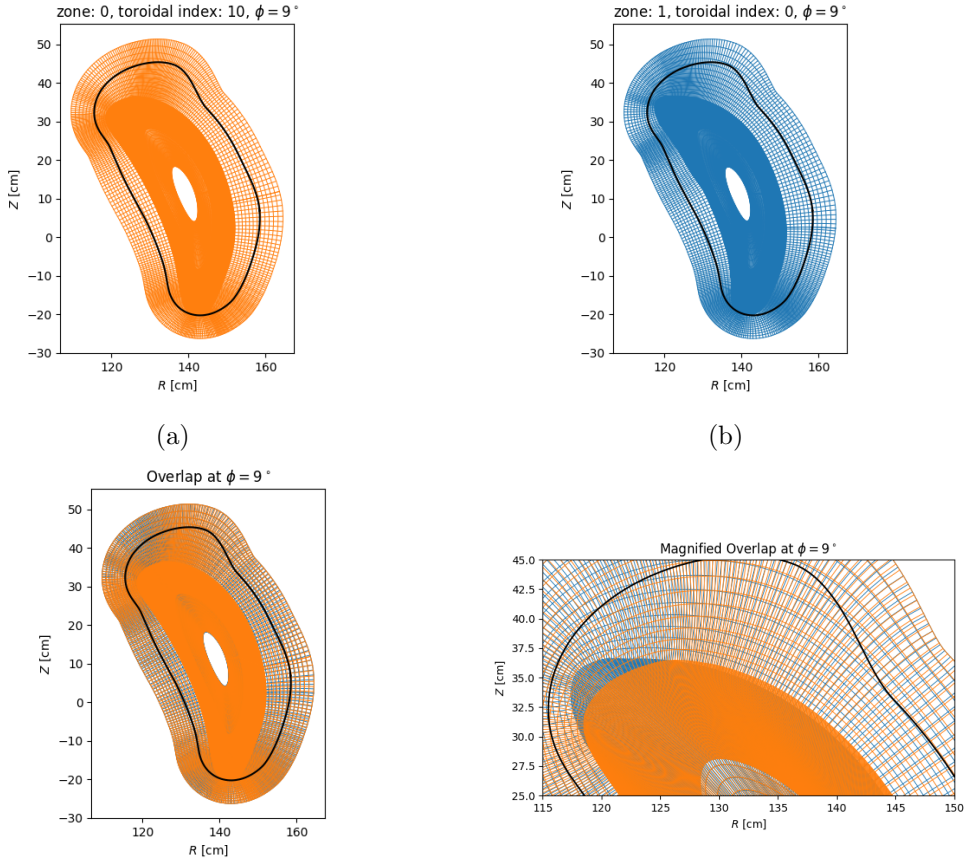

Figure 5.11: Example of zone overlap at $\phi = 9°$. Zone 0 and zone 1 span $\phi \in [0°, 9°]$ and $\phi \in [9°, 18°]$ respectively. Each zone has a toroidal resolution of 10 cells and we show zone 0 at toroidal index 10 (a) in orange and zone 1 at toroidal index 0 (b) in blue and their overlap at $\phi = 9°$ (c). A magnification of (c) is shown in (d). The lofted wall is superimposed in black. The region with greater cell density indicates the plasma domain while the region with less cell density represents the neutral domain.

multiple toroidal zones to better represent the complex shaping geometry and magnetic structure present in some equilibria. Despite this, grid misalignments always occur at zone boundaries as an error resulting from interpolation from one zone to the next. This means that, for example, plasma cells of one zone do not map onto the next zone's plasma domain. Mapping loss also occurs at up-down symmetric zone boundaries which will be described in the following paragraph. We first describe mapping loss at the overlapping interface of 2 different zones. An example illustrating the base mesh overlap of 2 different zones at their boundary is shown in figure 5.11 at $\phi = 9°$ from the QHS grid where the grid resolution is noted in table 5.1. Figure 5.11 (a) plots the first zone (zone 0) at its final toroidal index (10) in orange and figure 5.11 plots the second zone (zone 1) at its first toroidal index (0) in blue. Their overlap is shown in figure 5.11 (c) and magnified for a smaller poloidal region in (d). Cells from zone 0 and zone 1 are indicated in orange and blue, respectively, where the plasma region of each zone has a higher density of cells while the neutral domain is less dense with cells. By construction, cells within the neutral domain are not affected by the described mapping surface loss. The regions in plot (d) where the plasma cells do not overlap between zone 0 and 1 are where mapping losses are most likely to occur. Grid construction to reduce mapping losses is challenging, and attempting to expand the plasma domain to reduce such losses can increase flux errors and/or introduce irregularly shaped cells due the complexity in magnetic structure in the edge. We call the power lost in the simulation from this lack of overlap a mapping surface power loss P_{SL}. In general, such losses are inevitable and typically a loss of $< 5\%$ is deemed acceptable. For higher power loss, it is necessary to investigate how much the modeling outcome is affected by this loss. We will carefully consider the power loss and prescribe an uncertainty range to the modeling results shown in the previous sections.

Mapping loss at a zone boundary can also occur when the poloidal cross section is supposed to be up-down symmetric and is not. This occurs, for example, at the zone boundary at $\phi = 0°$ in the first zone of the QHS grid because grid generation is started at $\phi = 4.5°$. This type of grid misalignment is unavoidable and occurs even if the simulation

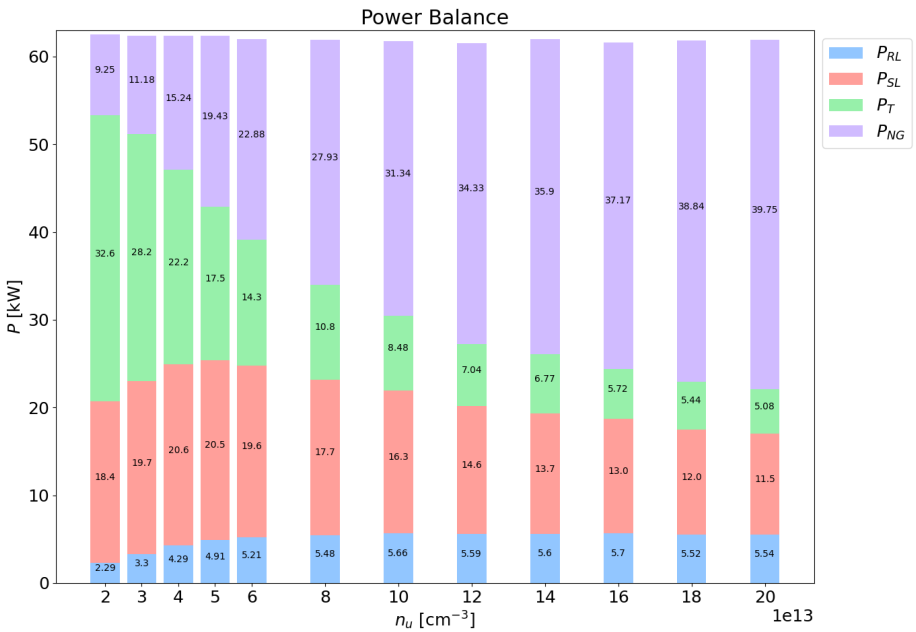

Figure 5.12: SOL power balance as a function of n_u for the large island configuration. The total input power was set to 500 kW corresponding to 62.5 kW for the simulation domain (an eighth of HSX). Plotted is the the power radiated from neutral gas interactions (P_{NG} light purple), power deposited onto the target (P_T light green), and power lost due to perpendicular transport (P_{RL} light blue) and mapping surfaces from parallel transport (P_{SL} coral).

domain would not be split into multiple zones. In the case where grid generation is started at an up-down symmetric cross section, for example $\phi = 0°$, the FLARE mesh generation routine which traces the field lines to the half-period would not result in an up-down symmetric grid at the $\phi = 45°$ zone boundary. Furthermore, the mapped losses would be significant in this one-zone scenario since splitting the domain into multiple zones aids with reducing mapping loss. In general, the grid is only susceptible to mapping losses at zone boundaries, such as what is shown in figure 5.11. P_{SL} from these mapping surface mechanisms is tracked in EMC3-EIRENE and is reported as a power term to the target or PFC in addition to P_T which reaches the target. This is important to note for the EMC3-EIRENE post-processing deposition routine discussed later which takes P_{SL} and P_T as inputs for the target deposition calculation. In this section, we treat P_{SL} separately from P_T.

$n_e \times 10^{13}$ [cm^{-3}]	P_{SL}/P_T	P_{SL}/P_{Total}
2	0.57	0.29
8	1.65	0.29
20	2.25	0.19

Table 5.3: Power lost to surface mapping P_{SL} compared to power to target P_T and total power P_{Total}.

Examining the power losses and the simulation's overall power balance requires a converged EMC3-EIRENE solution. Because of this, tracking such losses for grid improvement can become computationally time consuming in terms of both reaching simulation convergence and adding manual grid adjustments to reduce power losses. For the density scan of the QHS configuration performed in the last section, we show the power balance in figure 5.12. Recalling that the input power for the simulation domain is 62.5 kW, figure 5.12 plots the power that is radiated due to interactions with neutral gas P_{NG} (light purple), power reaching the target P_T (light green), power lost to mapping surfaces P_{SL} (coral), and power lost radially from cross-field transport P_{RL} (light blue). In the center of each color block is the power in kW corresponding to the legend for the simulated n_u. Overall, as the fixed n_u increases, P_{NG} tends to increase while P_T decreases. This is expected as

T_i in figure 5.3 is markedly decreased at high n_u compared to the lowest simulated fixed n_u and coincides with more power radiated due to neutral gas interactions. While this trend persists, we also note the behavior of P_{SL} with increasing n_u and turn our attention to table 5.3. Compared to the total power P_{Total}, P_{SL} tends to decrease as seen in coral in figure 5.12 and in the third column of table 5.3. As mentioned in the beginning of this section, however, P_{SL} is taken as an input for the target deposition post-processing routine along with P_T. Thus, we must also compare P_{SL}/P_T. While P_T noticeably decreases in figure 5.12, the change in P_{SL}/P_T as n_u increases conveys that P_{SL} is the dominant flux contribution that will go through the target compared to P_T for $n_u \geq 5 \times 10^{13}$ cm^{-3}. As a significant contribution to the overall power balance with P_{SL} comprising $20\% - 30\%$ of P_{Total}, this introduces a level of uncertainty for the plasma transport output from EMC3-EIRENE and suggests that further grid refinement is necessary. This error was employed in figures 5.9 and 5.10 in order to describe the physics results earlier in this chapter. Nevertheless, the trends of the downstream quantities accompanied with increasing P_{NG} with n_u confirm assessment of a low-recycling regime followed by a reduction in target temperature $T_{\{e,i\}d}$ approximately from 40 eV to $\sim$ 2 eV just with the HSX lofted wall seen in figure 5.9. This confirmation of the downstream trends is supported by table 5.3 which shows that P_{SL}/P_{Total} decreases from 0.29 at $n_e = 2 \times 10^{13}$ cm^{-3} to 0.19 at $n_e = 20 \times 10^{13}$ cm^{-3}.

5.2.1 How Grid Power Loss Impacts Simulation of Target Deposition

To further assess the power loss associated with the grid misalignment, we examine the result of the EMC3-EIRENE's post-processing deposition routine on the PFC. The overall deposition from this calculation was shown in section 5.1.1 with figures 5.7 and 5.8. In particular, we must compare the input flux to the target versus the flux that is actually deposited onto the target from this calculation. This is necessary in order to assess how much mapping losses from grid misalignments may be

1. underestimating the values of the target heat and particle deposition

2. altering the location of target heat and particle deposition

This post-processing routine takes in P_T and P_{SL} (both from the converged EMC3-EIRENE solution) as well as surface recombination at the target as input to calculate the heat and particle deposition on the target. Surface recombination is calculated from $\epsilon\Gamma_T$ where Γ_T is the particle flux to the target and $\epsilon = 15.6\,\text{eV}$ where 13.6 eV is for hydrogen recombination and additional 2 eV of molecular hydrogen recombination. We denote the power mapped onto the target (or deposited to the target) from P_T and P_{SL} as $P_{T,depo}$ and $P_{SL,depo}$, respectively. P_{SL} can still be deposited onto the target in this routine since the deposition simulation will track particles until they reach a target, regardless if this particle contributed to P_T or P_{SL}. A particle from P_{SL} which is not mapped onto the next toroidal domain is followed in post-processing until reaching a target element. The maximum number of cells in the forward and backward directions to map field lines onto the target(s) is set by the code's NT_S parameter. If the particle is not deposited onto the target, it is lost in the simulation. Otherwise, it contributes to $P_{SL,depo}$. Both scenarios will be described in this section. Before this, we compare the ratios of $P_{T,depo}/P_T$ and $P_{SL,depo}/P_{SL}$ in table 5.4 for only 2 upstream densities (2×10^{13} cm^{-3} and 8×10^{13} cm^{-3}). We will return to the impact of the parameter NT_S noted in the first column entry of table 5.4 after discussing figures 5.13 and 5.14.

NT_S	$n_e \times 10^{13}$ [cm^{-3}]	$P_{T,depo}/P_T$	$P_{SL,depo}/P_{SL}$
3,3	2	1	0.35
3,3	8	1	0.11
100,100	2	1	0.84
100,100	8	1	0.81

Table 5.4: Ratio of flux deposited onto target vs through target expressed for target power P_T and power lost to surface mapping P_{SL}. Increasing the parameter NT_S improves the overall power loss in the simulation seen in ratio $P_{SL,depo}/P_{SL}$.

We consider the first two rows of table 5.4. The ratios of $P_{T,depo}/P_T$ and $P_{SL,depo}/P_{SL}$ show that 35% and 11% of P_{SL} is deposited onto the target for $n_e = 2\times10^{13}$ cm^{-3} and 8×10^{13} cm^{-3}, respectively. The remaining power not accounted for is power that is not deposited onto the target and is lost in the simulation. To visualize the regions of P_{SL}

lost in the simulation or deposited onto the target, we turn our attention to figures 5.13 and 5.14. Figure 5.13 displays P_{SL} which does not make it to the target while figure 5.14 shows P_{SL} which reaches the target ($P_{SL,depo}$).

Figure 5.13 shows the overlap of base meshes at zone boundary at $\phi = 18°$ (one zone in black and the other zone in red). Plots (a) and (b) are plots magnifying power loss from mapping surfaces for the two different set values of upstream n_e. Like figure 5.11, the denser region of grid cells are each zone's respective plasma domain while the less dense region of larger cells correspond to the neutral domain. The magnified region of plots (a) and (b) of figure 5.13 shows the power loss due to mapping surfaces which does not get deposited onto the target since this region of non-white cells from P_{SL} is inside the lofted wall boundary (thick black curve). Plot (c) of figure 5.13 overlays the L_C contour map at $\phi = 18°$ calculated with FLARE in chapter 4 onto the zone overlap region. We see that the region of mapped loss plotted in figure 5.13 (a) and (b) shows that a high L_C flux tube (yellow $L_C \sim \mathcal{O}(10^3$ m)) is not cut off by this mapped loss. Furthermore, the FLARE results of chapter 4 indicate that this region of mapped loss in figure 5.13 (b) and (c) does not coincide with the high L_C flux tube(s) that interact with the wall to create the helical strike line. Furthermore, the colorbar scale in figure 5.13 (a) and (b) show that that this mapped loss is marginal ($\leq \mathcal{O}(10\,\mathrm{W})$) (and are qualitatively similar for the different set values of n_u) compared to the input power of the simulation and an order of magnitude lower than the mapped loss which reaches the target $P_{SL,depo}$ discussed in the next paragraph. The magnitude of power lost in this example combined with the fact that this particular region in the open chaotic layer is not a major contribution to the overall anticipated heat flux strike line. This shows that while P_{SL} is still lost in the simulation, this does not significantly alter the location of the calculated EMC3-EIRENE deposition regions in figures 5.7 and 5.8.

On the other hand, figure 5.14 is an example of $P_{SL,depo}$. Figure 5.14 is at the simulation boundary of $\phi = 0°$ and is a magnification of the region $Z > 0$ where the lofted wall is again plotted as the thick black curve. To demonstrate that the grid at $\phi = 0°$ is not up-down

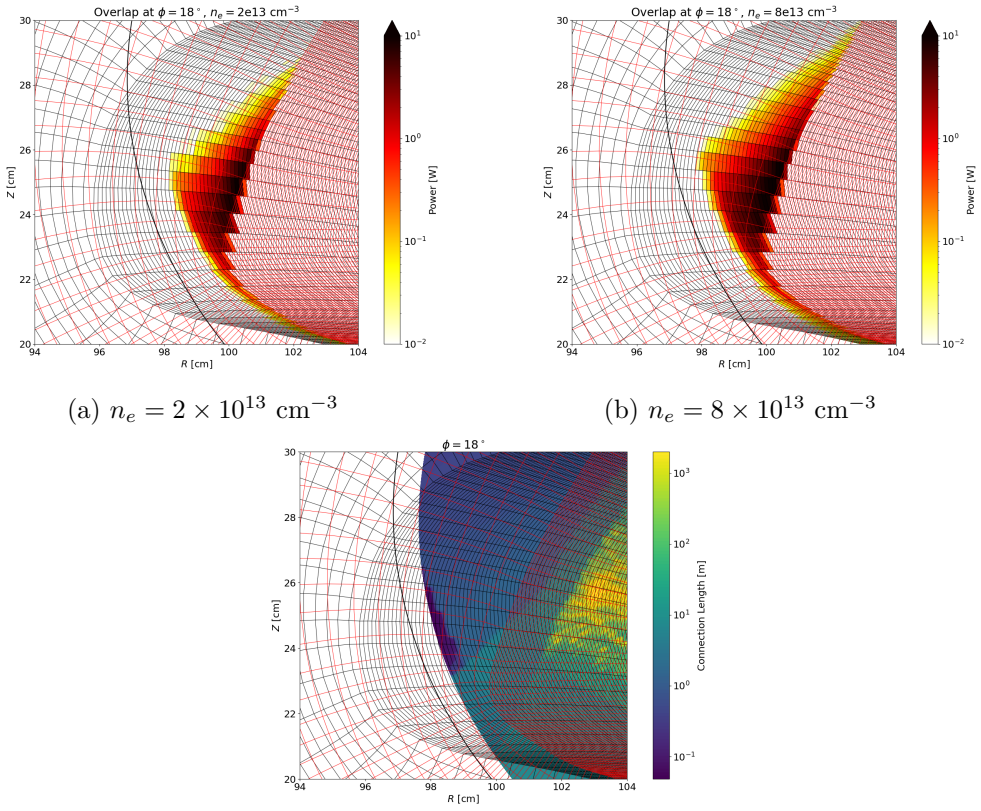

(a) $n_e = 2 \times 10^{13}$ cm^{-3}

(b) $n_e = 8 \times 10^{13}$ cm^{-3}

(c) Superimposed FLARE L_C

Figure 5.13: Zone overlap at $\phi = 18°$ of the base meshes (one zone is red and the other is black). Plasma cells carrying P_{SL} not mapped onto the target are shown for (a) $n_e = 2 \times 10^{13}$ cm^{-3} and (b) [$n_e = 8 \times 10^{13}$ cm^{-3} where the color inside of the cells correspond to the P_{SL} color bar. Plot (c) overlays the FLARE calculated L_C contour map from chapter 4 with the corresponding zone overlap region. The thick black curve in all plots is the lofted wall.

symmetric, figure 5.14 (d) superimposes the grid cells at $Z < 0$ as red cells on top of the black cells which correspond to the actual grid at this location. In addition to the mapping misalignment, figure 5.14 shows that the cells with P_{SL} are outside the wall at this toroidal location. These cells which carry P_{SL} are actually within the wall boundary at the next toroidal index. This can occur because plasma cells near the target can sometimes appear inside or outside the target/PFC boundary during field line mapping routine which tags cells as part of the neutral or plasma domain. The resulting P_{SL} at this location in the vicinity of target is deposited onto the target. Figure 5.14 (a) and (b) display the plasma cells with P_{SL} for $n_e = 2 \times 10^{13}$ cm^{-3} and 8×10^{13} cm^{-3}, respectively. The plasma cells which extend toward the wall in this region correspond topologically with the high L_C flux tubes that intersect the lofted wall and contribute to the helical strike line produced in the FLARE analysis in chapter 4. Because this mapping misalignment occurs, however, the power carried via these flux tubes is considered $P_{SL,depo}$ rather than $P_{T,depo}$. This type of mapping loss which becomes $P_{SL,depo}$ is expected in EMC3-EIRENE and is preferential to the scenario depicted in figure 5.13 since $P_{SL,depo}$ helps more accurately capture the heat and particle load to the target. We note that there are many more regions with mapped losses at the zone boundaries which accumulate and contribute to the overall loss in $P_{SL,depo}/P_{SL}$.

The first column in table 5.4 shows the impact of varying NT_S on the overall grid power loss. These quantities are compared for 2 choices of the numerical parameter NT_S. This parameter sets the maximum number of cells in the forward and backward directions to map field lines onto the target(s). A large value of NT_S is particularly beneficial for cells that are tangential to the target, however, it should be noted that this value should be set based on the grid's n_t and field lines L_C in the edge region near the target. As a computational exercise, we compare the code's default NT_S parameter value of $(3, 3)$ with an increased value of $(100, 100)$ to investigate the sensitivity of the mapping losses. This is listed in the first column in table 5.4. The first column demonstrates that by increasing NT_S, the $P_{SL,depo}/P_{SL}$ markedly increases for these fixed upstream density

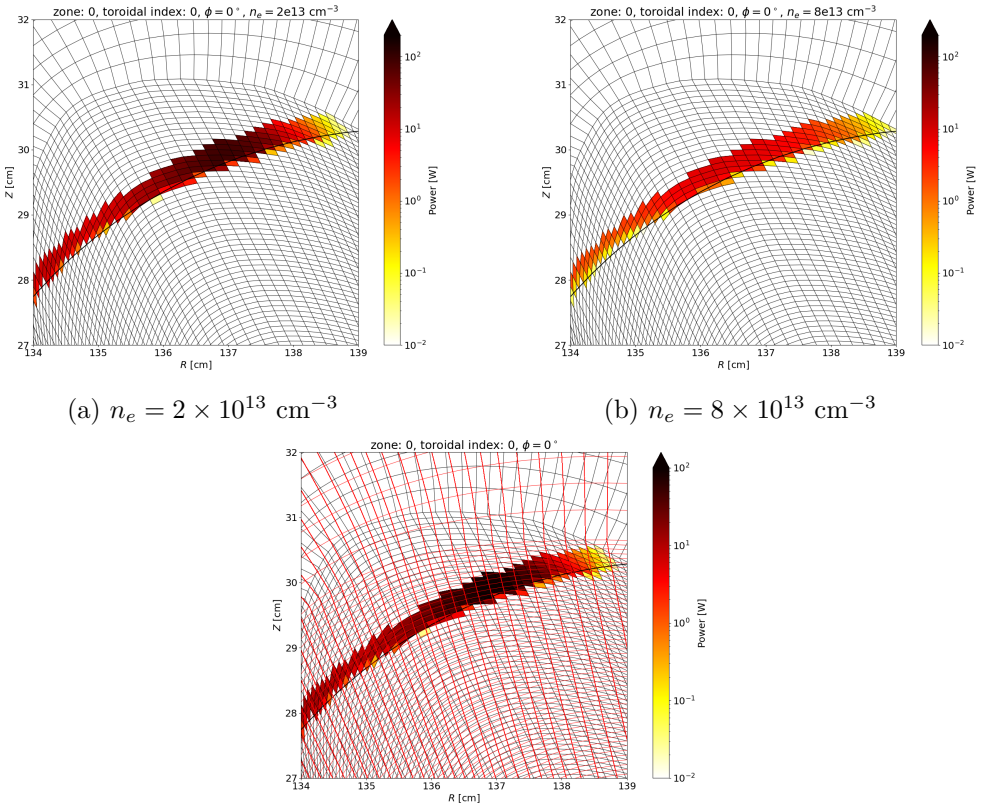

(a) $n_e = 2 \times 10^{13}$ cm^{-3}

(b) $n_e = 8 \times 10^{13}$ cm^{-3}

(c) Not up-down symmetric

Figure 5.14: Base mesh at $\phi = 0°$ at the simulation domain boundary magnified in one region near the lofted wall plotted as the thick black curve. The mapped losses are shown for (a) $n_e = 2 \times 10^{13}$ cm^{-3} and (b) $n_e = 20 \times 10^{13}$ cm^{-3}. In plot (c), the superimposed red cells correspond to the cells mirrored to the positive Z region while the black cells are the actual grid cells in this magnified region. In this example, P_{SL} does become mapped onto the target $P_{SL,depo}$.

values: $> 80\%$ of P_{SL} is deposited onto the target compared to the previous 35% and 11% for 2×10^{13} cm^{-3} and 8×10^{13} cm^{-3}, respectively. The impact of increasing NT_S is visualized on the target in figures 5.15 and 5.16 in section 5.2.2. We note that careful consideration of this set parameter value should be taken into account for future analysis.

5.2.2 Overall Comparison of EMC3 and FLARE Deposition for the QHS and Large Island Configurations

In this section, we study how the parameter NT_S impacts the target heat and particle fluxes and and compare with the strike line structure obtained from field line tracing. The wall deposition outcome from increasing NT_S for the QHS configuration is shown in figure 5.15. The heat flux on the wall for (a) $n_e = 2 \times 10^{13}$ cm^{-3} and (c) $n_e = 8 \times 10^{13}$ cm^{-3} are shown in the left column of the figure while the right column superimposes FLARE generated strike points with a diffusion value of 4.4×10^{-5} m^2/m in (b) and (d). Examining the left column first, we note that the helical regions of peaked heat flux observed in figure 5.7 (with NT_S $= (3, 3)$) is recovered in both density cases, however, an additional region of $\mathcal{O}(10^{-1}$ MW/m$^2)$ (light green to light blue) emerges between $20° \leq \phi \leq 45°$. While the heat flux in this area is a few orders of magnitude smaller than the peaked helical heat flux regions, it is important to determine whether this region is artificial. For further comparison, the right column of figure 5.15 superimposes FLARE generated strike points. Similar to the calculated strike points shown in previous sections, these field lines are followed in both forward and backward directions (plotted in black $\times$ and gray $\circ$ respectively) but now with an increased diffusion value of 4.4×10^{-5} m^2/m (2 orders of magnitude higher than the strike points shown in figure 5.8). By artificially increasing this diffusion value, there are more field lines which strike the wall in comparison with figure 5.8. These strike points from field line following are now extended helically further and correspond to the helical heat flux regions from EMC3-EIRENE. Because these strike points extend helically further, a region between $20° \leq \phi \leq 45°$ and $100° \leq \theta \leq 120°$ is present in figure 5.8. This can be interpreted as an extension of the up-down symmetric

branch of middle strike points from the next half-field period. While it is not expected that the results from two different codes will completely agree, the additional heat flux deposition between $20° \leq \phi \leq 45°$ and $100° \leq \theta \leq 120°$ could correspond the field line behavior of the newly generated strike points. Due to the extent of non-overlap between FLARE and EMC3-EIRENE, however, numerical inconsistencies could still be impacting the interpretation of this region. Before comparing this region further with the results of chapter 4 through figure 5.17, the deposition results for the large island configuration shown in figure 5.16 is discussed next.

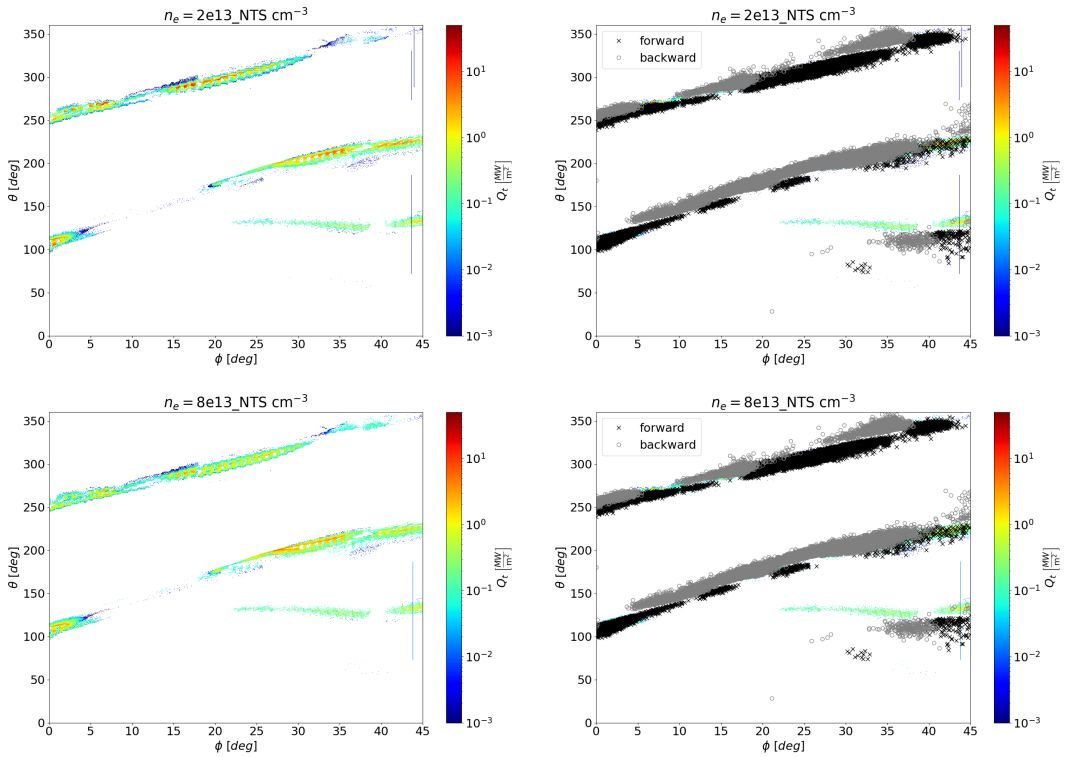

Figure 5.15: Left column plots the heat flux on the wall for (a) $n_e = 2 \times 10^{13}$ cm^{-3} and (c) $n_e = 8 \times 10^{13}$ cm^{-3} both with NT_S= $(100, 100)$. Right column superimposes the FLARE generated strike points with a diffusion value of 4.4×10^{-5} m^2/m in (b) and (d).

Figure 5.16 shows the calculated wall deposition for the large island configuration for the simulated densities of 2×10^{13} cm^{-3} and 3×10^{13} cm^{-3}. Details regarding the power loss associated with the large island grid can be found in section A.1 which is presented in a similar manner as section 5.2. The calculated wall deposition with NT_S

$= (3, 3)$ is also shown in section A.1. The deposition shown in figure 5.16 corresponds with NT_S $= (100, 100)$. The right column of this figure superimposes the FLARE strike points for the large island case with a diffusion value of 4.4×10^{-5} m^2/m like figure 5.15. As expected, there is overlap between the FLARE strike points and the deposition calculated with EMC3-EIRENE. Furthermore, it is noted in figure 5.15 that the region of flux between $20° \leq \phi \leq 45°$ and $100° \leq \theta \leq 120°$ previously described in figure 5.15 is also visible in the large island case's wall deposition. Additionally, the FLARE strike points for QHS and large island with increased diffusion resemble each other as expected from the results presented in chapter 4. The overall helical Q_t deposition pattern qualitatively agree between both magnetic configurations.

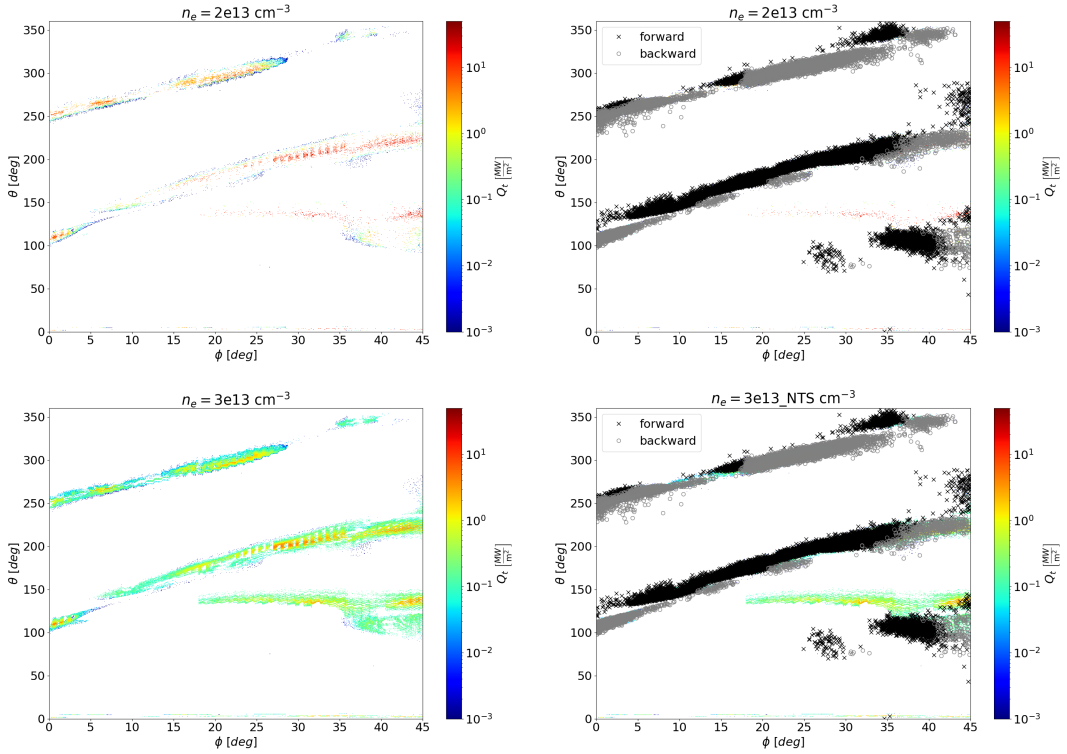

Figure 5.16: Heat flux deposition on wall for large island configuration with NT_S$= (100, 100)$. Left column plots Q_t while the right column superimposes the FLARE generated strike points on the heat flux map.

Turning our attention back to the region $20° \leq \phi \leq 45°$ and $100° \leq \theta \leq 120°$ on the heat flux pattern for both QHS and large island, we compare this region with figures 4.5

and 4.6 from chapter 4 which is reproduced below as figure 5.17. In this figure, the area between $35° \leq \phi \leq 45°$ and $100° \leq \theta \leq 120°$ is circled in black for added clarity in this discussion. The circled region contains short $L_C \sim \mathcal{O}(10\,\text{m})$ (orange) in plots (a) and (b) but with $\min(\delta_N) \sim \mathcal{O}(10^{-2}\,\text{m})$ (light pink-white) in plots (c) and (d). This indicates that there may be heat deposited on the target via flux tubes with short L_C and low $\min(\delta_N)$. The inclusion of the FLARE diffusive strike points from figures 5.15 and 5.16 along with the radial connection plots in figure 5.17 (c) and (d) strongly suggest that increasing NT_S captures this additional region of heat flux. Moreover, this extra heat flux region clearly demonstrates the location of where the increased P_{SL} deposited on the target reported in table 5.4 ends up on the target.

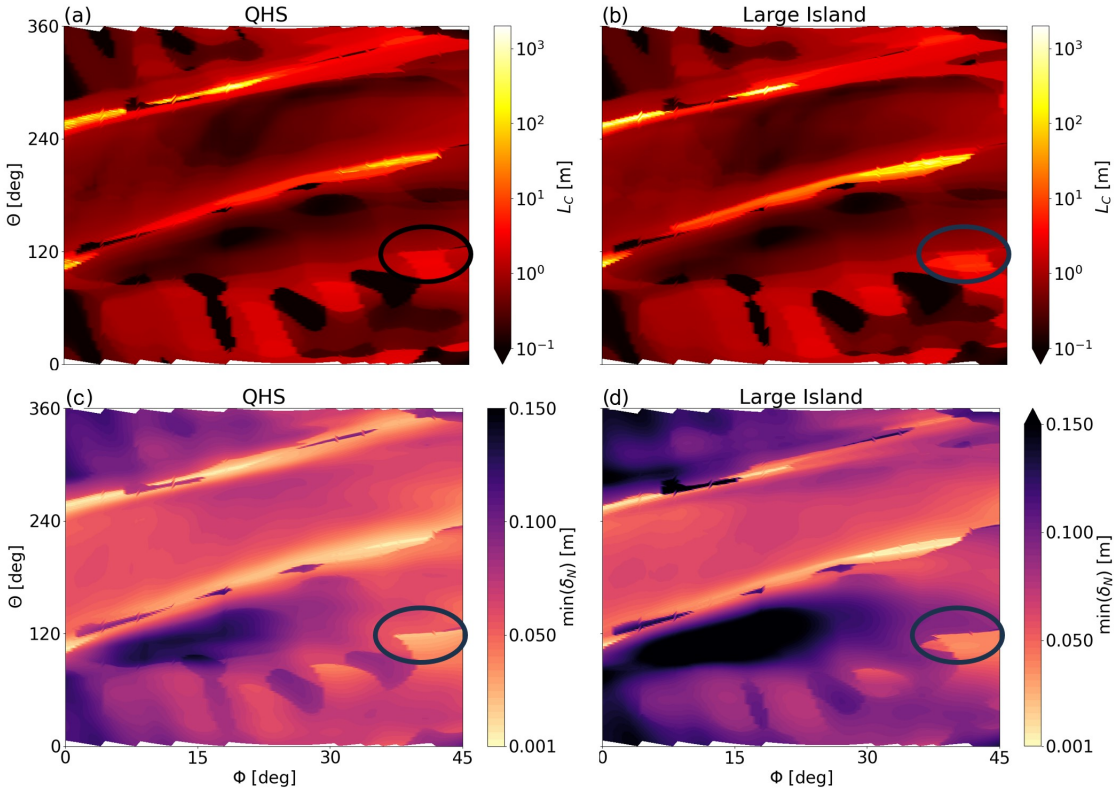

Figure 5.17: FLARE generated L_C ((a) and (b)) and $\min(\delta_N)$ ((c) and (d)) for the QHS ((a) and (c)) and large island ((b) and (d)) configurations reproduced from chapter 4. The circled region is for comparison with figures 5.15 and 5.16.

While this may provide some physical explanation of some extent of the flux reaching the target, discrepancies within this $20° \leq \phi \leq 45°$ and $100° \leq \theta \leq 120°$ still persist. This

could be due to increasing the NT_S parameter since this quantity increases the maximum number of cells which field lines are mapped onto the target. Furthermore, grid resolution such as the toroidal resolution or even the number of zones to split the simulation domain could be increased more for further assessment of the deposition and for overall power loss analysis.

5.3 Summary

Section 5.2 demonstrates that the mapping losses do not significantly alter the deposition pattern location. Furthermore, table 5.4 shows that nearly all of P_T gets deposited onto the target and, after the improvement seen with increasing NT_S, the majority of P_{SL} also gets deposited onto the target. While it is not ideal that P_{SL} becomes the main contributor to flux deposited onto the target as n_u increases, it remains that the deposition location is largely unchanged and qualitatively agrees with the results of chapter 4 and section 5.1. Moreover, even the extra regions appearing in the modified deposition calculation in figures 5.15 and 5.16 are also reproduced in the FLARE generated strike points with increased diffusion and in the radial connection in 5.17 (c) and (d). Thus, the analysis indicates that it is most likely that Q_t and Γ_t are under-calculated on the wall.

The overall uncertainty of $20\% - 30\%$ introduced by the power loss still show that the general trends of the SOL behavior examined in section 5.1.2 coincide with the power balance behavior. Specifically, the increase in P_{NG} with n_u agrees with the n_d behavior at the target. This is similarly observed in the agreement between the trends of P_T and $T_{\{e,i\}d}$ which suggest that the heat flux detaches. The simulated downstream density as a function of upstream density n_u along with the peak particle flux Γ_t behavior indicated that the particle flux remains attached and never reaches a high-recycling regime. This lack of high-recycling has been observed in other stellarator devices and is attributed to the upstream momentum losses due to counter streaming flows in the open chaotic layer. Moreover, as the M profile for the QHS configuration shows the counter-streaming flow pattern follows the 8/7 island chain rather than the chaotic substructures identified in

chapter 4, it remains to be seen if these flows prevent access to a high-recycling regime. This may require improved EMC3-EIRENE grid resolution of the open chaotic layer in the QHS configuration. The work in this chapter has shown that further EMC3-EIRENE grid improvements must be made in order to more accurately simulate the heat and particle flux deposition values and overall plasma edge behavior for assessing divertor detachment. Specifically, attention to numerical resolution is required and, for example, further reduction of P_{SL}/P_{Total} could be assessed through a deeper convergence study of lost power for a few representative n_u values. Moreover, modeling this behavior is necessary to facilitate future mechanical design efforts for NRDs.

It should be noted that the QHS grid supplied for this chapter was also used in reference [119] where an additional method was employed to improve the field-alignment of the grid to represent all plasma flux surfaces. This chapter details the setbacks with this grid which were found after publication of reference [119]. Nevertheless, the results from the field line following analysis were compared with the understanding that further grid modifications must be addressed for a complete comparison to draw further physics conclusions regarding achieving stable detachment.

Chapter 6

Application of FLARE metrics for Two Configurations in W7-X

The objective of this chapter is to study the field line behavior in the plasma edge region of two selected magnetic equilibria in W7-X. The analysis and results will utilize the methods and tools implemented in chapters 3 and 4 to describe the field line behavior with the target. The analysis and simulations performed in this section consider only the vacuum vessel of W7-X as the main PFC. The island divertor and its extra components are not considered. As the island divertor was constructed for a specific magnetic configuration and topology, i.e. a resonant island that forms the island divertor, we remove these components to computationally explore the edge field line behavior freely. Like the previous chapters in which we studied selected equilibria in different devices with the wall as the main PFC, this is a first step toward identifying the location, geometry, and structure for NRD-like divertor solutions. This is particularly important for QI stellarators since NRDs have not been extensively studied in these stellarator configurations.

6.1 W7-X Edge Structure

W7-X is a 5-field period quasi-isodynamic (QI) stellarator with major radius $R = 5.5\,\mathrm{m}$ and average minor radius $a = 0.5\,\mathrm{m}$. The device shown in figure 6.1 from reference [126]

features 5 non-planar (gray) and 2 planar (brown) coils per half-field period. This results in 50 non-planar coils and 20 planar coils for the entire device.

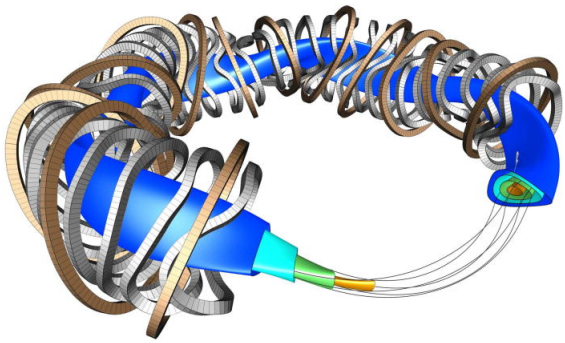

Figure 6.1: CAD rendering of W7-X coils taken from reference [126] showing the plasma contour's closed flux surfaces and field lines along with the 3D shaped non-planar coils in gray and planar coils in brown.

To analyze the selected magnetic equilibria in this chapter, we employ the FLARE code [83] like in the previous chapters. This is appropriate for W7-X as a QI configuration due to its low bootstrap current, especially compared to other stellarators. Table 6.1 lists the coil current for a half-field period for the two configurations studied in this chapter. As mentioned previously, the W7-X vacuum vessel is the only PFC considered in this chapter and serves as the necessary boundary input in FLARE.

		Magnetic Configuration	
		Standard	FMM
Coil Type	Non-planar #1 (A)	1450000	1446336
	Non-planar #2 (A)	1450000	1446336
	Non-planar #3 (A)	1450000	1446336
	Non-planar #4 (A)	1450000	1446336
	Non-planar #5 (A)	1450000	1446336
	Planar #1 (A)	0	-118404
	Planar #2 (A)	0	-118404

Table 6.1: Coil current amplitudes indicated for a half-field period for the studied magnetic configurations.

The Poincarè maps shown in figure 6.2 show the two W7-X magnetic equilibria we consider for this chapter. The left plot of this figure is the standard W7-X configuration that features the $\iota = 5/5$ island chain. This is the magnetic configuration which serves as

the basis for the island divertor discussed in chapter 2. The second case considered in this chapter is the so-called "FMM" case corresponding to the abbreviation labeling scheme which is used internally at the W7-X facility.

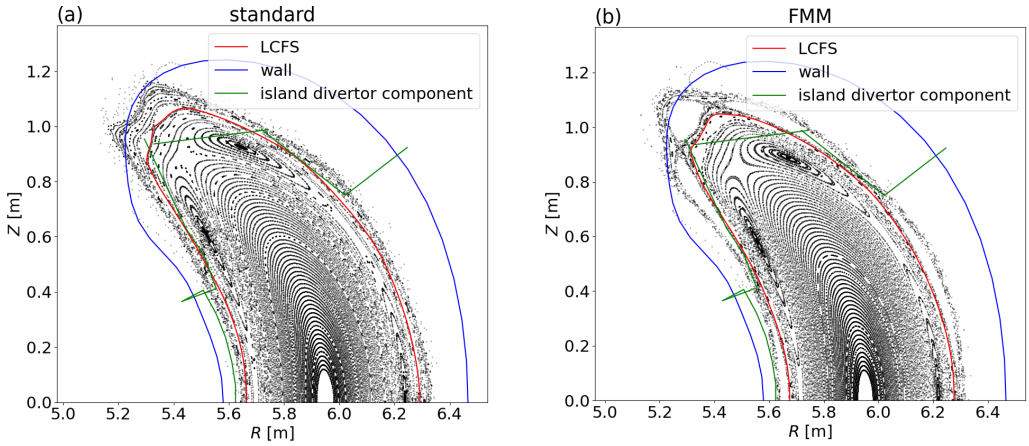

Figure 6.2: Poincarè map at $\phi = 0°$ for (a) standard and (b) FMM configurations. An estimation of the LCFS is plotted in red for each case with respect to the vessel wall plotted in dark blue. The island divertor targets are plotted in green in order to visualize the location of the 5/5 island chain with respect to the divertor. The island divertor structures are not included in the calculations of this chapter.

With respect to the island divertor geometry within W7-X shown in green in figure 6.2, the FMM magnetic configuration is one that is limited by the divertor plates where the altered coil currents for this equilibria shift the 5/5 island chain radially inward (also seen in figure 6.3). This results in the island divertor targets not intercepting this island chain, but a closed flux surface touching the divertor target, which establishes a limiter configuration[1]. This configuration features enhanced plasma performance explored experimentally at W7-X [127], [128]. It was shown that by shifting the 5/5 island chain inside the LCFS, development of an electron internal transport barrier (eITB) near the island resulted in an increase in the plasma core electron temperature T_e. This increase is considered

[1]We note that the large 5/5 internal island complicates the simple limiter structure described in chapter 2. The target still limits a closed flux surface which surrounds the inward shifted island chain. However, the large island chain creates a buffer region between the target and the inner plasma core region.

to be correlated with the observed increase in stored diamagnetic energy and, hence, improvement in plasma confinement [127], [128]. The FMM configuration studied in this chapter is one out of a set of identified FMM configurations currently under investigation at W7-X [129]. The coil currents for this particular equilibria are reported in table 6.1.

The analysis in this chapter, however, focuses on the field line behavior with respect to the vessel wall as the main PFC without the island divertor structures and other in-vessel components. Since these components are removed in this numerical exploration, this changes the interaction between the PFC and structures within the plasma edge. This can be seen already in figure 6.2. Furthermore, the LCFS shown in red in both configurations is much further outward due to the location of the vessel wall compared to where it is with the island divertor.

Figure 6.3 plots the rotational transform of each configuration as a function of major radius R. Both configurations feature the 5/5 island chain where the iota profile appears flat. The ι of the field lines outside of this rational surface continues to increase and is eventually > 1 at the edge. Figure 6.2 show that the region outside the LCFS is comprised of higher-order island chains along with their overlap causing a chaotic-like appearance of the field lines. The according $\iota > 1$ values can be seen accordingly in figure 6.3. We will see later in this chapter which structures are guiding the plasma wall interaction by calculating the magnetic footprint and the radial connection along the wall.

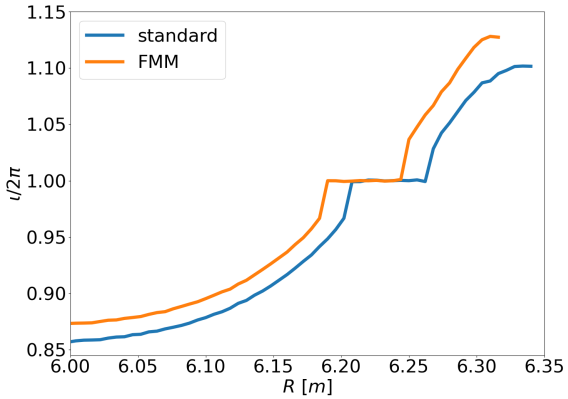

Figure 6.3: Rotational transform $\iota = \iota/2\pi$ profile for the standard (blue) and FMM (orange) magnetic configurations.

A calculation of the radial connection and magnetic footprint for a half-field period is shown in figure 6.4. A mesh is constructed $\sim 0.1\,\mathrm{cm}$ inward of the vessel wall. To create this mesh, a normalized arc length parameterization[2] was employed such that the arc length spans $[0, 1]$. We set 0 to correspond with the outboard midplane and increases

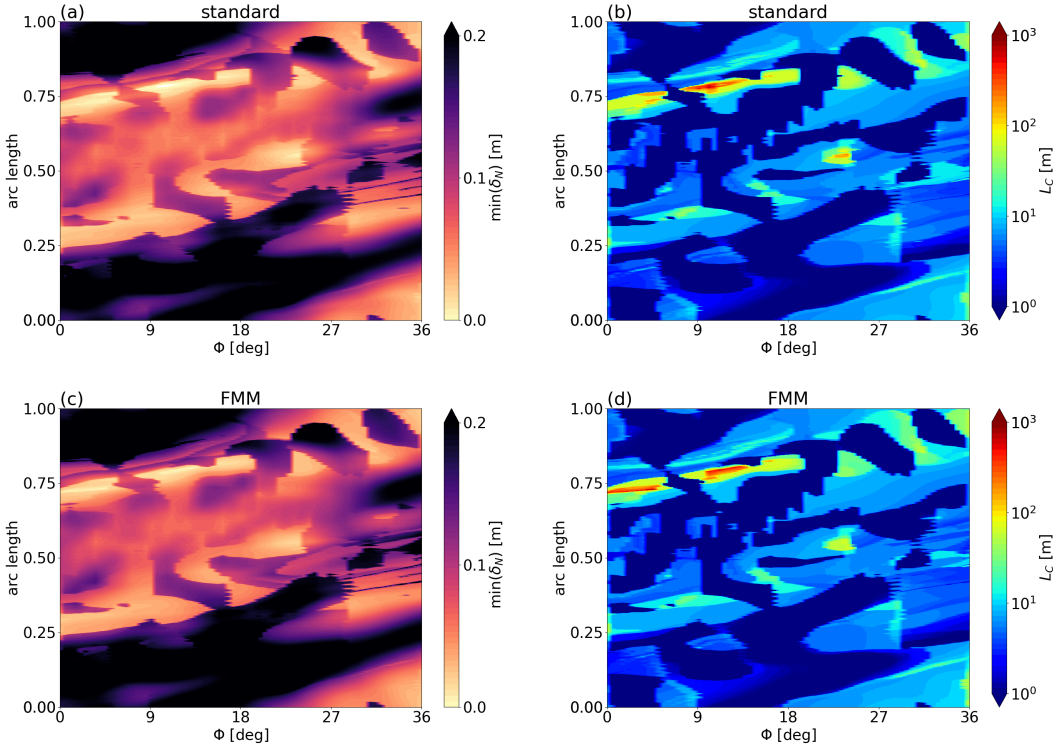

Figure 6.4: Radial connection (left column (a) and (c)) and magnetic footprint (right column (b) and (d)) for the standard (top row (a) and (b)) and FMM ((c) and (d)) configurations.

in the counterclockwise direction following the poloidal angle θ and returns to 1 at the outboard midplane. This is the y-axis in figures 6.4 and 6.5. The x-axis is the toroidal angle ϕ. Field lines were followed for a maximum L_C of 1 km in both forward and backward (counterclockwise and clockwise) directions. For both standard (figure 6.4 (b)) and FMM (figure 6.4 (d)), the highest L_C regions from yellow ($\mathcal{O}(10^2$ m)) to red ($\mathcal{O}(10^3$ m)) are between $0° \leq \phi \leq 18°$ at about 0.75 in arc length. These high L_C regions correspond to the major regions of anticipated heat and particle flux deposition on the wall. The

[2]This approach was necessary due to the concavity of the W7-X vacuum vessel. In contrast, the toroidal angle ϕ was a sufficient parameterization of the HSX lofted wall to create the mesh for field line tracing.

field lines' $\min(\delta_N)$ (figure 6.4 (a) and (c)) along the wall also follows a similar deposition pattern as the magnetic footprint similar to what was shown in chapter 4. The regions of low $\min(\delta_N)$ ($< \mathcal{O}(10^{-1}$ m)) are associated with longer connection lengths shown in figure 6.4 (b) and (d). As we have shown in previous chapters that drastically different magnetic equilibria will have similar magnetic footprints, it is expected that these plasma equilibria will also exhibit qualitatively very similar magnetic footprints and radial connection maps. This is also what is observed in figure 6.4 where the high L_C and low $\min(\delta_N)$ appear in a helical pattern along the wall. Within the helical envelope along the wall, however, the localized regions of L_C and low $\min(\delta_N)$ appear as separated clusters which may be due to the wall geometry. The magnetic footprint regions ranging from green ($\mathcal{O}(10$ m)) to dark blue ($\leq \mathcal{O}(1$ m)) (purple to black $\mathcal{O}(> 0.1$ m) in figures 6.4 (a) and (c)) are far SOL effects which we ignore in this analysis.

To emphasize the features within the high L_C (low $\min(\delta_N)$) region, figure 6.5 follows the field lines for $L_{C,max} = 10\,\text{km}$ on a higher resolution mesh spanning $\phi \in [0°, 18°]$ and normalized arc length $\in [0.625, 0.875]$. This extension demonstrates the differences which arise in the magnetic footprint between the two plasma configurations which were previously calculated in lower grid resolution in figure 6.4. Figure 6.5 (b) shows a localization of high L_C in red ($\mathcal{O}(10^4$m)) approximately between $9° \leq \phi \leq 12°$. This is in contrast to the FMM case depicted in figure 6.5 (d) where a poloidally narrow high L_C band extends from $0° \leq \phi \leq 6°$ and again from $10° \leq \phi \leq 15°$. This narrow band can also be seen in figure 6.5 (c) where the field lines have very small $\min(\delta_N)$ according to the colorbar. It is clear from these plots that these configurations must have different magnetic structures interacting with the PFC and for different toroidal extents.

Because of the differences in high connection length regions (particularly between $10° \leq \phi \leq 12°$), we consider figure 6.6 which plots the $\min(\delta_N)$ (left column (a) and (c)) and L_C (right column (b) and (d)) at $\phi = 10.5°$. The standard configuration is plotted in the top row while the FMM case is shown in the bottom row with a Poincarè map superimposed in black. Starting with the FMM case in figure 6.6 (d), we observe that the higher order

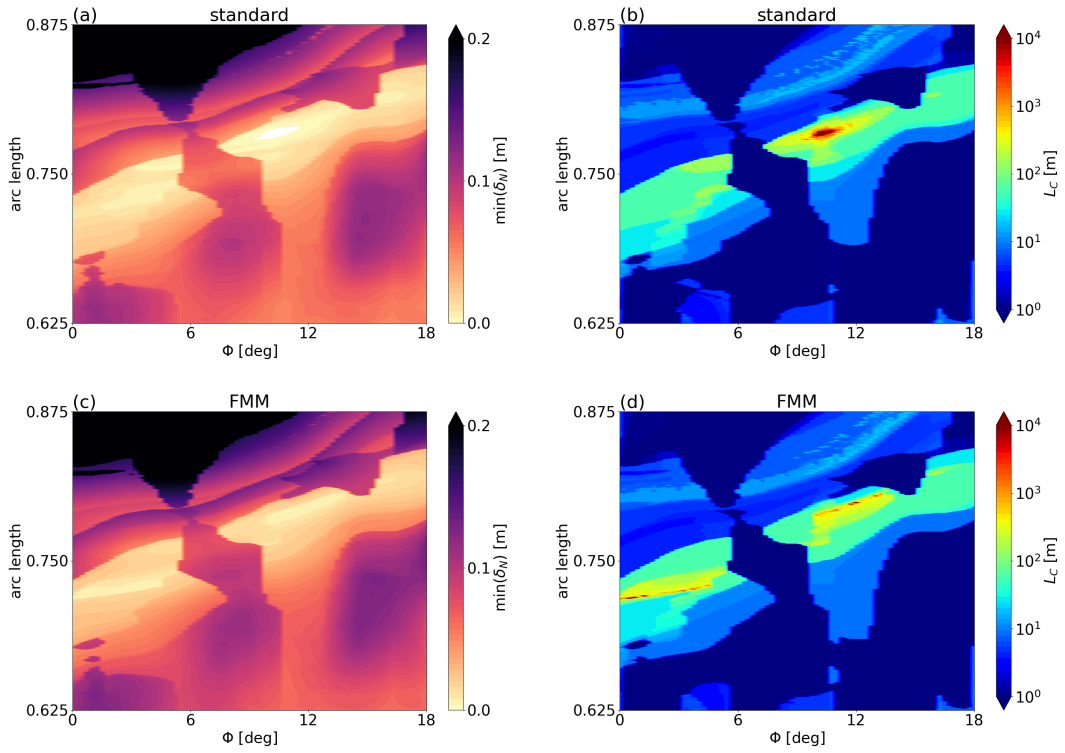

Figure 6.5: Higher resolution calculation of a limited range of figure 6.4. Radial connection (left column (a) and (c)) and magnetic footprint (right column (b) and (d)) for the standard (top row (a) and (b)) and FMM ((c) and (d)) configurations.

island chain intersected by the wall has low red-orange L_C ($\mathcal{O}(10^2$ m)) compared to the closed field lines with $L_C \sim \mathcal{O}(10^4$ m) in white. This indicates that the connection length of the field lines of the island chain intercepted by the wall is not contributing to the high L_C red region in figure 6.5. Moreover, the island is so deeply intercepted by the wall such that the field lines inside the island do not reach $L_C \sim \mathcal{O}(10^4)$ like in the large island configuration of HSX in chapter 4.

Figure 6.6 (c) also demonstrates this island's field lines are not contributing to the peak region of flux in figure 6.5. The values of min(δ_N) in this region are $\mathcal{O}(10^{-3}$ m) and are not associated with the island in this configuration. Within the island, the values of min(δ_N) are $> \mathcal{O}(10^{-3}$ m). This is in consistent to the previous chapter which suggested that islands with large L_C outside the LCFS have min(δ_N) $\sim \mathcal{O}(10^{-2}$ m). The dominant location of yellow L_C ($\mathcal{O}(10^3$ m)$-\mathcal{O}(10^4$ m)) extends toward the wall in a poloidally narrow

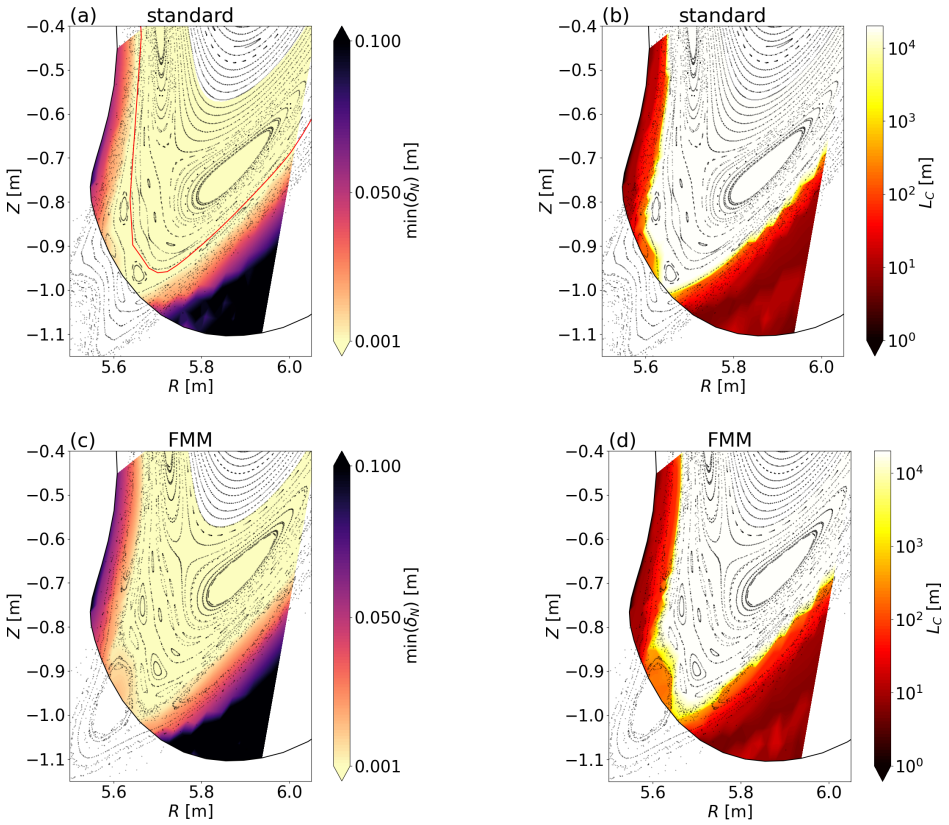

Figure 6.6: Calculation of $\min(\delta_N)$ (left column (a) and (c)) and L_C (right column (b) and (d)) for the standard (top row (a) and (b)) and FMM (bottom row (c) and (d)) cases at $\phi = 10.5°$.

manner. These field lines near the wall lie on what appears to be a broken flux surface outside of a higher-order island chain. This field line wall interaction from this broken surface highly resembles the HSX TEM configuration in chapter 4 which also featured chaotic-appearing field lines with long L_C interacting with the wall. The long L_C field line-wall interaction resulting from the TEM configuration was also a narrow helical band as seen in figure 4.7 along the wall. The field lines with $L_C \sim \mathcal{O}(10^3$ m) in figure 6.6 appear to contribute to the high L_C deposition regions of figure 6.5 (d).

This is in contrast to the strike line of the standard configuration. In figure 6.6 (b), long white L_C ($\mathcal{O}(10^4$ m)) extends toward the wall. This coincides with the superimposed Poincarè map which displays a closed flux surface that intercepts the wall. These combined observations convey that the standard configuration is one that is limited plasma wall

scenario with the wall as the main PFC. This helps elucidate the observed red localization spot of L_C in figure 6.5 (b) and is much like what was observed in the limited plasma configurations in CTH in chapter 3. Because the wall limits the plasma, this creates an obstacle in identifying a LCFS for the standard case in order to calculate the radial connection. Nonetheless, the LCFS was chosen to be the red curve overlaid in figure 6.6 (a).

Figure 6.7 further conveys where this configuration's closed flux surface is limited by the wall. This figure displays the connection length (top row) and radial connection (bottom row) at $\phi = 3°$ (left column) and $\phi = 10.5°$ (right column) using the data from figure 6.5. At $\phi = 10.5°$, the standard configuration (blue) shows that $L_{C,max} = 20\,\text{km}$

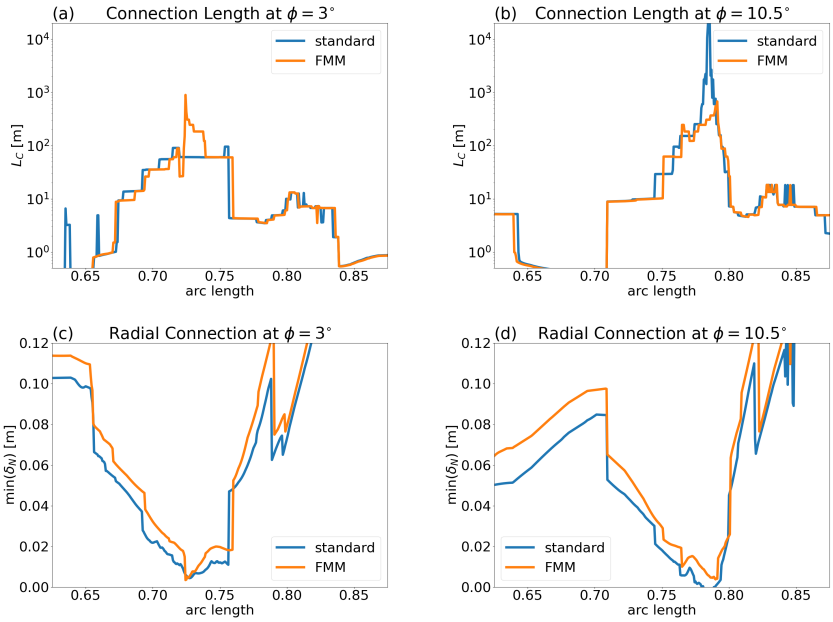

Figure 6.7: Connection length (top row (a) and (b)) and radial connection (bottom row (c) and (d)) as a function of arc length for $\phi = 3°$ (left column (a) and (d)) and $\phi = 10.5°$ (right column (b) and (d)). These values are from figure 6.5.

where figure 6.6 (b) confirms that a closed flux surface is intercepted by the wall. We note that in figure 6.7 (d), $\min(\delta_N)$ reaches a negative value. This occurs for the field lines which achieve $L_{C,max} = 20\,\text{km}$. We noted in chapter 4 that a positive $\min(\delta_N)$ is directed radially outward meaning that a negative one is radially inward. This value may

be occurring due to the interaction of the internal island chain's separatrix with the wall and the chosen LCFS for the calculation indicating that the surface may not be closed in the vicinity of the wall and internal island structure. This island chain appears near the wall just inside the closed flux surface that is intercepted by the wall shown in figures 6.6 (a) and (b) for the standard configuration. Nevertheless, it is observed that the overall behavior of the standard configuration's field lines near the wall in figures 6.7 tend to have shorter $\min(\delta_N)$. As there are no major island chains with $L_C \sim \mathcal{O}(10^4$ m) and $\min(\delta_N) \sim \mathcal{O}(10^{-2}$ m) in either magnetic configurations, the field line behavior in figures 6.4 - 6.7 demonstrates that the FMM case is a non-limited configuration since the field lines which interact with the wall appear to only have $L_C \sim \mathcal{O}(10^3$ m) like what is shown in figure 6.6 while the standard case is limited.

Figure 6.8 interprets the data from figures 6.5 and 6.7 by plotting the mesh's field lines' L_C vs $\min(\delta_N)$ for a few values of ϕ. This is similar to the power law analysis in

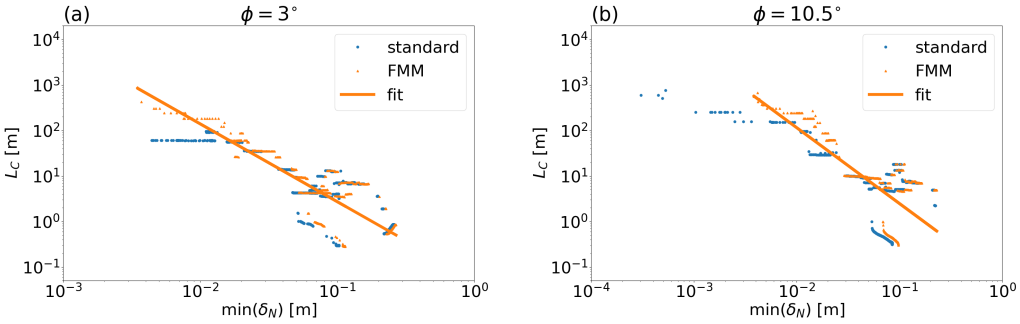

Figure 6.8: L_C vs $\min(\delta_N)$ for $\phi = 10.5^\circ$ for standard (blue circles) and FMM (orange triangles). A power law fitting is applied to the FMM case's data taken from figures 6.5 and 6.7.

chapter 4. We use a power law of the same form $L_C = b\ \min(\delta_N)^a$. This fit is performed on the FMM (orange triangle markers) configuration's data and is overlaid on these plots in orange. Table 6.2 tabulates the estimated coefficients a and b for various ϕ along the calculation mesh in figure 6.5. The estimates of the exponent coefficient a are comparable to what was calculated in the previous chapter for different magnetic configuration and wall vessel. In chapter 4, a was estimated to be -1.71 ± 0.02 and -1.74 ± 0.03 at $\phi = 5^\circ$

and $\phi = 18°$, respectively. This further reinforces that the FMM case's magnetic edge structure is similar to the TEM case in the previous chapter and suggests that the field lines of this broken surface are interacted with a cantorus (or cantori). The standard case (blue circle markers) is more difficult to interpret and we note that the negative values of $\min(\delta_N)$ at $L_{C,max}$ are removed in figure 6.8. As the last chapter did not have any limited plasma equilibria, the standard case here does not have a comparable magnetic configuration which was studied in HSX.

However, the data does overall follow the power law in figure 6.8 (b) at $\phi = 10.5°$ and does not have bifurcated behavior exhibited with large islands present in the edge. This agrees with the results of chapter 4 that when large edge islands dominate the strike line behavior, the field lines of these islands will follow different behavior than what is observed along the separatrix or LCFS. For the standard case which is limited with no large islands interacting with the wall, the trend of the data following the power law is consistent what was shown in the last chapter that the field lines are near or along the separatrix. For the limited configuration, we observe that the field lines follow the overall power law relation, similar to the FMM case. In regions where the plasma is not limited, however, there is an observed deviation from the power law in the standard configuration. This is shown in figure 6.8 where at $\phi = 3°$ field lines with constant $L_C \sim \mathcal{O}(10^2 \text{ m})$ and $\min(\delta_N) \sim \mathcal{O}(10^{-2} \text{ m})$ do not follow the power law. This lack in localized high L_C is also visible the standard case's magnetic footprint in figure 6.5 at $\phi = 3°$. At this toroidal angle, the LCFS or separatrix does not interact with the wall. Furthermore, this is unlike a large edge island interacting with the PFC which may have $L_C \sim \mathcal{O}(10^4 \text{ m})$ with moderate $\min(\delta_N)$, like in the last chapter for the large island configuration in HSX.

We note in table 6.2, that there are a few values of a which deviate further away from what was estimated in the last chapter. This could possibly be attributed to geometry variation of the PFC in the edge. How geometry of the PFC influences this power law relation necessitates further studies which were not considered here. Nevertheless, a power law relation does describe the behavior of these field lines, but more analysis could be

applied in the future to investigate further the impact of geometry and whether or not there are other magnetic topological structures to consider.

ϕ [°]	a	b
1	-1.78 ± 0.07	0.03 ± 1.23
3	-1.71 ± 0.05	0.05 ± 1.16
5	-2.25 ± 0.04	0.006 ± 1.13
9	-1.57 ± 0.34	0.03 ± 0.14
10	-1.7 ± 0.08	0.04 ± 1.27
10.5	-1.66 ± 0.08	0.05 ± 1.26
11	-1.38 ± 0.07	0.14 ± 1.24
12	-1.77 ± 0.1	0.03 ± 1.3
13	-2.36 ± 0.11	0.003 ± 1.37

Table 6.2: Estimated values of a and b for the power law fit $L_C = b \min(\delta_N)^a$ for the FMM configuration at various ϕ values corresponding the calculation mesh in figure 6.5.

6.2 Summary

Using the tools developed and tested in CTH and HSX described in the previous chapters, we have identified consistent features in the edge magnetic structure which gives rise to the major regions of anticipated heat and particle deposition. Namely, the standard configuration is limited while the FMM features a broken flux surface whose long L_C field lines interact with the wall. We confirm that a power law can be applied to between the L_C and $\min(\delta_N)$ of these field lines along the mesh.

The choice of using these high-performing scenarios (with respect to the island divertor) in W7-X show that these configurations do not exhibit features in the plasma edge which are connected to NRDs with an open chaotic layer as seen in previous chapters. The similar high L_C and low $\min(\delta_N)$ regions reveal that a resilient helical strike line feature does manifest along the wall as shown in reference [14] showing a helical "trough" which could be constructed for divertor studies. By removing the island divertor target, we demonstrate how field line following along the W7-X vacuum vessel reveals different field line behavior with the PFC than what is tested experimentally for the island divertor. In a similar way that the island divertor is dependent on a magnetic configuration in W7-X,

NRD-like configurations within W7-X must be treated similarly. The field line structure must be studied further with plasma transport calculations (such as with EMC3-EIRENE) in order to see if these magnetic configurations are advantageous as a divertor solution. The calculated field line interaction with the PFC in this chapter is a starting point for continued analysis which could involve studying more magnetic configurations along with simulating the transport in the edge. This would also help in identifying and constructing mechanical structures in the edge such that a divertor solution could be made.

Chapter 7

Conclusion

In this thesis, we have computationally explored resilient stellarator divertor behavior across three different devices. This was performed with the motivation of studying non-resonant divertors (NRDs) as an alternative stellarator divertor solution. Throughout this thesis, we have used "NRD" to mean that no large island is intercepted by the wall or PFC like in the island (resonant) divertor. These configurations are also not limited plasma wall scenarios where a good closed flux surface is intercepted by the PFC. Rather, NRDs feature an open chaotic layer (which can feature many edge resonances) in the plasma edge and we have investigated the impact of these structures within the context of divertor resiliency. Moreover, we aim to resolve the fundamental structural features of NRD scenarios for stellarators and explore basic trends of their divertor performance.

In CTH, we explored the fundamental features of the edge magnetic structure and its interaction with a simple circular wall geometry. The resulting resilient strike line was assessed through variation in wall location and presence of an open chaotic layer. Here, resiliency means that the formed strike line across all magnetic configurations remains within the same helical band on the PFC. Differences within the helical pattern across the configurations are observed as sub-structural details that are connected to the magnetic structure of the various plasma configurations. As we have shown in this thesis, large variation can occur across the configurations by featuring plasma edge magnetic structures

such as islands and an open chaotic layer. By studying the structures within the open chaotic layer present in the magnetic configurations, we were able to differentiate between diverted and limited plasma wall scenarios.

In the magnetic configurations which were diverted, the features within their magnetic edge structure were related to similar structures observed in TEXTOR ergodic divertor [71]–[75] and Tore Supra [65], [76]. Namely, the presence of heteroclinic tangles extending from X-points in the diverted CTH configurations are linked to the heat load pattern on the wall. These formed the divertor legs that channeled plasma flux to the PFC. These equilibria were then simulated with EMC3-EIRENE to connect the plasma transport behavior to the magnetic structure analyzed with field line following. The deposited heat flux on the wall for the diverted scenarios were connected to the tangles serving as divertor legs. This was not observed in the limiter scenarios where a close flux surface or quasi-flux surface was intercepted by the wall. Moreover, the magnetic structures in the edge and their relation to the pattern of the strike line and wall deposition pattern contributed to an initial scoping study of where a physical divertor could be located for an NRD as a resilient divertor in CTH.

Based on the fundamental findings in CTH, HSX was studied next as a quasi-helically symmetric (QHS) optimized stellarator with the inclusion of an shaped expanded lofted wall [24]. The strike line on the lofted wall resulted in resilient wall behavior across all magnetic configurations, including the large island equilibria. This is in contrast to previous work where it was found that this configuration is not resilient due to the presence of a large island in the edge [15]. By using an expanded wall in our analysis, however, this increased the distance between the island and the wall and resulted in contributing to the overall resilient behavior.

To study this observed resiliency and the detailed sub-structures within the helical band further we introduced a new metric, the minimum radial connection $\min(\delta_N)$ to quantify the differences in magnetic structure and its interaction with the wall. Specifically, the field lines' deviations from an empirical power law using the ansatz $L_C = b\ \min(\delta_N)^a$

helped delineate features of the strike line associated with islands. This was observed in the large island configuration of HSX featuring the 4/4 island chain. When the field lines L_C and $\min(\delta_N)$ followed this power law, this indicated that field lines intersecting the wall were associated with the separatrix or LCFS of a configuration. Within this power law behavior, the field lines with long $L_C \sim \mathcal{O}(10^4\text{m})$ and $\min(\delta_N) \sim \mathcal{O}(10^{-3}\text{m})$ can be connected to interacting with a cantorus (or cantori) before eventually reaching the wall. Moreover, this overall quantification of the differences in strike line behavior on the lofted wall due to different magnetic structures helps in scoping out a space for a potential resilient divertor implementation for HSX.

With the described field line structure analysis, it is of interest to investigate the plasma transport of HSX with the lofted wall through simulation with EMC3-EIRENE. We selected configurations based on differences in edge island size and location in order to assess SOL behavior and see if detachment could be achieved on the bare wall, particular in the presence of open chaotic structures. The simulated downstream density as a function of upstream density n_u along with the peak particle flux Γ_t behavior indicated that the particle flux remains attached and never reaches a high-recycling regime. This lack of high-recycling has been observed in other stellarator devices and is attributed to the upstream momentum losses due to counter streaming flows in the open chaotic layer. Meanwhile, the downstream temperature $T_{\{e,i\}d}$ and peak heat flux Q_t trends support that the plasma detaches thermally from the target (energy detachment). These trends were connected to the power balance analysis which demonstrated the reduction in power to the target P_T coinciding with an accumulation in power due to plasma-neutral interactions P_{NG} as n_u increased. This overall behavior was shown despite a $20\% - 30\%$ power loss uncertainty due to grid misalignment issues. The simulated heat and particle flux on the wall location was also studied and found to be consistent with the results of field line following modeling for the QHS and large island configuration. While the location of the resilient strike line in EMC3-EIRENE remained consistent with field line following, however, the amount of target heat and particle flux is likely underestimated based on the power loss uncertainty.

These results served as a basis for future work into grid improvements for a deeper analysis into what is needed for a physical resilient divertor structure. This is important not only for identifying a mechanical structure(s) to improve volumetric particle recombination for full detachment, but also for understanding other physics parameters, such as the role of counter-streaming flows for detachment, in the presence of an open chaotic layer as seen in the QHS configuration.

Finally, the methodologies developed and tested for CTH and HSX were applied to W7-X, a quasi-isodynamic (QI) optimized stellarator. These were applied to high-performance scenarios which were found by changing the rotational transform and shifting the 5/5 island chain. The studied plasma equilibria were studied by removing the current in-vessel island divertor components in order to explore the open field line behavior of these configurations with the wall as the main PFC. Additionally, this analysis was done to scope out a resilient NRD-like mechanical structure. Through the application of the field line following metrics developed in this thesis, it was seen that the field lines of the chosen magnetic configurations at the wall followed the empirical power law relationship consistent with the HSX investigation. This occurred despite both configurations not featuring an open chaotic layer like the QHS configuration in HSX. Rather, these equilibria overall followed a power law relationship between the field lines' L_C and $\min(\delta_N)$ when the field lines are along the separatrix or LCFS and interact with the wall. This was also the case when one of the chosen configurations had a closed flux surface which was intercepted by the wall and was therefore a limiter. These magnetic configurations, moreover, did not feature a large island intersecting the PFC like in the HSX analysis. Thus, the field lines of these configurations did not exhibit features which were associated with the 4/4 large island configuration in HSX. The field line following application to W7-X as a QI device shows that further adjustments of the rotational transform is necessary to find and test equilibria that are NRD-like in edge magnetic structure. This is specifically important in a low magnetic shear QI stellarator like W7-X which is very susceptible to equilibrium effects that change the magnetic edge structure and hence the divertor configuration.

7.1 Future Work

The magnetic structures in the edge and their relation to the strike line and wall deposition pattern contributed to an initial scoping study of where a physical divertor could be located for an NRD as a resilient divertor in CTH. Ongoing work at CTH has shown qualitative agreement of the strike line location for plasma equilibria with similar features modeled in this thesis [104]. In reference [104] this includes implementation of Langmuir probes arrays to measure ion flux measurements at the edge of CTH plasmas for verification of the magnetic features discussed in this work. Additionally, plasma density and temperature information from the Langmuir probes can be compared to results from EMC3-EIRENE simulations. While it is possible to verify the edge behavior in a low-recycling SOL regime on a device like CTH, the conditions for plasma detachment are not achievable.

In W7-X, NRD magnetic configurations are a subject of ongoing experimental studies. The configuration denoted as "CYM" with similar chaotic edge features as NRDs was operated in W7-X in May 2025 to assess if the experimentally measured strike line is connected to the edge magnetic structure [130].

Future work pertaining to NRDs in optimized quasisymmetric stellarator configurations requires simulation of divertor performance metrics. Specifically, metrics such as simulation of neutral behavior, like what was done in [119], and the presence of impurities must also be accounted for divertor performance calculations. These metrics are especially important to examine the influence of plasma edge magnetic structures for continued detachment studies. It has been shown in this thesis that NRDs feature an open chaotic layer in the plasma edge and an open question remains if this magnetic structure and the consequent counter-streaming flows prevent access to high-recycling and stable particle detachment. Moreover, this thesis identified necessary grid improvements to more accurately simulate the edge transport behavior with codes like EMC3-EIRENE. Application of these improvements for these metrics will also help inform the construction and design of NRDs which are of interest for future experiments [131] and stellarator fusion pilot plants [132].

Appendix A

Appendix

A.1 Power Loss Analysis in EMC3-EIRENE for the Large Island Configuration in HSX

Like in section 5.1, the power balance for this configuration also conveys that the modeled grid also suffers from power losses due to mapping surfaces. Figure A.1 plots the power balance using the same convention as figure 5.12. Additionally, table A.1 considers the ratios of P_{SL}/P_T and P_{SL}/P_{Total} like in table 5.3. Together, these show that the generated large island grid suffers from a slightly smaller influence of P_{SL} compared to the QHS case. Furthermore, the P_{NG} increases with n_u while P_T decreases, similar to what was observed for the QHS configuration. More n_u cases are necessary, however, to fully examine the power balance behavior. These must be accompanied with grid improvements as described in chapter 5.

$n_e \times 10^{13}$ [cm^{-3}]	P_{SL}/P_T	P_{SL}/P_{Total}
2	0.23	0.17
3	0.32	0.14

Table A.1: Power lost to surface mapping P_{SL} compared to power to target P_T and total power P_{Total} for the large island configuration grid.

To examine the overall power lost in the simulation due to non-overlapping mapping surfaces, we perform the post-processing EMC3-EIRENE routine for the 2 large island

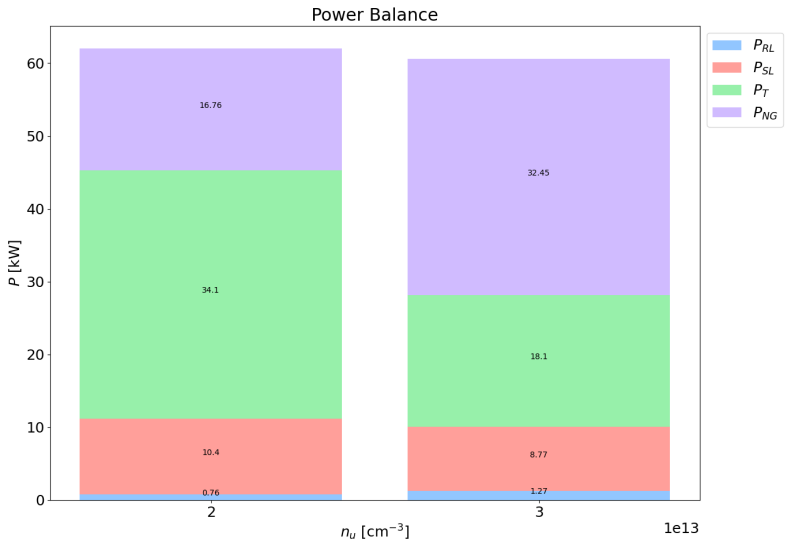

Figure A.1: SOL power balance as a function of n_u for the large island configuration. The total input power was set to 500 kW corresponding to 62.5 kW for the simulation domain (an eighth of HSX). Plotted is the the power radiated from neutral gas interactions (P_{NG} light purple), power deposited onto the target (P_T light green), and power lost to mapping surfaces from parallel and perpendicular transport (P_{SL} coral and P_{RL} light blue, respectively).

density cases. Using the same convention in the previous section of power mapped to the target ($P_{SL,depo}, P_{T,depo}$) and power to the target (P_{SL}, P_T), we tabulate the ratios of these quantities in table A.2 like in table 5.4. The first column entry conveys the impact of varying the NT_S parameter is also shown in table A.2. Increasing NT_S has a similar impact as in section 5.2 where the overall power lost to the simulation is dramatically reduced and nearly all P_{SL} is mapped onto the target.

NT_S	$n_e \times 10^{13}$ [cm^{-3}]	$P_{T,depo}/P_T$	$P_{SL,depo}/P_{SL}$
3,3	2	0.99	0.63
3,3	3	0.99	0.49
100,100	2	1	1
100,100	3	1	1

Table A.2: Ratio of flux mapped onto target vs to the target expressed for target power P_T and power lost to surface mapping P_{SL}. Increasing the parameter NT_S improves the overall power loss in the simulation seen in ratio $P_{SL,depo}/P_{SL}$.

The results of the EMC3-EIRENE deposition routine for the large island case for NT_S

$= (3, 3)$ and $(100, 100)$ are shown in figures A.2 and 5.16 respectively. Like in sections 5.1.1 and 5.2.2, the locations of deposition qualitatively agree with the FLARE modeled strike points on the lofted wall. Moreover, the improved $P_{SL,depo}/P_{SL}$ shows that the locations of deposition robustly stay in the same helical region and qualitatively correspond with the FLARE generated strike points. These points are superimposed in gray and black. Minor discrepancies in the target deposition location outside of the helical strike line appear similar to what is described in 5.2.2.

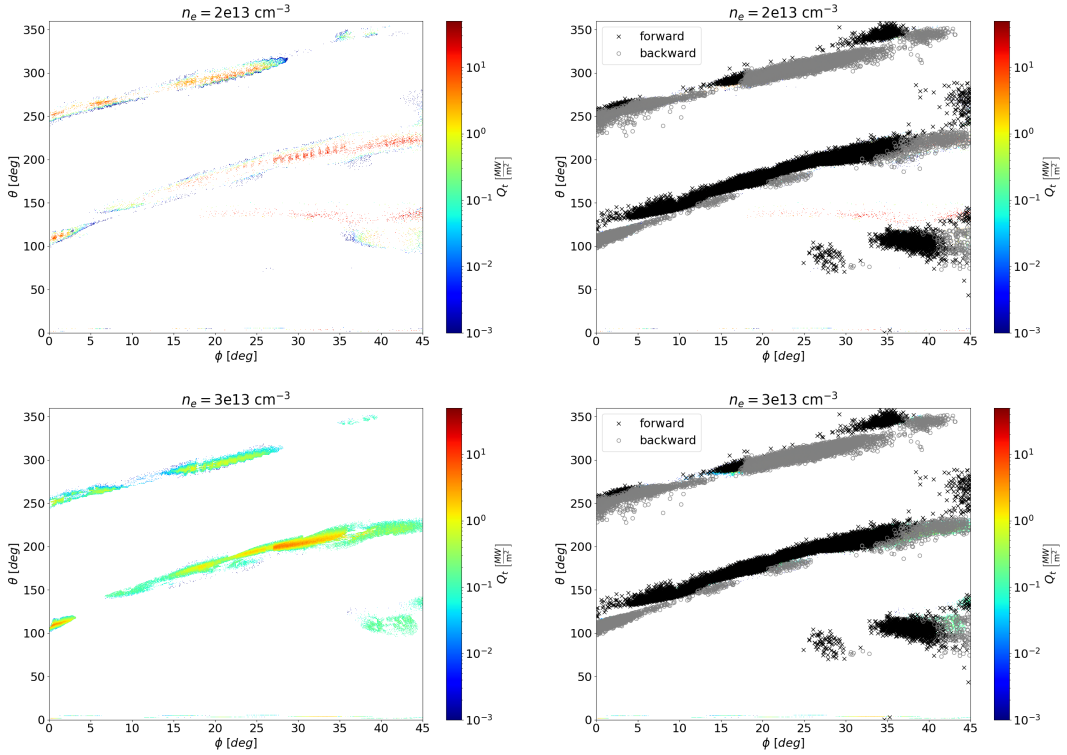

Figure A.2: Heat flux deposition on wall for large island configuration. Left column plots the heat flux Q_t while the right column superimposes the FLARE generated strike points on the heat flux map.

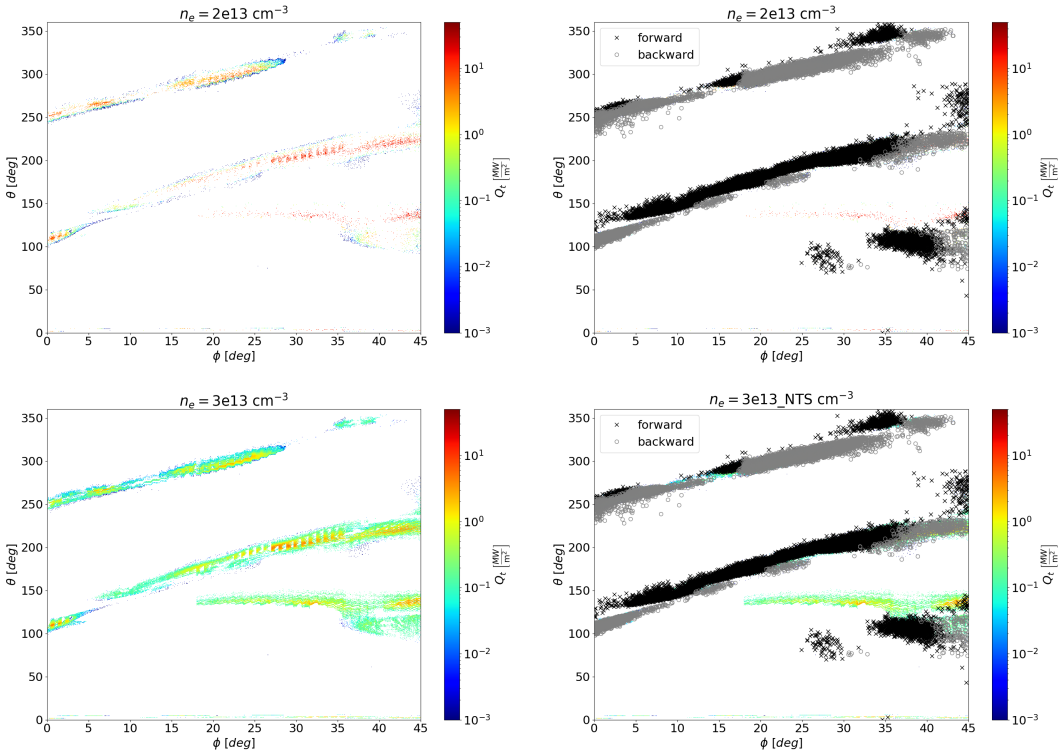

Figure A.3: Heat flux deposition on wall for large island configuration with NT_S= $(100, 100)$. Left column plots Q_t while the right column superimposes the FLARE generated strike points on the heat flux map. This figure is the same as figure 5.16.

Bibliography

[1] R. A. Pitts, X. Bonnin, F. Escourbiac, *et al.*, "Physics basis for the first ITER tungsten divertor," *Nuclear Materials and Energy*, vol. 20, p. 100 696, Aug. 2019, ISSN: 2352-1791. DOI: 10.1016/j.nme.2019.100696.

[2] J. D. Lawson, "Some Criteria for a Power Producing Thermonuclear Reactor," en, *Proceedings of the Physical Society. Section B*, vol. 70, no. 1, p. 6, Jan. 1957, ISSN: 0370-1301. DOI: 10.1088/0370-1301/70/1/303.

[3] A. B. Zylstra, O. A. Hurricane, D. A. Callahan, *et al.*, "Burning plasma achieved in inertial fusion," en, *Nature*, vol. 601, no. 7894, pp. 542–548, Jan. 2022, Publisher: Nature Publishing Group, ISSN: 1476-4687. DOI: 10.1038/s41586-021-04281-w.

[4] J. Wesson, *Tokamaks*, 4th. Oxford University Press, Dec. 2011, ISBN: 0199592234.

[5] J. Nührenberg and R. Zille, "Quasi-helically symmetric toroidal stellarators," en, *Physics Letters A*, vol. 129, no. 2, pp. 113–117, May 1988, ISSN: 0375-9601. DOI: 10.1016/0375-9601(88)90080-1.

[6] M. Landreman, S. Buller, and M. Drevlak, "Optimization of quasi-symmetric stellarators with self-consistent bootstrap current and energetic particle confinement," *Physics of Plasmas*, vol. 29, no. 8, p. 082 501, Aug. 2022, ISSN: 1070-664X. DOI: 10.1063/5.0098166.

[7] A. Redl, C. Angioni, E. Belli, O. Sauter, ASDEX Upgrade Team, and EUROfusion MST1 Team, "A new set of analytical formulae for the computation of the bootstrap current and the neoclassical conductivity in tokamaks," *Physics of Plasmas*, vol. 28, no. 2, p. 022 502, Feb. 2021, ISSN: 1070-664X. DOI: 10.1063/5.0012664.

[8] H. Renner, E. Anabitarte, E. Ascasibar, *et al.*, "Initial operation of the Wendelstein 7AS advanced stellarator," en, *Plasma Physics and Controlled Fusion*, vol. 31, no. 10, p. 1579, Aug. 1989, ISSN: 0741-3335. DOI: 10.1088/0741-3335/31/10/008.

[9] C. Beidler, G. Grieger, F. Herrnegger, *et al.*, "Physics and Engineering Design for Wendelstein VII-X," *Fusion Technology*, vol. 17, no. 1, pp. 148–168, Jan. 1990, Publisher: Taylor & Francis _eprint: https://doi.org/10.13182/FST90-A29178, ISSN: 0748-1896. DOI: 10.13182/FST90-A29178.

[10] P. Grigull, K. McCormick, J. Baldzuhn, *et al.*, "First island divertor experiments on the W7-AS stellarator," en, *Plasma Physics and Controlled Fusion*, vol. 43, no. 12A, A175, Nov. 2001, ISSN: 0741-3335. DOI: 10.1088/0741-3335/43/12A/313.

[11] H. Renner, J. Boscary, H. Greuner, *et al.*, "Divertor concept for the W7-X stellarator and mode of operation," en, *Plasma Physics and Controlled Fusion*, vol. 44, no. 6, p. 1005, May 2002, ISSN: 0741-3335. DOI: 10.1088/0741-3335/44/6/325.

[12] R. C. Wolf, A. Alonso, S. Äkäslompolo, *et al.*, "Performance of Wendelstein 7-X stellarator plasmas during the first divertor operation phase," *Physics of Plasmas*, vol. 26, no. 8, p. 082 504, Aug. 2019, ISSN: 1070-664X. DOI: 10.1063/1.5098761.

[13] N. Ohyabu, T. Watanabe, H. Ji, *et al.*, "The Large Helical Device (LHD) helical divertor," en, *Nuclear Fusion*, vol. 34, no. 3, p. 387, Mar. 1994, ISSN: 0029-5515. DOI: 10.1088/0029-5515/34/3/I07.

[14] E. Strumberger, "Magnetic field line diversion in Helias stellarator configurations: Perspectives for divertor operation," en, *Nuclear Fusion*, vol. 32, no. 5, p. 737, 1992, ISSN: 0029-5515. DOI: 10.1088/0029-5515/32/5/I02.

[15] A. Bader, A. H. Boozer, C. C. Hegna, S. A. Lazerson, and J. C. Schmitt, "HSX as an example of a resilient non-resonant divertor," *Physics of Plasmas*, vol. 24, no. 3, p. 032 506, 2017, Publisher: American Institute of Physics, ISSN: 1070-664X. DOI: 10.1063/1.4978494.

[16] K. A. Garcia, A Bader, D Boeyaert, *et al.*, "Resilient stellarator divertor characteristics in the Helically Symmetric eXperiment," en, *Plasma Physics and Controlled Fusion*, vol. 67, no. 3, p. 035 011, Feb. 2025, Publisher: IOP Publishing, ISSN: 0741-3335. DOI: 10.1088/1361-6587/adb179.

[17] A. Bader, C. C. Hegna, M. Cianciosa, and G. J. Hartwell, "Minimum magnetic curvature for resilient divertors using Compact Toroidal Hybrid geometry," en, *Plasma Physics and Controlled Fusion*, vol. 60, no. 5, p. 054 003, Mar. 2018, Publisher: IOP Publishing, ISSN: 0741-3335. DOI: 10.1088/1361-6587/aab1ea.

[18] K. A. Garcia, A. Bader, H. Frerichs, *et al.*, "Exploration of non-resonant divertor features on the Compact Toroidal Hybrid," *Nuclear Fusion*, vol. 63, no. 12, p. 126 043, Oct. 2023, ISSN: 0029-5515. DOI: 10.1088/1741-4326/ad0160.

[19] J. T. Peterson, G. J. Hartwell, S. F. Knowlton, J. Hanson, R. F. Kelly, and C. Montgomery, "Initial Vacuum Magnetic Field Mapping in the Compact Toroidal Hybrid," en, *Journal of Fusion Energy*, vol. 26, no. 1, pp. 145–148, Jun. 2007, ISSN: 1572-9591. DOI: 10.1007/s10894-006-9053-2.

[20] G. J. Hartwell, S. F. Knowlton, J. D. Hanson, D. A. Ennis, and D. A. Maurer, "Design, Construction, and Operation of the Compact Toroidal Hybrid," *Fusion Science and Technology*, vol. 72, no. 1, pp. 76–90, Jul. 2017, Publisher: Taylor & Francis _eprint: https://doi.org/10.1080/15361055.2017.1291046, ISSN: 1536-1055. DOI: 10.1080/15361055.2017.1291046.

[21] Y. Feng, F. Sardei, J. Kisslinger, P. Grigull, K. McCormick, and D. Reiter, "3D Edge Modeling and Island Divertor Physics," en, *Contributions to Plasma Physics*, vol. 44, no. 1-3, pp. 57–69, 2004, ISSN: 1521-3986. DOI: 10.1002/ctpp.200410009.

[22] D. Reiter, M. Baelmans, and P. Börner, "The eirene and B2-eirene codes," *Fusion Science and Technology*, vol. 47, Feb. 2005. DOI: 10.13182/FST47-172.

[23] F. S. B. Anderson, A. F. Almagri, D. T. Anderson, P. G. Matthews, J. N. Talmadge, and J. L. Shohet, "The Helically Symmetric Experiment, (HSX) Goals, Design and Status," *Fusion Technology*, vol. 27, no. 3T, pp. 273–277, Apr. 1995, Publisher: Taylor & Francis _eprint: https://doi.org/10.13182/FST95-A11947086, ISSN: 0748-1896. DOI: 10.13182/FST95-A11947086.

[24] J. Schmitt, D. Boeyaert, A. Bader, *et al.*, "Vacuum vessel design with lofted toroidal surfaces for a QHS configuration," *Fusion Engineering and Design*, vol. 211, p. 114 731, Feb. 2025, ISSN: 0920-3796. DOI: 10.1016/j.fusengdes.2024.114731.

[25] C. S. Pitcher and P. C. Stangeby, "Experimental divertor physics," en, *Plasma Physics and Controlled Fusion*, vol. 39, no. 6, p. 779, Jun. 1997, ISSN: 0741-3335. DOI: 10.1088/0741-3335/39/6/001.

[26] P. C. Stangeby, "A tutorial on some basic aspects of divertor physics," en, *Plasma Physics and Controlled Fusion*, vol. 42, no. 12B, B271, Dec. 2000, ISSN: 0741-3335. DOI: 10.1088/0741-3335/42/12B/321.

[27] L. Spitzer Jr. and L Witten, "US Atomic Energy Commission Report No," 1951.

[28] L. Spitzer Jr., "The Stellarator Concept," *The Physics of Fluids*, vol. 1, no. 4, pp. 253–264, Jul. 1958, ISSN: 0031-9171. DOI: 10.1063/1.1705883.

[29] M. Keilhacker and A. Team, "The ASDEX divertor tokamak," en, *Nuclear Fusion*, vol. 25, no. 9, p. 1045, Sep. 1985, ISSN: 0029-5515. DOI: 10.1088/0029-5515/25/9/008.

[30] A. Team, "The H-Mode of ASDEX," en, *Nuclear Fusion*, vol. 29, no. 11, p. 1959, Nov. 1989, ISSN: 0029-5515. DOI: 10.1088/0029-5515/29/11/010.

[31] P. C. Stangeby, *The Plasma Boundary of Magnetic Fusion Devices*. Boca Raton: CRC Press, Dec. 1999, ISBN: 978-0-367-80148-9. DOI: 10.1201/9780367801489.

[32] Y. Feng, F. Sardei, P. Grigull, K. McCormick, J. Kisslinger, and D. Reiter, "Physics of island divertors as highlighted by the example of W7-AS," en, *Nuclear Fusion*, vol. 46, no. 8, p. 807, Jul. 2006, ISSN: 0029-5515. DOI: 10.1088/0029-5515/46/8/006.

[33] M. Keilhacker, K. Lackner, K. Behringer, H. Murmann, and H. Niedermeyer, "Plasma Boundary Layer in Limiter and Divertor Tokamaks," en, *Physica Scripta*, vol. 1982, no. T2B, p. 443, Jan. 1982, ISSN: 1402-4896. DOI: 10.1088/0031-8949/1982/T2B/022.

[34] V. R. Winters, "Carbon Sourcing and Transport in the Island Divertor of Wendelstein 7-X," Ph.D. dissertation, University of Wisconsin-Madison, Sep. 2019.

[35] O. Schmitz, Y. Feng, M. Jakubowski, *et al.*, "Stable heat and particle flux detachment with efficient particle exhaust in the island divertor of Wendelstein 7-X," en, *Nuclear Fusion*, vol. 61, no. 1, p. 016 026, Dec. 2020, Publisher: IOP Publishing, ISSN: 0029-5515. DOI: 10.1088/1741-4326/abb51e.

[36] S Masuzaki, H Tanaka, M Kobayashi, and G Kawamura, "Effects of drifts on divertor plasma transport in LHD," *Nuclear Materials and Energy*, vol. 18, pp. 281–284, Jan. 2019, ISSN: 2352-1791. DOI: 10.1016/j.nme.2019.01.009.

[37] Y. Feng, M. Kobayashi, F. Sardei, *et al.*, "Comparative divertor-transport study for helical devices," en, *Nuclear Fusion*, vol. 49, no. 9, p. 095 002, Aug. 2009, ISSN: 0029-5515. DOI: 10.1088/0029-5515/49/9/095002.

[38] S. R. Hudson and Y. Suzuki, "Chaotic coordinates for the Large Helical Device," *Physics of Plasmas*, vol. 21, no. 10, p. 102 505, Oct. 2014, ISSN: 1070-664X. DOI: 10.1063/1.4897390.

[39] S. Masuzaki, T. Morisaki, N. Ohyabu, *et al.*, "The divertor plasma characteristics in the Large Helical Device," en, *Nuclear Fusion*, vol. 42, no. 6, p. 750, Jun. 2002, ISSN: 0029-5515. DOI: 10.1088/0029-5515/42/6/313.

[40] M. Kobayashi, S. Morita, and M. Goto, "2D distribution of hydrogen/impurity radiation and flow formation in stochastic layer during detachment transition in LHD," *Nuclear Materials and Energy*, Proceedings of the 22nd International Conference on Plasma Surface Interactions 2016, 22nd PSI, vol. 12, pp. 1043–1048, Aug. 2017, ISSN: 2352-1791. DOI: 10.1016/j.nme.2016.12.023.

[41] Y. Shimomura, M. Keilhacker, K. Lackner, and H. Murmann, "Characteristics of the divertor plasma in neutral-beam-heated ASDEX discharges," en, *Nuclear Fusion*, vol. 23, no. 7, p. 869, Jul. 1983, ISSN: 0029-5515. DOI: 10.1088/0029-5515/23/7/002.

[42] S. I. Krasheninnikov, A. S. Kukushkin, and A. A. Pshenov, "Divertor plasma detachment," *Physics of Plasmas*, vol. 23, no. 5, p. 055 602, May 2016, ISSN: 1070-664X. DOI: 10.1063/1.4948273.

[43] A. S. Kukushkin and H. D. Pacher, "The Role of "Momentum Removal" in Divertor Detachment," en, *Contributions to Plasma Physics*, vol. 56, no. 6-8, pp. 711–716, 2016, _eprint: https://onlinelibrary.wiley.com/doi/pdf/10.1002/ctpp.201610048, ISSN: 1521-3986. DOI: 10.1002/ctpp.201610048.

[44] A. W. Leonard, "Plasma detachment in divertor tokamaks," en, *Plasma Physics and Controlled Fusion*, vol. 60, no. 4, p. 044 001, Feb. 2018, Publisher: IOP Publishing, ISSN: 0741-3335. DOI: 10.1088/1361-6587/aaa7a9.

[45] Y Feng, M Kobayashi, T Lunt, and D Reiter, "Comparison between stellarator and tokamak divertor transport," en, *Plasma Physics and Controlled Fusion*, vol. 53, no. 2, p. 024 009, Jan. 2011, ISSN: 0741-3335. DOI: 10.1088/0741-3335/53/2/024009.

[46] P. Grigull, K. McCormick, H. Renner, *et al.*, "Divertor operation in stellarators: Results from W7-AS and implications for future devices," *Fusion Engineering and Design*, 22nd Symposium on Fusion Technology, vol. 66-68, pp. 49–58, Sep. 2003, ISSN: 0920-3796. DOI: 10.1016/S0920-3796(03)00121-2.

[47] G. Motojima, S. Masuzaki, H. Tanaka, *et al.*, "Establishment of a low recycling state with full density control by active pumping of the closed helical divertor at LHD," en, *Nuclear Fusion*, vol. 58, no. 1, p. 014 005, Nov. 2017, Publisher: IOP Publishing, ISSN: 0029-5515. DOI: 10.1088/1741-4326/aa9720.

[48] M. Jakubowski, M. Endler, Y. Feng, *et al.*, "Overview of the results from divertor experiments with attached and detached plasmas at Wendelstein 7-X and their implications for steady-state operation," en, *Nuclear Fusion*, vol. 61, no. 10, p. 106 003, Aug. 2021, Publisher: IOP Publishing, ISSN: 0029-5515. DOI: 10.1088/1741-4326/ac1b68.

[49] A. H. Boozer, "Stellarator design," en, *Journal of Plasma Physics*, vol. 81, no. 6, p. 515 810 606, Dec. 2015, Publisher: Cambridge University Press, ISSN: 0022-3778, 1469-7807. DOI: 10.1017/S0022377815001373.

[50] A. H. Boozer and A. Punjabi, "Simulation of stellarator divertors," *Physics of Plasmas*, vol. 25, no. 9, p. 092 505, Sep. 2018, ISSN: 1070-664X. DOI: 10.1063/1.5042666.

[51] A. Punjabi and A. H. Boozer, "Simulation of non-resonant stellarator divertor," *Physics of Plasmas*, vol. 27, no. 1, p. 012 503, Jan. 2020, Publisher: American Institute of Physics, ISSN: 1070-664X. DOI: 10.1063/1.5113907.

[52] J. R. Cary and R. G. Littlejohn, "Noncanonical Hamiltonian mechanics and its application to magnetic field line flow," *Annals of Physics*, vol. 151, no. 1, pp. 1–34, Nov. 1983, ISSN: 0003-4916. DOI: 10.1016/0003-4916(83)90313-5.

[53] A. H. Boozer, "Physics of magnetically confined plasmas," *Reviews of Modern Physics*, vol. 76, no. 4, pp. 1071–1141, Jan. 2005, Publisher: American Physical Society. DOI: 10.1103/RevModPhys.76.1071.

[54] L.-M. Imbert-Gérard, E. J. Paul, and A. M. Wright, *An Introduction to Stellarators: From Magnetic Fields to Symmetries and Optimization*. Philadelphia, PA: Society for Industrial and Applied Mathematics, 2024.

[55] A. H. Boozer, "Evaluation of the structure of ergodic fields," *The Physics of Fluids*, vol. 26, no. 5, pp. 1288–1291, May 1983, ISSN: 0031-9171. DOI: 10.1063/1.864289.

[56] A. Kolmogorov, "On conservation of conditionally periodic motions for a small change in Hamilton's function," *Proceedings of the USSR Academy of Sciences*, 1954.

[57] "Proof of a theorem of A. N. Kolmogorov on the invariance of quasi-periodic motions under small perturbations of the Hamiltonian," en, in *Collected Works: Representations of Functions, Celestial Mechanics and KAM Theory, 1957–1965*, V. I. Arnold, A. B. Givental, B. A. Khesin, *et al.*, Eds., Berlin, Heidelberg: Springer, 2009, pp. 267–294, ISBN: 978-3-642-01742-1. DOI: 10.1007/978-3-642-01742-1_21.

[58] J. Moser, "On invariant curves of area-preserving mappings of an anulus," *Matematika*, vol. 6, no. 5, pp. 51–68, 1962.

[59] C. Oestreicher, "A history of chaos theory," *Dialogues in Clinical Neuroscience*, vol. 9, no. 3, pp. 279–289, Sep. 2007, ISSN: 1294-8322.

[60] E. Ott, *Chaos in Dynamical Systems*, 2nd ed. Cambridge: Cambridge University Press, 2002, ISBN: 978-0-521-01084-9. DOI: 10.1017/CBO9780511803260.

[61] R. S. Mackay, J. D. Meiss, and I. C. Percival, "Transport in Hamiltonian systems," en, *Physica D: Nonlinear Phenomena*, vol. 13, no. 1, pp. 55–81, Aug. 1984, ISSN: 0167-2789. DOI: 10.1016/0167-2789(84)90270-7.

[62] D. Beigie, A. Leonard, and S. Wiggins, "Chaotic transport in the homoclinic and heteroclinic tangle regions of quasiperiodically forced two-dimensional dynamical systems," en, *Nonlinearity*, vol. 4, no. 3, p. 775, Aug. 1991, ISSN: 0951-7715. DOI: 10.1088/0951-7715/4/3/008.

[63] A. Punjabi and A. Boozer, "Homoclinic tangle in tokamak divertors," *Physics Letters A*, vol. 378, no. 32, pp. 2410–2416, Jun. 2014, ISSN: 0375-9601. DOI: 10.1016/j.physleta.2014.06.027.

[64] T. E. Evans, R. K. W. Roeder, J. A. Carter, B. I. Rapoport, M. E. Fenstermacher, and C. J. Lasnier, "Experimental signatures of homoclinic tangles in poloidally diverted tokamaks," en, *Journal of Physics: Conference Series*, vol. 7, no. 1, p. 174, Jan. 2005, ISSN: 1742-6596. DOI: 10.1088/1742-6596/7/1/015.

[65] P. Ghendrih, A. Grosman, and H. Capes, "Theoretical and experimental investigations of stochastic boundaries in tokamaks," en, *Plasma Physics and Controlled Fusion*, vol. 38, no. 10, p. 1653, Oct. 1996, ISSN: 0741-3335. DOI: 10.1088/0741-3335/38/10/002.

[66] S. S. Abdullaev, K. H. Finken, and K. H. Spatschek, "Asymptotical and mapping methods in study of ergodic divertor magnetic field in a toroidal system," *Physics of Plasmas*, vol. 6, no. 1, pp. 153–174, Jan. 1999, ISSN: 1070-664X. DOI: 10.1063/1.873270.

[67] J. D. Meiss, "Thirty years of turnstiles and transport," *Chaos: An Interdisciplinary Journal of Nonlinear Science*, vol. 25, no. 9, p. 097 602, Mar. 2015, ISSN: 1054-1500. DOI: 10.1063/1.4915831.

[68] A. Wingen, M. Jakubowski, K. H. Spatschek, *et al.*, "Traces of stable and unstable manifolds in heat flux patterns," *Physics of Plasmas*, vol. 14, no. 4, p. 042 502, Apr. 2007, ISSN: 1070-664X. DOI: 10.1063/1.2715548.

[69] O. Schmitz, T. E. Evans, M. E. Fenstermacher, *et al.*, "Aspects of three dimensional transport for ELM control experiments in ITER-similar shape plasmas at low collisionality in DIII-D," en, *Plasma Physics and Controlled Fusion*, vol. 50, no. 12, p. 124 029, Nov. 2008, ISSN: 0741-3335. DOI: 10.1088/0741-3335/50/12/124029.

[70] H. Frerichs, D. Reiter, O. Schmitz, *et al.*, "Impact of screening of resonant magnetic perturbations in three dimensional edge plasma transport simulations for DIII-D," *Physics of Plasmas*, vol. 19, no. 5, p. 052 507, May 2012, ISSN: 1070-664X. DOI: 10.1063/1.4714616.

[71] M. W. Jakubowski, S. S. Abdullaev, K. H. Finken, and t. T. Team, "Modelling of the magnetic field structures and first measurements of heat fluxes for TEXTOR-DED operation," en, *Nuclear Fusion*, vol. 44, no. 6, S1, May 2004, ISSN: 0029-5515. DOI: 10.1088/0029-5515/44/6/S01.

[72] S. S. Abdullaev, K. H. Finken, M. W. Jakubowski, *et al.*, "Overview of magnetic structure induced by the TEXTOR-DED and the related transport," en, *Nuclear Fusion*, vol. 43, no. 5, p. 299, Apr. 2003, ISSN: 0029-5515. DOI: 10.1088/0029-5515/43/5/302.

[73] TEXTOR Team, M. W. Jakubowski, O. Schmitz, *et al.*, "Change of the Magnetic-Field Topology by an Ergodic Divertor and the Effect on the Plasma Structure and Transport," *Physical Review Letters*, vol. 96, no. 3, p. 035 004, Jan. 2006, Publisher: American Physical Society. DOI: 10.1103/PhysRevLett.96.035004.

[74] T. Eich, D. Reiser, and K. H. Finken, "Two dimensional modelling approach to transport properties of the TEXTOR-DED laminar zone," en, *Nuclear Fusion*, vol. 40, no. 10, p. 1757, Oct. 2000, ISSN: 0029-5515. DOI: 10.1088/0029-5515/40/10/307.

[75] O. Schmitz, M. W. Jakubowski, H. Frerichs, *et al.*, "Identification and analysis of transport domains in the stochastic boundary of TEXTOR-DED for different mode spectra," en, *Nuclear Fusion*, vol. 48, no. 2, p. 024 009, Jan. 2008, ISSN: 0029-5515. DOI: 10.1088/0029-5515/48/2/024009.

[76] F. Nguyen, P. Chendrih, and A. Grosman, "Interaction of stochastic boundary layer with plasma facing components," en, *Nuclear Fusion*, vol. 37, no. 6, p. 743, Jun. 1997, ISSN: 0029-5515. DOI: 10.1088/0029-5515/37/6/I03.

[77] S. S. Abdullaev, "On mapping models of field lines in a stochastic magnetic field," en, *Nuclear Fusion*, vol. 44, no. 6, S12, May 2004, ISSN: 0029-5515. DOI: 10.1088/0029-5515/44/6/S02.

[78] A. Punjabi and A. H. Boozer, "Magnetic turnstiles in nonresonant stellarator divertor," *Physics of Plasmas*, vol. 29, no. 1, Jan. 2022, ISSN: 1070-664X. DOI: 10.1063/5.0068913.

[79] R. Davies, C. B. Smiet, A. Punjabi, A. Boozer, and S. A. Henneberg, *The topology of non-resonant stellarator divertors*, arXiv:2501.18293 [physics], Jan. 2025. DOI: 10.48550/arXiv.2501.18293.

[80] S. P. Hirshman and D. K. Lee, "MOMCON: A spectral code for obtaining three-dimensional magnetohydrodynamic equilibria," en, *Computer Physics Communications*, vol. 39, no. 2, pp. 161–172, Feb. 1986, ISSN: 0010-4655. DOI: 10.1016/0010-4655(86)90127-X.

[81] J. Schilling, *The Numerics of VMEC++*, arXiv:2502.04374 [physics], Feb. 2025. DOI: 10.48550/arXiv.2502.04374.

[82] M. R. Cianciosa, S. P. Hirshman, and S. K. Seal, "Development of a free-boundary version of the SIESTA MHD equilibrium code," *58th Annual Meeting of the APS Division of Plasma Physics*, 2016, (Poster).

[83] H. Frerichs, "FLARE: Field line analysis and reconstruction for 3D boundary plasma modeling," en, *Nuclear Fusion*, vol. 64, no. 10, p. 106 034, Sep. 2024, Publisher: IOP Publishing, ISSN: 0029-5515. DOI: 10.1088/1741-4326/ad7303.

[84] J. R. Dormand and P. J. Prince, "A family of embedded Runge-Kutta formulae," *Journal of Computational and Applied Mathematics*, vol. 6, no. 1, pp. 19–26, Mar. 1980, ISSN: 0377-0427. DOI: 10.1016/0771-050X(80)90013-3.

[85] S. S. Abdullaev, "Stable and unstable manifolds, and the structure of magnetic footprints," en, *Nuclear Fusion*, vol. 54, no. 6, p. 064 004, May 2014, Publisher: IOP Publishing, ISSN: 0029-5515. DOI: 10.1088/0029-5515/54/6/064004.

[86] O. Schmitz, M. Becoulet, P. Cahyna, *et al.*, "Three-dimensional modeling of plasma edge transport and divertor fluxes during application of resonant magnetic perturbations on ITER," en, *Nuclear Fusion*, vol. 56, no. 6, p. 066 008, May 2016, Publisher: IOP Publishing, ISSN: 0029-5515. DOI: 10.1088/0029-5515/56/6/066008.

[87] H. Frerichs, O. Schmitz, I. Waters, *et al.*, "Exploration of magnetic perturbation effects on advanced divertor configurations in NSTX-U," *Physics of Plasmas*, vol. 23, no. 6, p. 062 517, Jun. 2016, ISSN: 1070-664X. DOI: 10.1063/1.4954816.

[88] "Center for High Throughput Computing," 2006. DOI: 10.21231/GNT1-HW21.

[89] A. R. Akerson, A. Bader, C. C. Hegna, *et al.*, "Three-dimensional scrape off layer transport in the helically symmetric experiment HSX," en, *Plasma Physics and Controlled Fusion*, vol. 58, no. 8, p. 084 002, Jun. 2016, Publisher: IOP Publishing, ISSN: 0741-3335. DOI: 10.1088/0741-3335/58/8/084002.

[90] G. Kawamura, H. Tanaka, K. Mukai, *et al.*, "Three-dimensional impurity transport modeling of neon-seeded and nitrogen-seeded LHD plasmas," en, *Plasma Physics and Controlled Fusion*, vol. 60, no. 8, p. 084 005, Jun. 2018, Publisher: IOP Publishing, ISSN: 0741-3335. DOI: 10.1088/1361-6587/aac9ea.

[91] R. Matoike, G. Kawamura, S. Ohshima, *et al.*, "First Application of 3D Peripheral Plasma Transport Code EMC3-EIRENE to Heliotron J," *Plasma and Fusion Research*, vol. 14, pp. 3 403 127–3 403 127, 2019. DOI: 10.1585/pfr.14.3403127.

[92] V. R. Winters, F. Reimold, R. König, *et al.*, "EMC3-EIRENE simulation of first wall recycling fluxes in W7-X with relation to H-alpha measurements," en, *Plasma Physics and Controlled Fusion*, vol. 63, no. 4, p. 045 016, Mar. 2021, Publisher: IOP Publishing, ISSN: 0741-3335. DOI: 10.1088/1361-6587/abe39c.

[93] S. Y. Dai, H. M. Zhang, B. Lyu, *et al.*, "Impacts of resonant magnetic perturbations on edge carbon transport and emission on EAST with EMC3-EIRENE modelling," en, *Journal of Plasma Physics*, vol. 86, no. 3, p. 815 860 303, Jun. 2020, Publisher: Cambridge University Press, ISSN: 0022-3778, 1469-7807. DOI: 10.1017/S0022377820000422.

[94] L. Bock, D. Brida, M. Faitsch, K. Schmid, T. Lunt, and t. A. U. Team, "Comparison of the influence of 2D and 3D geometry of the main chamber on plasma parameters in the SOL of ASDEX Upgrade," en, *Nuclear Fusion*, vol. 62, no. 2, p. 026 020, Dec. 2021, Publisher: IOP Publishing, ISSN: 0029-5515. DOI: 10.1088/1741-4326/ac3f49.

[95] H. Frerichs, Y. Feng, X. Bonnin, R. A. Pitts, D. Reiter, and O. Schmitz, "Volumetric recombination in EMC3-EIRENE: Implementation and first application to the pre-fusion power operation phase in ITER," *Physics of Plasmas*, vol. 28, no. 10, p. 102 503, Oct. 2021, ISSN: 1070-664X. DOI: 10.1063/5.0062248.

[96] Y. Feng, F. Sardei, and J. Kisslinger, "A simple highly accurate field-line mapping technique for three-dimensional Monte Carlo modeling of plasma edge transport," *Physics of Plasmas*, vol. 12, no. 5, p. 052 505, Apr. 2005, ISSN: 1070-664X. DOI: 10.1063/1.1888959.

[97] H Frerichs, D Boeyaert, Y Feng, and K. A. Garcia, "Magnetic mesh generation and field line reconstruction for scrape-off layer and divertor modeling in stellarators," en, *Plasma Physics and Controlled Fusion*, vol. 67, no. 4, p. 045 012, Mar. 2025, Publisher: IOP Publishing, ISSN: 0741-3335. DOI: 10.1088/1361-6587/adbb8c.

[98] X. Ma, M. R. Cianciosa, D. A. Ennis, *et al.*, "Determination of current and rotational transform profiles in a current-carrying stellarator using soft x-ray emissivity measurements," *Physics of Plasmas*, vol. 25, no. 1, p. 012 516, Jan. 2018, ISSN: 1070-664X. DOI: 10.1063/1.5013347.

[99] J. D. Lore, T. Andreeva, J. Boscary, *et al.*, "Design and Analysis of Divertor Scraper Elements for the W7-X Stellarator," *IEEE Transactions on Plasma Science*, vol. 42, no. 3, pp. 539–544, Mar. 2014, Conference Name: IEEE Transactions on Plasma Science, ISSN: 1939-9375. DOI: 10.1109/TPS.2014.2303649.

[100] M. Kobayashi, Y. Xu, K. Ida, *et al.*, "3D effects of edge magnetic field configuration on divertor/scrape-off layer transport and optimization possibilities for a future reactor," en, *Nuclear Fusion*, vol. 55, no. 10, p. 104 021, Sep. 2015, Publisher: IOP Publishing, ISSN: 0029-5515. DOI: 10.1088/0029-5515/55/10/104021.

[101] S. S. Abdullaev, T. Eich, and K. H. Finken, "Fractal structure of the magnetic field in the laminar zone of the Dynamic Ergodic Divertor of the Torus Experiment for Technology-Oriented Research (TEXTOR-94)," *Physics of Plasmas*, vol. 8, no. 6, pp. 2739–2749, Jun. 2001, ISSN: 1070-664X. DOI: 10.1063/1.1371954.

[102] Y. Gao, Y. Feng, M. Endler, *et al.*, "Improvement in the simulation tools for heat distribution predictions and control of baffle and middle divertor loads in Wendelstein 7-X," en, *Nuclear Fusion*, vol. 63, no. 2, p. 026 031, Jan. 2023, Publisher: IOP Publishing, ISSN: 0029-5515. DOI: 10.1088/1741-4326/acaf0e.

[103] M. Kobayashi, F. Y., M. S., *et al.*, "Transport Characteristics in the Stochastic Magnetic Boundary of LHD: Magnetic Field Topology and Its Impact on Divertor Physics and Impurity Transport," *Fusion Science and Technology*, vol. 58, no. 1, pp. 220–231, Aug. 2010, ISSN: 1536-1055. DOI: 10.13182/FST10-A10809.

[104] N. Allen and et al, "Studies of Non-Resonant Divertor Strike Line Resiliency in the Compact Toroidal Hybrid," *66th Annual Meeting of the APS Division of Plasma Physics*, Oct. 2024, (Poster).

[105] F Warmer, C. D. Beidler, A Dinklage, R Wolf, and T. W.-X. Team, "From W7-X to a HELIAS fusion power plant: Motivation and options for an intermediate-step burning-plasma stellarator," en, *Plasma Physics and Controlled Fusion*, vol. 58, no. 7, p. 074 006, Jun. 2016, Publisher: IOP Publishing, ISSN: 0741-3335. DOI: 10.1088/0741-3335/58/7/074006.

[106] J. Lion, J. C. Anglès, L. Bonauer, *et al.*, "Stellaris: A high-field quasi-isodynamic stellarator for a prototypical fusion power plant," *Fusion Engineering and Design*, p. 114 868, Feb. 2025, ISSN: 0920-3796. DOI: 10.1016/j.fusengdes.2025.114868.

[107] C. C. Hegna, D. T. Anderson, E. C. Andrew, *et al.*, "The Infinity Two fusion pilot plant baseline plasma physics design," en, *Journal of Plasma Physics*, vol. 91, no. 3, E76, Jun. 2025, ISSN: 0022-3778, 1469-7807. DOI: 10.1017/S0022377825000364.

[108] M. Landreman and E. Paul, "Magnetic Fields with Precise Quasisymmetry for Plasma Confinement," *Physical Review Letters*, vol. 128, no. 3, p. 035 001, Jan. 2022, Publisher: American Physical Society. DOI: 10.1103/PhysRevLett.128.035001.

[109] M. J. Gerard, B. Geiger, M. J. Pueschel, *et al.*, "Optimizing the HSX stellarator for microinstability by coil-current adjustments," en, *Nuclear Fusion*, vol. 63, no. 5, p. 056 004, Mar. 2023, Publisher: IOP Publishing, ISSN: 0029-5515. DOI: 10.1088/1741-4326/acc1f6.

[110] H. Frerichs, O. Schmitz, T. Evans, Y. Feng, and D. Reiter, "The pattern of parallel edge plasma flows due to pressure gradients, recycling, and resonant magnetic perturbations in DIII-D," *Physics of Plasmas*, vol. 22, no. 7, p. 072 508, Jul. 2015, ISSN: 1070-664X. DOI: 10.1063/1.4926524.

[111] F. Cai, S. Kado, G. Kawamura, *et al.*, "Impact of multifold magnetic structure on spectroscopy analysis in Heliotron J based on EMC3-EIRENE simulation," en, *Contributions to Plasma Physics*, vol. 64, no. 7-8, e202300145, 2024, _eprint: https://onlinelibrary.wiley.com/doi/pdf/10.1002/ctpp.202300145, ISSN: 1521-3986. DOI: 10.1002/ctpp.202300145.

[112] K. C. Hammond, Y. Gao, M. Jakubowski, *et al.*, "Drift effects on W7-X divertor heat and particle fluxes," en, *Plasma Physics and Controlled Fusion*, vol. 61, no. 12, p. 125 001, Oct. 2019, Publisher: IOP Publishing, ISSN: 0741-3335. DOI: 10.1088/1361-6587/ab4825.

[113] T. Morisaki, S. Sakakibara, K. Watanabe, *et al.*, "Characteristics of Edge Magnetic Field Structure in LHD Heliotron," en, *Contributions to Plasma Physics*, vol. 40, no. 3-4, pp. 266–270, 2000, ISSN: 1521-3986. DOI: 10.1002/1521-3986(200006)40:3/4<266::AID-CTPP266>3.0.CO;2-M.

[114] A. Wolf, "13. Quantifying chaos with Lyapunov exponents," in *Chaos*, A. V. Holden, Ed., Princeton: Princeton University Press, 1986, pp. 273–290, ISBN: 978-1-4008-5815-6. DOI: doi:10.1515/9781400858156.273.

[115] P. Virtanen, R. Gommers, T. E. Oliphant, *et al.*, "SciPy 1.0: Fundamental algorithms for scientific computing in Python," en, *Nature Methods*, vol. 17, no. 3, pp. 261–272, Mar. 2020, Publisher: Nature Publishing Group, ISSN: 1548-7105. DOI: 10.1038/s41592-019-0686-2.

[116] A. H. Boozer, "Needed computations and computational capabilities for stellarators," *Physics of Plasmas*, vol. 31, no. 6, p. 060 601, Jun. 2024, ISSN: 1070-664X. DOI: 10.1063/5.0211063.

[117] V. R. Winters, F. Reimold, Y. Feng, *et al.*, "First experimental confirmation of island SOL geometry effects in a high radiation regime on W7-X," en, *Nuclear Fusion*, vol. 64, no. 12, p. 126 047, Oct. 2024, Publisher: IOP Publishing, ISSN: 0029-5515. DOI: 10.1088/1741-4326/ad820e.

[118] D. Boeyaert, Y. Feng, H. Frerichs, *et al.*, "Analysis of the neutral fluxes in the divertor region of Wendelstein 7-X under attached and detached conditions using EMC3-EIRENE," en, *Plasma Physics and Controlled Fusion*, vol. 66, no. 1, p. 015 005, Nov. 2023, Publisher: IOP Publishing, ISSN: 0741-3335. DOI: 10.1088/1361-6587/ad0e22.

[119] D. Boeyaert, K. A. Garcia, H. Frerichs, *et al.*, "Towards improved neutral exhaust in the HSX stellarator," *Nuclear Materials and Energy*, vol. 42, p. 101 874, Mar. 2025, ISSN: 2352-1791. DOI: 10.1016/j.nme.2025.101874.

[120] A. Bader, D. T. Anderson, C. C. Hegna, Y. Feng, J. D. Lore, and J. N. Talmadge, "Simulations of edge configurations in quasi-helically symmetric geometry using EMC3–EIRENE," en, *Nuclear Fusion*, vol. 53, no. 11, p. 113 036, Oct. 2013, Publisher: IOP Publishing and International Atomic Energy Agency, ISSN: 0029-5515. DOI: 10.1088/0029-5515/53/11/113036.

[121] Y. Feng, H. Frerichs, M. Kobayashi, *et al.*, "Recent Improvements in the EMC3-Eirene Code," en, *Contributions to Plasma Physics*, vol. 54, no. 4-6, pp. 426–431, 2014, ISSN: 1521-3986. DOI: 10.1002/ctpp.201410092.

[122] H. Frerichs, D. Reiter, Y. Feng, and D. Harting, "Block-structured grids in Lagrangian 3D edge plasma transport simulations," *Computer Physics Communications*, vol. 181, no. 1, pp. 61–70, Jan. 2010, ISSN: 0010-4655. DOI: 10.1016/j.cpc.2009.08.016.

[123] F. Reimold, R Konig, F. Effenberg, *et al.*, "Experimental indications of high-recycling and the role of pressure and power dissipation for detachment at W7-X," 2021.

[124] T. Morisaki, S. Masuzaki, M. Kobayashi, *et al.*, "Initial experiments towards edge plasma control with a closed helical divertor in LHD," en, *Nuclear Fusion*, vol. 53, no. 6, p. 063 014, May 2013, Publisher: IOP Publishing and International Atomic Energy Agency, ISSN: 0029-5515. DOI: 10.1088/0029-5515/53/6/063014.

[125] N. Maaziz, F. Reimold, V. R. Winters, D. Bold, Y. Feng, and V. Perseo, "Investigating the role of divertor geometry on density build-up in the island divertor," *Nuclear Materials and Energy*, vol. 42, p. 101 886, Mar. 2025, ISSN: 2352-1791. DOI: 10.1016/j.nme.2025.101886.

[126] T. Sunn Pedersen, A. Dinklage, Y. Turkin, *et al.*, "Key results from the first plasma operation phase and outlook for future performance in Wendelstein 7-X," *Physics of Plasmas*, vol. 24, no. 5, p. 055 503, May 2017, ISSN: 1070-664X. DOI: 10.1063/1.4983629.

[127] N. Chaudhary, M. Hirsch, T. Andreeva, *et al.*, "Radial localization of electron temperature pedestal and ELM-like events using ECE measurements at Wendelstein 7-X," en, *EPJ Web of Conferences*, vol. 277, p. 03 004, 2023, Publisher: EDP Sciences, ISSN: 2100-014X. DOI: 10.1051/epjconf/202327703004.

[128] N. Chaudhary, M. Hirsch, T. Andreeva, *et al.*, "Electron transport barrier and high confinement in configurations with internal islands close to the plasma edge of W7-X," en, *Nuclear Fusion*, vol. 64, no. 10, p. 106 038, Sep. 2024, Publisher: IOP Publishing, ISSN: 0029-5515. DOI: 10.1088/1741-4326/ad703e.

[129] N Chaudhary, M Hirsch, T Andreeva, *et al.*, "Impact of internal magnetic islands on the electron temperature transport barrier and plasma confinement in W7-X," *24th International Stellarator Heliotron Workshop*, Sep. 2024, (Invited).

[130] D Boeyaert and A Kharwandikar, *Private Communication.*

[131] G. Harrer and et al, "STAR_lite Update: Transition to Modular Coils, Internal Vacuum Vessel, and Simplified Manufacturing," *Princeton Plasma Physics Laboratory - Stellarator Seminar Series*, Feb. 2025.

[132] L Tang and et al, "Divertor Design Plans for Eos Stellarator," *66th Annual Meeting of the APS Division of Plasma Physics*, Oct. 2024, (Poster).